

The Pennsylvania State University  
Applied Research Laboratory  
PO Box 30, State College, PA 16804

PERFORMANCE MEASUREMENTS ON  
A THERMOACOUSTIC REFRIGERATOR  
DRIVEN AT HIGH AMPLITUDES

by

Matthew Ernest Poes  
and  
Steven L. Garrett

Technical Report Number: TR 98- 003  
June 1998

Supported by:  
ARL through the Enrichment and Foundation Program  
Office of Naval Research  
NASA through the Pennsylvania Space Grant Consortium

19980622  
138

Approved for public release; distribution unlimited

# REPORT DOCUMENTATION PAGE

Form Approved  
OMB No. 0704-0188

Public reporting burden for this collection of information is estimated to average 1 hour per response, including the time for reviewing instructions, searching existing data sources, gathering and maintaining the data needed, and completing and reviewing the collection of information. Send comments regarding this burden estimate or any other aspect of this collection of information, including suggestions for reducing this burden, to Washington Headquarters Services, Directorate for Information Operations and Reports, 1215 Jefferson Davis Highway, Suite 1204, Arlington, VA 22202-4302, and to the Office of Management and Budget, Paperwork Reduction Project (0704-0188), Washington, DC 20503.

1. AGENCY USE ONLY (Leave blank)	2. REPORT DATE	3. REPORT TYPE AND DATES COVERED	
	June 1998	Thesis in Acoustics; Master of Science	
4. TITLE AND SUBTITLE		5. FUNDING NUMBERS	
Performance Measurements on a Thermoacoustic Refrigerator Driven at High Amplitudes			
6. AUTHOR(S)			
Matthew E. Poese Steven L. Garrett			
7. PERFORMING ORGANIZATION NAME(S) AND ADDRESS(ES)		8. PERFORMING ORGANIZATION REPORT NUMBER	
Applied Research Laboratory The Pennsylvania State University PO Box 30 State College, PA 16804		TR 98-003	
9. SPONSORING/MONITORING AGENCY NAME(S) AND ADDRESS(ES)		10. SPONSORING/MONITORING AGENCY REPORT NUMBER	
Office of Naval Research Ballston Tower 800 North Quincy Street Arlington, VA 22217 Logan Hargrove		Pennsylvania Space Grant Consort. 101 S. Frear University Park, PA 16802 Richard Devon, Director	
11. SUPPLEMENTARY NOTES			
12a. DISTRIBUTION/AVAILABILITY STATEMENT		12b. DISTRIBUTION CODE	
Approved for public release: distribution unlimited			
13. ABSTRACT (Maximum 200 words) Since the power density in a thermoacoustic device is proportional to the square of the acoustic Mach number, there is strong motivation to design thermoacoustic refrigerators to operate at larger pressure amplitudes. Measurements are reported of a modified version of the Space Thermoacoustic Refrigerator (STAR), driven at pressure amplitudes up to 6%. This pressure ratio corresponds to 30 W of cooling power -- five times as large as reported in 1993. The results of these measurements are compared to a DELTAE computer model of the low amplitude (linear) performance that matches experimental conditions on a point-by-point basis. It is found that there is a small but measurable deviation in heat pumping power from the power predicted with a linear acoustic computer model. This deviation in heat pumping power at 6% pressure ratio is about 15%. A large, amplitude independent disagreement in the acoustic power needed to attain a specific pressure ratio is found between measured data and DELTAE results. An overview of the instrumentation, including a measurement of exhaust heat with an absolute accuracy of 65 mW, is also presented.			
14. SUBJECT TERMS		15. NUMBER OF PAGES 102	
		16. PRICE CODE	
17. SECURITY CLASSIFICATION OF REPORT Unclassified	18. SECURITY CLASSIFICATION OF THIS PAGE Unclassified	19. SECURITY CLASSIFICATION OF ABSTRACT Unclassified	20. LIMITATION OF ABSTRACT

## Abstract

Since the power density in a thermoacoustic device is proportional to the square of the acoustic Mach number, there is strong motivation to design thermoacoustic refrigerators to operate at larger pressure amplitudes. Measurements are reported of a modified version of the Space ThermoAcoustic Refrigerator (STAR) [S. L. Garrett, *et. al.* “Thermoacoustic Refrigerator for Space Applications,” *Journal of Thermophysics and Heat Transfer* **7**(4), 595–599 (1993)], driven at pressure amplitudes up to 6%, which is two times as large as reported in 1993. The results of these measurements are compared to both a DELTAE computer model of the low amplitude (linear) performance that matches experimental conditions on a point-by-point basis and one that includes turbulent flow in the duct regions of the device.

It is found that there is a small but measurable deviation in heat pumping power from the power predicted with a linear acoustic computer model. This deviation in heat pumping power at 4% pressure ratio is not more than 5% and at 6% pressure ratio is about 15%. The correspondingly poorer coefficient-of-performance is small enough not to deter a thermoacoustic refrigerator designer from designing for high pressure ratio to take advantage of the dramatically increased power density. A large, amplitude independent disagreement in the acoustic power needed to attain a specific pressure ratio is found between measured data and DELTAE results.

Comparison of low amplitude performance to STAR shows that the modified device has a coefficient of performance relative to Carnot curve that is shifted downward by approximately 25%. The total amount of heat pumped with the modified device reaches 30 W which is larger than the amount pumped with STAR by a factor of 5.

An overview of the instrumentation, including a measurement of exhaust heat with an absolute accuracy of 65 mW, is also presented.

# Contents

List of Figures . . . . .	vi
List of Tables . . . . .	vii
Symbol List . . . . .	viii
Chapter 1. Introduction . . . . .	1
1.1. Background . . . . .	1
1.1.1. A Short History of Thermoacoustics . . . . .	2
1.1.2. Performance Metrics of Thermoacoustic Refrigerators . . . . .	3
1.2. The Frankenfridge Device . . . . .	4
1.2.1. Acoustic Subsystem Parameters . . . . .	6
Chapter 2. Thermoacoustics on Paper . . . . .	11
2.1. A Short Heat Engine Primer . . . . .	11
2.1.1. The Natural Engine . . . . .	16
2.2. Linear Model in DELTAE . . . . .	22
2.2.1. Introduction of DELTAE . . . . .	22
2.2.2. The Frankenfridge Model . . . . .	23
2.2.3. A More Detailed Look at the DELTAE Solver . . . . .	28
Chapter 3. Frankenfridge Instrumentation . . . . .	32
3.1. Sensors and Signal Paths . . . . .	32
3.1.1. Sensor Calibration History and Cross-Checks . . . . .	39
3.2. Details of the Exhaust Heat Sink Flange and Flow Loop . . . . .	43
3.3. The Data Recording System using LabVIEW . . . . .	46
Chapter 4. Measurement Analysis and Results . . . . .	48
4.1. Summary of Experiments . . . . .	48

4.2. Exhaust Heat Sink Flange . . . . .	49
4.3. Heat Exchanger Performance Model . . . . .	56
4.4. Performance of Frankenfridge . . . . .	61
4.4.1. Performance at low amplitudes ( $P_A/p_m \leq 3\%$ ) . . . . .	61
4.4.2. Performance at high amplitudes ( $P_A/p_m \leq 6\%$ ) . . . . .	61
4.4.3. DELTAE Model Perturbations . . . . .	64
4.4.4. Comparison of Frankenfridge Performance with STAR Performance . . . . .	67
4.4.5. Resonator Losses . . . . .	69
4.5. Conclusions . . . . .	71
References . . . . .	74
Appendix A. Effects of Stack Position on Engine Performance . . . . .	76
Appendix B. Heat Capacity of the Cold Side Resonator . . . . .	82
Appendix C. Manufacturer Specifications of Sensors . . . . .	84

## List of Figures

Figure	page
1.1. Plan view of STAR and SETAC	5
1.2. Cross-sectional view of Frankenfridge	8
2.1. Heat engine schematic	12
2.2. Schematic of the Carnot cycle	13
2.3. Carnot cycle <i>p-v</i> diagram	14
2.4. Schematic of the thermoacoustic cycle	18
2.5. Thermoacoustic cycle <i>p-v</i> diagram	19
2.6. Relationship of stack and parcel temperatures	22
3.1. Work and heat flux in Frankenfridge	33
3.2. Sensor locations on Frankenfridge	34
3.3. Signal paths of instrumentation	40
3.4. Schematic of the exhaust heat sink flange and heat flux measurement instrumentation	45
4.1. Geometry of the hot and cold heat exchanger	60
4.2. Comparison of measured data and DELTAE prediction of Run #4 data	62
4.3. Comparison of measured data and DELTAE prediction of Run #6 data	63
4.4. Acoustic power requirements in DELTAE models of Run #6 operating conditions	65
4.5. Cooling power in DELTAE models of Run #6 operating conditions	66
4.6. Comparison of coefficient of performance relative to Carnot at 2%	68
4.7. Comparison of coefficient of performance relative to Carnot at 3%	68
4.8. Acoustic pressure magnitude and phase of the Frankenfridge DELTAE model	70
4.9. Resonator acoustic power requirements	71
A.1. Stack performance as a function of stack position in the standing wave	80
B.1. Graph of the initial temperature drop in Run #6	83

## List of Tables

Table	page
1.1. Physical parameters of the resonator and working fluid . . . . .	7
1.2. SETAC Driver Parameters . . . . .	10
4.1. Summary of measurements made with Frankenfridge . . . . .	50
4.2. Subset of data from Run #6 that exhibited a large First Law imbalance . . . . .	52
4.3. Subset of Run #6 data that have been corrected for the First Law imbalance. . . . .	53
4.4. Subset of data from Run #6 that have been corrected for driver housing heat leak . . . . .	55
4.5. Heat exchanger model summary . . . . .	60
B.1. Mass and specific heat of cold side resonator components . . . . .	82

## Symbol List

$a$	Sound speed [m/s]
$COP$	Coefficient of Performance
$COPR$	Coefficient of Performance Relative to Carnot
$c$	Specific heat capacity [ $\frac{\text{J}}{\text{kg}\cdot\text{K}}$ ]
$f$	Frequency [Hz] or Rott function
$\bar{h}$	Average convective heat transport coefficient [ $\frac{\text{W}}{\text{m}^2\cdot\text{K}}$ ]
$K$	Thermal conductivity [ $\frac{\text{W}}{\text{m}\cdot\text{K}}$ ]
$k$	Wavenumber [1/m]
$l$	Stack plate half-thickness [m]
$M$	Molecular weight [kg/kmol]
$\dot{m}$	Mass flow rate [kg/s]
$Nu$	Nusselt number
$P_A$	Peak standing wave pressure magnitude [Pa]
$p_1$	Acoustic pressure [Pa]
$p_m$	Static pressure [Pa]
$Q$	Heat energy [J] or resonance quality factor
$R$	Stack radius [m]
$Re$	Reynolds number
$T_1$	Temperature [m]
$T_m$	Mean temperature [K]
$u_1$	Acoustic particle velocity [m/s]
$V$	Volume [ $\text{m}^3$ ]
$v$	Specific volume [ $\text{m}^3/\text{kg}$ ]
$W$	Work energy [J]
$x_1$	Acoustic particle displacement [m]
$x_{fd}$	Entry length [m]

$y_0$	Stack plate half-separation [m]
$\beta$	Coefficient of thermal expansion [1/K]
$\Gamma$	Normalized temperature gradient
$\gamma$	Polytropic coefficient
$\Delta x$	Stack length [m]
$\delta_k$	Thermal penetration depth [m]
$\delta_v$	Viscous penetration depth [m]
$\epsilon_s$	Stack heat capacity correction factor
$\eta_f$	Fin efficiency
$\kappa$	Thermal diffusivity [m <sup>2</sup> /s]
$\lambda$	Wavelength [m]
$\mu$	Dynamic viscosity [ $\frac{\text{kg}}{\text{m}\cdot\text{s}}$ ]
$\nu$	Kinematic viscosity [m <sup>2</sup> /s]
$\rho_m$	Mean density [kg/m <sup>3</sup> ]
$\Pi$	Total stack transverse perimeter [m]
$\sigma, Pr$	Prandtl number
$\omega$	Angular frequency [rad/s]

# Chapter 1.

## Introduction

---

### 1.1. Background

This thesis focuses on experiments conducted on a small thermoacoustic refrigerator affectionately called “Frankenfridge.”<sup>1</sup> Besides being a catchy project name, this moniker is an apt one because the engine is made of parts from other refrigerators, namely the *Space Thermoacoustic Refrigerator*<sup>2</sup> (STAR) and the *Shipboard Electronics Thermoacoustic Cooler*<sup>3</sup> (SETAC), both designed and built at the Naval Postgraduate School. Frankenfridge is made up from the resonator section of STAR, which includes the stack and heat exchangers, coupled to a SETAC driver. The STAR driver can produce about 10 W of acoustic power while the SETAC driver is capable of producing up to 100 W of sound power. The SETAC driver will allow the STAR resonator to be driven at acoustic pressure amplitudes much higher than the STAR resonator was originally designed to accommodate.

This thesis experimentally characterizes the performance of Frankenfridge driven at pressure ratios between one and six percent. The pressure ratio, which is the ratio of the peak acoustic standing wave pressure in the resonator,  $P_A$ , divided by the static pressure in the resonator,  $p_m$ , never exceeded three percent in the STAR device that flew on the Space Shuttle *Discovery* in 1992. SETAC wasn’t operated above a four percent pressure ratio during its sea trials in 1995. Since power density in a thermoacoustic device increases with the square of increasing pressure ratio, there is strong motivation to design thermoacoustic refrigerators to operate at higher pressure ratios. It is hypothesized that there are significant nonlinear effects that alter the performance of the device from the predicted linear response at pressure ratios greater than four percent.

This experimental treatment attempts to investigate deviations from linear performance predictions of efficiency and heat pumping power at high pressure amplitudes and to determine at what pressure ratio these deviations become significant.

### 1.1.1. A Short History of Thermoacoustics

The interaction of sound and heat was recognized over 200 years ago in the disagreement between Newton and Laplace over whether propagation of sound in air is adiabatic or isothermal (it is largely an adiabatic process — one of the few times that Newton was wrong). Glass blowers in the 19th Century noticed freshly blown hot glass bulbs that were attached to cool stems would occasionally “sing” — this effect was explained by Sondhauss who qualitatively suggested that there existed a relationship between the pitch of the sound and the geometry of the bulbs and stems. Sondhauss makes a note in his work of a “glowing glass harmonica” that preceded his investigation by 40 years. In 1896, Lord Rayleigh explained the Sondhauss effect and correctly understood the natural phasing of the acoustic motion, pressure and temperature changes with the conductive heat transfer that could cause an acoustic oscillation to be sustained. It wasn’t until Nicholas Rott and his collaborators worked out a solid quantitative understanding of thermoacoustics (in an attempt to explain Taconis oscillations) that acousticians were able to create intelligent thermoacoustic engine designs. A more complete history, with many references, can be found in Swift’s<sup>7</sup> excellent review of thermoacoustics published in 1988.

The proliferation in the last fifty years of very reliable and inexpensive refrigerators and air conditioners has led the population of many developed countries to regard cooling machines as a necessity rather than a luxury. Because of these machines’ reliance on CFCs that have been recently found to introduce severe environmental hazards in terms of ozone depletion and then on HCFCs which have global warming “greenhouse” effects, an environmentally benign replacement has also become a necessity instead of a luxury. The thermoacoustic cycle works extremely well with a working fluid of inert gases like helium, argon and xenon. These three gases are found naturally in the atmosphere and underground in great quantity (especially helium and argon) and most importantly do not present ozone depletion or global warming potential. Aside from the environmental benefits, a thermoacoustic engine employs little in the way of complicated machinery. The only moving part in STAR or SETAC is the pusher cone structure in the electro-dynamic driver mechanism. This piston is different than the pistons in the compressors that power the standard Rankine cycle refrigerators that are in most kitchens because the thermoacoustic piston is sealed by a flexure seal and not a sliding seal. The flexure seal is an advantage because it needs no

lubrication and can have a longer lifetime. The thermoacoustic cycle also lends itself well to a more efficient proportional control, rather than the primitive binary control that conventional refrigerators currently employ. All of these reasons make thermoacoustics potentially attractive for widespread commercial use.

### 1.1.2. Performance Metrics of Thermoacoustic Refrigerators

The experiments that are the subject of this thesis are carried out to determine how the performance of a small thermoacoustic refrigerator (with an ideal gas working fluid) deviates at high driving amplitudes from the significant and growing body of linear theory that is valid at low amplitudes. The coefficient of performance, or COP, is one nondimensional parameter that characterizes a heat engine. One can compare this performance to the theoretical performance of the same engine operating in a Carnot cycle between the two thermal reservoirs that correspond to the working temperatures of the actual device. A ratio that we call “coefficient of performance relative to Carnot” or *COPR* can be formed that is the COP divided by the Carnot COP given in Eq. (2.5). Because of turbulent mixing at the cross-sectional changes in the resonator, for example, it is thought that large drive amplitudes will degrade the COP for a refrigerator.

Another metric that is of interest to designers of thermoacoustic engines is an expression for the power density of a thermoacoustic device given by Swift as Eq. 66 in Ref. 7:

$$\frac{\dot{H}_2}{V} \sim \frac{f}{2} \frac{T_m \beta}{(1 + \epsilon_s)} \frac{P_A^2}{\rho_m a^2} \quad (1.1)$$

There are several simplifying assumptions that produce this concise expression. Perhaps the two most gross simplifications are that thermal conduction (heat leak from the hot side to the cold side) along both the stack material and the gas in the stack is neglected and secondly, that the viscosity of the gas is assumed to be zero. Other assumptions are that the stack is short compared to the wavelength of the acoustic standing wave, the temperature difference across the stack is a small fraction of the mean temperature of the stack and gas, and that heat and work flows are at steady state. While the steady state assumption is probably good for Frankenfridge, the no viscosity limit and the short stack approximations are not very accurate.

By substituting  $a^2 = \gamma(\frac{p_m}{\rho_m})$  into Eq. (1.1),

$$\frac{\dot{H}_2}{V} \sim f p_m \left( \frac{P_A}{p_m} \right)^2 \quad (1.2)$$

it becomes easier to see that the power density increases with the square of increasing pressure ratio,  $P_A/p_m$ . The pressure ratio is a convenient measure of how hard the engine is being driven —  $P_A$  is the magnitude of the standing wave pressure at a pressure antinode and  $p_m$  is the ambient pressure in the resonator (which in Frankenfridge is about 10 atmospheres). This relationship tempts the designers of thermoacoustic engines to increase this drive ratio (or pressure ratio) of their engines to get more power out of a smaller box. Because of nonlinear effects such as turbulence, the expression in Eq. (1.2), which is valid in only a linear domain, will predict extraordinary power densities that cannot be achieved in a practical device. It is hypothesized that there is some pressure ratio above which the heat pumping power shows a systematic degradation compared to the above simple expression. It is the charge of this experimenter to find that critical pressure ratio in the STAR resonator (Frankenfridge).

## 1.2. The Frankenfridge Device

As mentioned above, Frankenfridge is a marriage of a small, simple quarter wavelength resonator to a driver designed to power a much larger capacity thermoacoustic refrigerator. The STAR device is powered by a driver capable of producing 10 W of acoustic power — the SETAC driver can produce up to 100 W. In his infinite wisdom, the principal investigator on both the STAR and the SETAC projects made the bolt circle of the flange that couples the resonator to the driver equivalent in both devices so as to make the parts interchangeable. Schematics of STAR (on the left) and SETAC (on the right) are shown in Fig. 1.1

STAR flew on the Space Shuttle *Discovery* in January 1992 as a part of the Get-Away Special payload program. After surviving the rigors of launch, STAR operated autonomously in low-earth orbit. In ground-based tests, STAR spanned a temperature difference of up to 81 K and pumped up to 5 W of heat. It was generally operated at a mean pressure of 1 MPa of a helium (97.2%) and xenon (2.8%) gas mixture or a helium (91.1%) and argon (8.9%) mixture. The device saw acoustic pressure amplitudes up to 2 kPa (which is a pressure ratio  $P_A/p_m$  of 2%). The best coefficient of performance relative to Carnot (*COPR*) attained by STAR<sup>2</sup> was about 16% at a heat load of 2.8 W.

SETAC sailed in April of 1995 on the *USS Deyo (DD-989)*, a Spruance Class Destroyer, and cooled the CV-2095 shipboard radar electronics rack. At its peak operating power

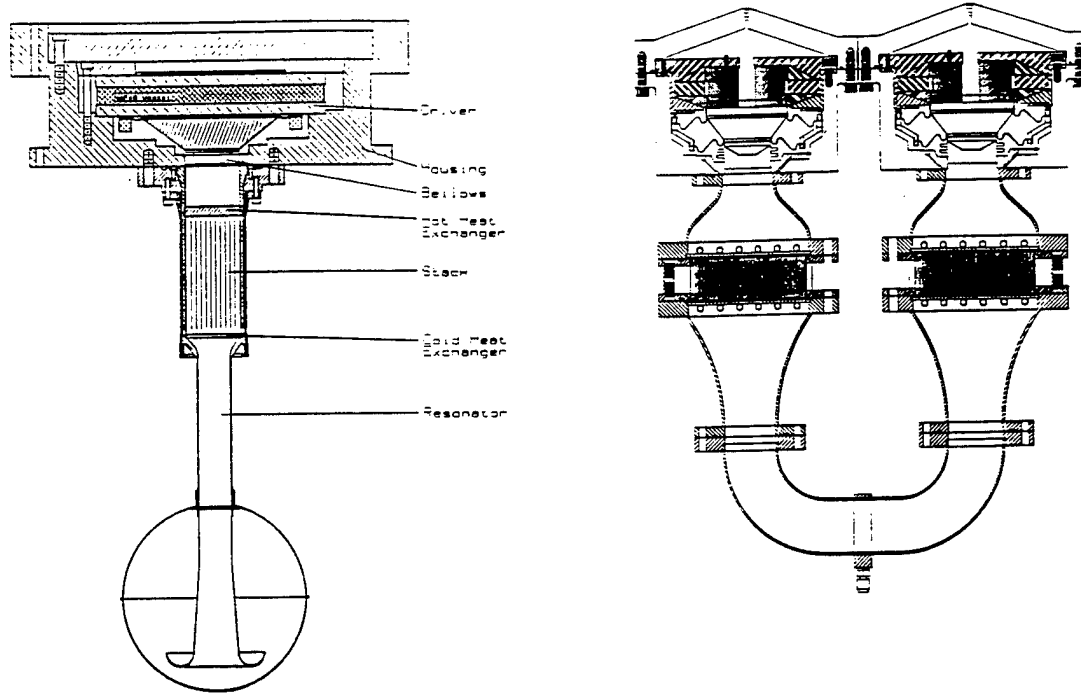


**Figure 1.1:** Schematic of STAR (left) and SETAC (right). Frankenfridge uses a SETAC driver and the STAR resonator. (Source: Ref. 2 and Ref. 3 respectively)

aboard ship, SETAC provided 419 W of cooling power and spanned a temperature difference of about 10 K. The refrigerator operated at 2 MPa of a helium (94%) and argon (6%) gas mixture. SETAC saw acoustic amplitudes of up to 82 kPa (a pressure ratio of 4%). At the 400 W operating point, a COPR of about 8.2% was realized<sup>3</sup>. At a lower power and larger temperature span, the COPR reached 17% based on external reservoir temperatures and 27% based on stack temperatures.

### 1.2.1. Acoustic Subsystem Parameters

Table 1.1 lists some of the more relevant information about the gas and resonator of Frankenfridge at the standard operating point. A cross-sectional view of the device is pictured in Fig. 1.2.

The SETAC driver is instrumented with a microphone positioned very near the pusher cone and an accelerometer mounted directly on the pusher cone. The signals from these two sensors allow the measurement of acoustic input power as well as the stroke of the pusher cone and the acoustic impedance that the resonator presents to the driver. The resonator is instrumented with thermocouples and semiconductor diode thermometers to measure the external metal temperatures near the hot (exhaust) and cold (heat load) heat exchangers. There are no sensors mounted directly inside of the resonator. As pointed out in Fig. 1.2, the resonator is equipped with a small Kapton tape resistance heater just below the cold side heat exchanger. This electrical heater provides an easily controlled and measured amount of heat for the refrigerator to pump. A more detailed explanation of the instrumentation, including the supporting electronics, signal paths, and computerized data acquisition system is provided in Chapter 3.

The only new component that is part of Frankenfridge is the copper exhaust heat sink shown in Fig. 1.2 sandwiched between the SETAC driver and the STAR resonator. This 1/2 in. thick flange has two loops of 1/8 in. copper refrigeration tubing wrapped and soldered around its perimeter to allow water to be circulated around the flange. The water that is pumped through this loop and around the flange will absorb some of the exhaust heat and will therefore experience an increase in temperature as it travels around the flange. The circulation loop is instrumented with a ten junction thermopile (located directly across the inlet and discharge ports of the flange piping) and an in-line flow meter located among the Tygon™ tubing that plumbs the pump, filter and dissipating heat exchanger in the loop. Based on a measurement of the temperature difference and fluid flow rate, the heat flux from the exhaust flange to the water flowing in the loop can be measured. This direct measurement of exhaust heat flux was not made when the resonator was part of STAR. The original STAR device was insulated in a vacuum cannister<sup>4</sup> which meant that knowing the heat flux introduced by the Kapton heater and the acoustic power provided by the

Parameter	Symbol	Value	Units
Mean Pressure	$p_m$	1.07	MPa
Mean Stack Temperature	$T_m$	290	K
Gas Mixture (Helium/Argon)		85.5% He	
Gas Mixture Atomic Mass	$M$	9.214	$\frac{\text{kg}}{\text{kmol}}$
Gas Mixture Density	$\rho$	4.105	$\frac{\text{kg}}{\text{m}^3}$
Gas Mixture Sound Speed	$a$	660.4	$\frac{\text{m}}{\text{s}}$
Gas Mixture Specific Heat	$c_p$	2256	$\frac{\text{J}}{\text{kg}\cdot\text{K}}$
Gas Mixture Polytropic Coefficient	$\gamma$	1.667	
Gas Mixture Prandtl Number	$\sigma$	0.428	
Gas Mixture Kinematic Viscosity	$\mu$	$2.10 \times 10^{-5}$	$\frac{\text{kg}}{\text{s}\cdot\text{m}}$
Gas Mixture Thermal Conductivity	$K_g$	0.111	$\frac{\text{W}}{\text{m}\cdot\text{K}}$
Stack Thermal Conductivity	$K_s$	0.161	$\frac{\text{W}}{\text{m}\cdot\text{K}}$
Stack Specific Heat	$c_s$	1101	$\frac{\text{J}}{\text{kg}\cdot\text{K}}$
Stack Material Density	$\rho_s$	1348	$\frac{\text{kg}}{\text{m}^3}$
Stack Plate Thickness	$2l$	0.0762	mm
Stack Plate Separation	$2y_0$	0.191	mm
Stack Length	$\Delta x$	78.5	mm
Center Position of Stack (ref. from driver)	$x_s$	206.3	mm
Stack Radius	$R$	19.1	mm
Stack (Spiral) Perimeter	$\Pi$	4846	mm
Stack Heat Capacity Correction	$\epsilon_s$	0.067	
Cold Exchanger Length	$\Delta x_C$	6.35	mm
Hot Exchanger Length	$\Delta x_H$	2.54	mm
Exchanger Fin Thickness	$2l^{EX}$	0.254	mm
Exchanger Fin Separation	$2y_0^{EX}$	0.508	mm
Operating Frequency	$f$	328	Hz
Gas Thermal Penetration Depth	$\delta_\kappa$	0.108	mm
Stack Thermal Penetration Depth	$\delta_s$	0.010	mm
Gas Viscous Penetration Depth	$\delta_\nu$	0.070	mm

**Table 1.1:** Physical parameters of the resonator and working fluid

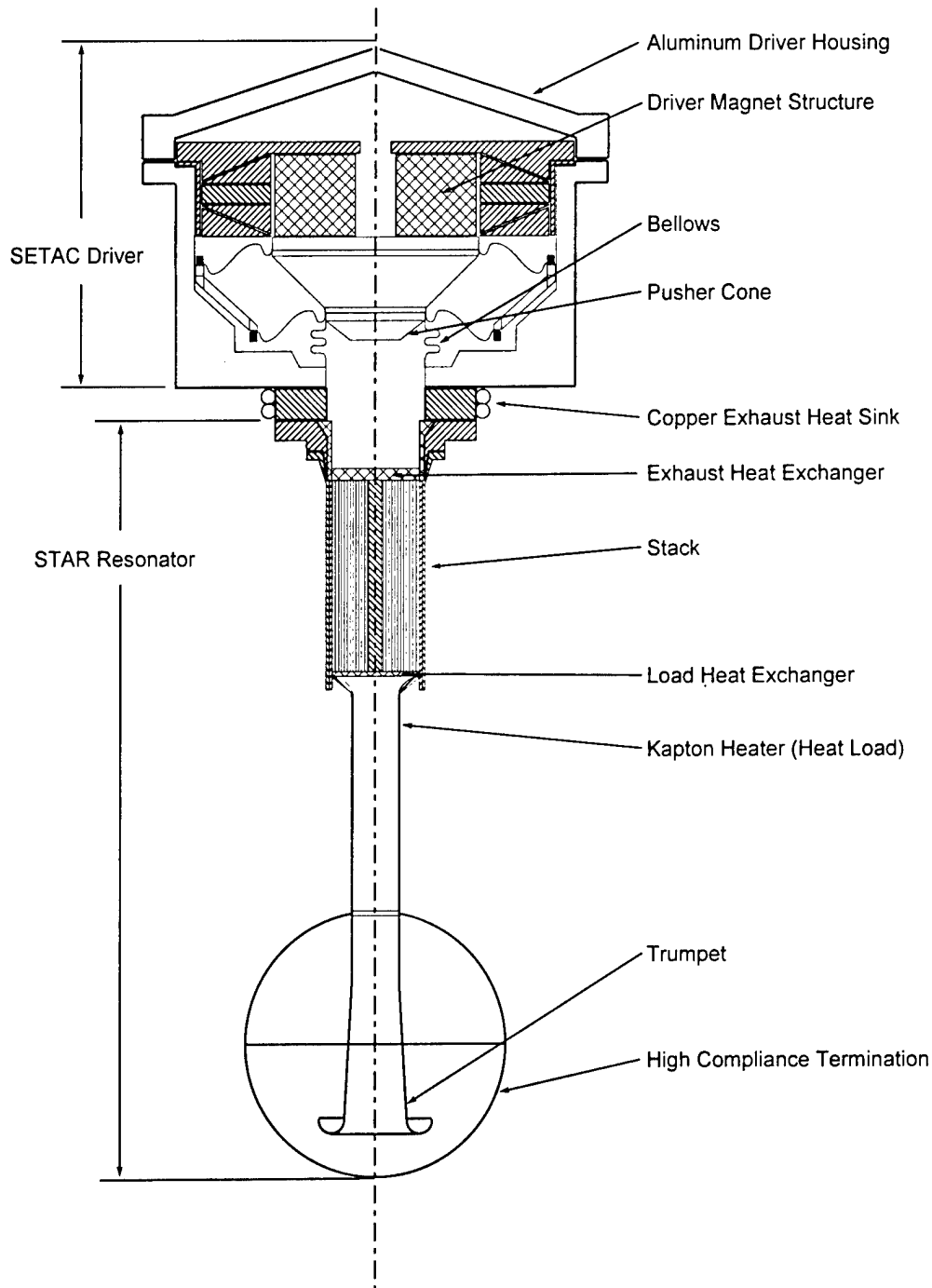


**Figure 1.2:** Cross-sectional view of Frankenfridge. Approximate height is 56 cm and maximum width at the driver housing is 23 cm.

driver<sup>†</sup> was enough to know the exhaust heat flux (from the First Law of Thermodynamics, see Eq. (2.1)). Because Frankenfridge has not nearly as “perfect” an insulation scheme, it is not certain that all of the heat provided by the Kapton heater is pumped by the fridge or, conversely, that the fridge is not pumping heat from the room. While an attempt is made to insulate the refrigerator using standard Corning Pink fiberglass construction grade insulation, for large temperature differences between the cold side duct and room temperature, heat leak to the cold side is expected. Knowledge of the exhaust heat flux will allow calculation of the heat leak as well as providing an accurate determination of the amount of heat that the refrigerator pumps.

The resonator, the new exhaust heat sink, and a 1/8 in. thick Delrin<sup>TM</sup> insulating ring are bolted to the driver with eight 1/4 – 20 bolts on a 3.440 in. diameter bolt circle that is common to the SETAC driver and the STAR resonator. Thermal insulation between the exhaust heat sink and the aluminum driver housing is critical if a temperature increase is to be measured in the exhaust heat sink flange. To this end, the 1/4 in. holes have been enlarged to 5/16 in. to allow for an insulating air gap and the bolt heads have been insulated with nylon washers from the resonator flange to minimize thermal conduction between the resonator and the driver housing. The driver housing is not insulated from the room.

The SETAC driver is capable of producing 100 W of acoustic power. It has an *invacuo* mechanical resonance frequency of 316 Hz. The pertinent driver parameters are listed in Table 1.2. The voice coil is attached to a reducing cone that ends in an aluminum piston face. This cone is attached to the driver housing with a two convolution electroformed nickel bellows that provides a flexure seal for the resonator and eliminates the need for a sliding seal. There is a capillary leak between the back volume of the driver and the volume of the resonator so that the 10 atm of static pressure can equilibrate the driver back volume and not displace the bellows. The bellows does seal the acoustic pressure in the resonator from the driver back volume, however.

The sinusoidal electrical signal supplied to the driver originates from an HP 3314A signal generator and is amplified by a Techron 7520 Power Amplifier. There are no electronics to control the frequency of this signal to keep the standing wave at the resonance frequency of the combined driver/resonator system — a frequency that is changing significantly with the

---

<sup>†</sup> The STAR driver, although only capable of supplying 10 W of power, was instrumented in much the same way as the SETAC driver.

**Table 1.2:** SETAC Driver Parameters

<i>Parameter</i>	<i>Value</i>	<i>Units</i>	<i>Relative Uncertainty</i>
Moving mass	36.4	g	0.8%
Stiffness	143	kN/m	0.5%
Mechanical resistance	2.10	kg/s	0.6%
$Bl$	19.1	N/A	0.7%
DC electrical resistance	1.677	$\Omega$	negligible
Effective bellows area	21	$cm^2$	3%

changing temperature of the gas in the fridge (as the fridge gets cold, so does the working fluid!) In STAR and SETAC a phase-lock loop circuit compared the driver microphone and accelerometer signals to determine the resonance frequency of the resonator. Frankenfridge uses a human controller to accomplish this task — the human controller looks at a Lissajous pattern on a scope that is tracing the accelerometer and microphone signals (to assure a  $90^\circ$  phase relation of acceleration and pressure, or  $0^\circ$  phase difference of velocity and pressure). There are many reasons to stay on resonance, not the least of which is that the stack position in the standing wave is a strong function of heat pumping power. This position is calculated and designed to be a constant parameter for the system at resonance and if the frequency is not changed to accommodate the changing sound speed of the gas mixture this stack position in the standing wave will vary with temperature. Another reason for resonant operation is that the driver delivers the most power when it operates close to its mechanical resonance frequency.

## Chapter 2.

# Thermoacoustics on Paper

---

---

### 2.1. A Short Heat Engine Primer

To begin with some terminology, this thesis will refer to a thermodynamic cycle as the theoretical picture of the thermodynamic processes that combine to form a cycle, while a thermodynamic engine is the physical incarnation of this cycle. Often the cycle on which an engine is based is not exactly the cycle that the engine follows — engineers sometimes have to make approximations to the theoretical cyclic representation when using real hissing steam, clanking gears and sliding pistons. In fact, in the case of the cycle proposed by Rudolf Diesel in 1893, nobody to date has been able to make an engine that follows his cycle — the Diesel engine that is in widespread use today does not really follow the Diesel cycle. The other bit of nomenclature to settle upon is the term engine: this thesis is going to call any thermodynamic machine an engine no matter whether it works in either of two possible modes. These modes are pictured in Fig. 2.1: a prime mover, in which the engine turns the potential energy of a temperature difference into usable work, and a heat pump, where the engine accepts energy in the form of work and uses the work to pump heat from a cold temperature reservoir to a hot temperature reservoir. From the thermodynamic cycle point of view, these two modes are just the opposite of one another; the flow of heat and work are reversed. In this respect, any idealized thermodynamic engine cycle is functionally reversible, however few practical heat engines can be made to run backwards — an automobile engine can't be used as a refrigerator nor can an air conditioner power a Cessna.

To get started, let's consider the Carnot<sup>5</sup> cycle, which was proposed by the Frenchman Sadi Carnot in 1824, and has become known as the most fundamental and simple thermodynamically (and functionally) reversible engine cycle that operates between two temperature reservoirs. The cycle is characterized by alternating two adiabatic steps and two isothermal steps: for the cycle as it operates as a refrigerator the steps are as follows:

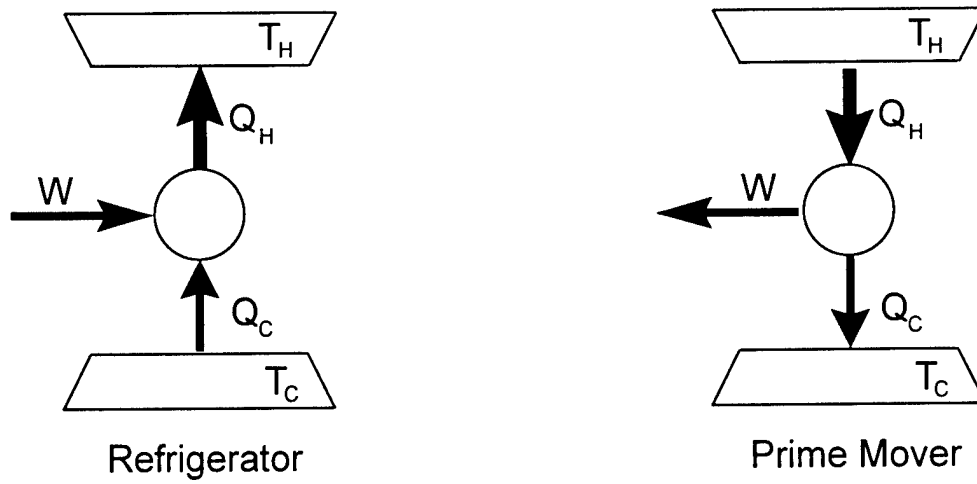


**Figure 2.1:** Schematic of a heat engine functioning as a refrigerator and a prime mover

- Step 1-2: The gas is expanded isothermally at  $T_C$  while receiving energy  $Q_C$  from the cold reservoir by heat transfer.
- Step 2-3: The gas is compressed adiabatically until the gas temperature is  $T_H$ .
- Step 3-4: The gas is compressed isothermally at  $T_H$  while it gives up energy  $Q_H$  to the hot reservoir by heat transfer.
- Step 4-1: The gas expands adiabatically until the gas reaches a temperature  $T_C$ .

This cycle can be visualized physically (see Fig. 2.2) by considering a cylinder filled with an ideal gas and a piston that can compress or expand this gas, which is known as the thermodynamic medium or working fluid. Also consider that this well insulated cylinder can be alternately brought into contact with two large heat reservoirs, one at temperature  $T_C$  and one at temperature  $T_H$ , that have infinite heat capacity. Let's follow the heat and work flux from the point of view of the gas in each of the four stages.

- Step 1-2: The gas does work  $dW'$  on the surroundings in an isothermal expansion and receives heat  $dQ_C$  from the cold reservoir.
- Step 2-3: The gas is worked on by the surroundings with the amount of work  $dW''$  and no heat is transferred while the working fluid temperature is raised from  $T_C$  to  $T_H$ .

**Step 3-4:** The gas is again worked on by the surroundings with the amount of work  $dW$  and heat  $dQ_H$  is transferred isothermally from the gas to the reservoir, also at  $T_H$ .

**Step 4-1:** The gas does work  $dW''$  on the surroundings, no heat is transferred, and its temperature is reduced to  $T_C$ .

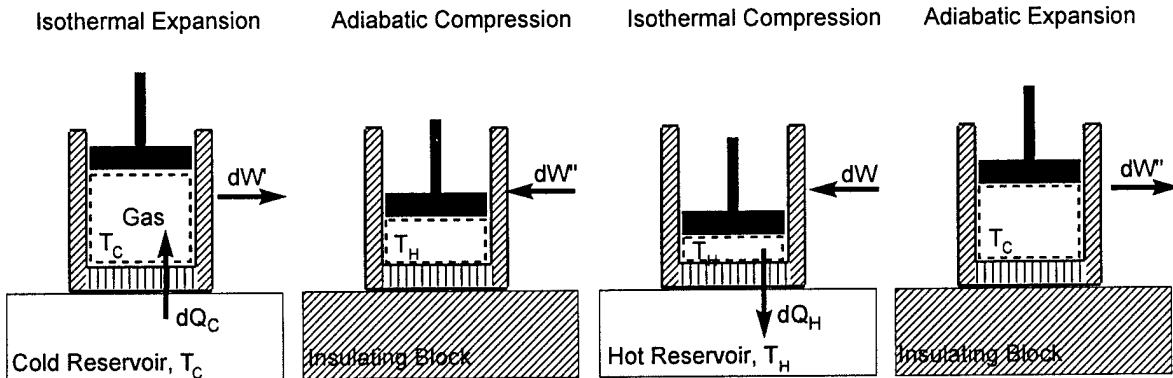


**Figure 2.2:** Carnot cycle using a piston and cylinder

These four steps can be represented on a diagram that plots the pressure of the gas as a function of the volume of the gas — this type of chart is referred to as a *p-v* diagram and is quite standard in thermodynamic engine analysis. The qualitative *p-v* diagram of a Carnot cycle is shown in Fig. 2.3.

The shaded area inside the *p-v* diagram represents the amount of work done in one cycle (the integration of  $p dV$  through a complete cycle). This work can be seen in Fig. 2.2 to be  $dW'' - dW'' + dW - dW'$  which reduces to  $dW - dW'$ . The negative signs mean that work is done by the gas, positive work is defined here as work done to the gas. Because this net work is done to the gas, heat is transferred “uphill” meaning that heat is taken from the cold reservoir and exhausted to the hot, against the grain of Mother Nature. The net amount of heat that is transferred is  $dQ_C + (-dQ_H)$ . Since  $dQ_C < dQ_H$  (see Eq. (2.2) below) the net amount of heat transferred is negative, meaning that a net amount of heat is transferred from the gas to the surroundings. Although there is heat extracted from the cold reservoir to the gas, more heat is exhausted from the gas to the hot reservoir. The

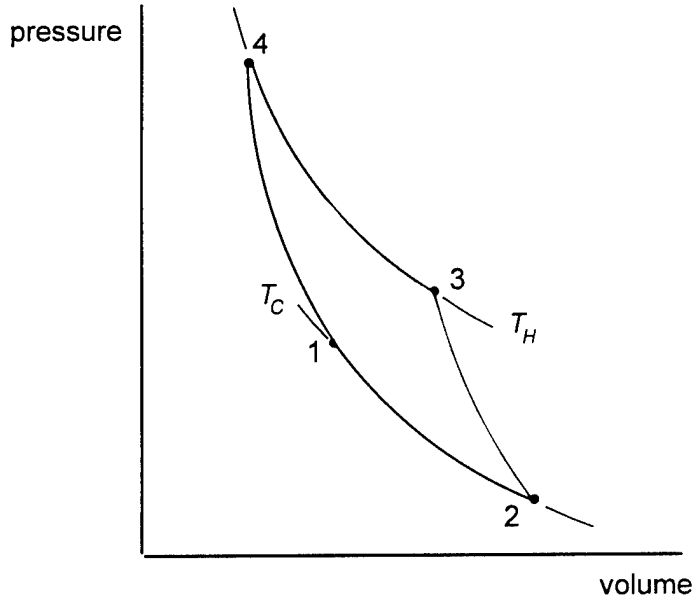


**Figure 2.3:** Carnot  $p$ - $v$  Diagram

magnitudes of these heat transfers are guaranteed by the First Law of Thermodynamics which states that the amount of work done to the gas (or anything inside of a control volume) plus the amount of heat transferred to the gas plus any change in internal energy of the gas must be equal to zero:

$$dQ + dW + dU = 0 \quad (\text{First Law for a control volume}) \quad (2.1)$$

In a thermodynamic cycle that operates at steady state, the state of the system at the end of the cycle must be the same state at which the cycle began. Therefore, the net change in internal energy of the gas  $dU$  must be zero. This fact reduces Eq. (2.1) to the following expression of the First Law.

$$Q_H = (W - W') + Q_C \quad (2.2)$$

The efficiency of a prime mover or the coefficient of performance (COP) of a refrigerator can both be expressed in words as the ratio of "How much energy (in the form that I desire) I get out of the engine compared to how much energy I have to put into the engine." From Fig. 2.1 the efficiency of a prime mover can easily be seen to be  $W/Q_H$  and the COP is  $Q_C/W$  (if

the heat pump is a refrigerator)<sup>†</sup>. The First Law puts no limits on the relative magnitudes of these quantities and from Eq. (2.1) it would appear that if built well, the efficiency of a prime mover or refrigerator could be 100%! However, we know from experience that 100% efficiency is hard to come by. Indeed, there is a fundamental limit of efficiency: the COP of an ideal cycle depends only on the operating temperatures (in this case the temperatures of the thermal reservoirs). This limit is guaranteed by the Second Law of Thermodynamics which requires that the universal amount of entropy ( $\int dQ/T$ ) can only grow or remain the same (much like taxes). The Second Law looks like this for a thermodynamic cycle:

$$\frac{Q_H}{T_H} \leq \frac{Q_C}{T_C} \quad (\text{for a prime mover}) \quad (2.3a)$$

$$\frac{Q_C}{T_C} \leq \frac{Q_H}{T_H} \quad (\text{for a heat pump}) \quad (2.3b)$$

In the Carnot cycle, the amount of entropy generated in one isothermal step exactly balances the entropy decrease in the other step and the adiabatic steps generate no entropy. The Carnot cycle is said to be thermodynamically reversible because no entropy is generated. The solution of these expressions for the First and Second Laws gives a measure of the efficiency or COP of the cycle, and these are:

$$\text{Efficiency (prime mover)} \equiv \frac{W}{Q_H} \leq \frac{T_H - T_C}{T_H} \quad (2.4)$$

$$\text{COP (refrigerator)} \equiv \frac{Q_C}{W} \leq \frac{T_C}{T_H - T_C} \quad (2.5)$$

In general, real engines never get close to this efficiency, and in fact only theoretical thermodynamically reversible engines ever attain an efficiency (or COP) equal to that upper limit. This upper limit of efficiency is called the Carnot efficiency (or Carnot COP for a refrigerator). A cycle is considered to be thermodynamically reversible if all parts of the system are in equilibrium at all time. Some examples of a reversible cycle are the Carnot and Stirling cycles. In order for this Carnot cycle to be reversible, the heat transfer processes from the gas to the thermal bath must take place at only a minuscule temperature difference. Likewise, the adiabatic compressions and expansions must occur over infinitely

---

<sup>†</sup> The difference  $W - W'$  will simply be referred to as  $W$ , the net work done on the gas.

long time periods. These dreamy reversible processes that are called quasi-equilibrium processes really inhibit any power that the cycle might produce if made into a physical engine. Engineers must sacrifice these quasi-equilibrium processes for much faster methods of energy conversion and heat transfers that have irreversibilites, like explosions of gasoline vapor in most automobile engines, free expansion of compressed gas in a household refrigerator and in a thermoacoustic engine, non-zero temperature differences across the heat exchangers. The conversion from an on-paper cycle to a real greasy, rumbling and rattling engine lowers this best-case efficiency, but in exchange lets the engine produce work at a rapid enough rate to be usable. This is a manifestation of the fundamental trade-off between efficiency and power in heat engines and illustrates that the operating point of maximum power output is not the operating point of best efficiency.

Another source of irreversibilites encountered in converting a cycle to an actual engine is the mechanism that provides the phasing of the thermodynamic steps — a mechanism that often makes an otherwise functionally reversible cycle into an engine that can only function in either the prime mover or refrigerator mode. In an automobile engine, the timing belt and piston lever arms (among other things) contribute to the temporal separation of the expansions and compressions of the working fluid. In a conventional refrigerator, check valves and nozzles ensure the flow of refrigerant in the correct direction. Rather than put up with thermodynamic irreversibilities as a necessary evil, a class of reciprocating heat engine cycles called natural engines use these irreversibilites to provide the phasing of the heat and work flows through the cycle<sup>6</sup>.

### 2.1.1. The Natural Engine

This brings us around to the thermoacoustic heat engine — a very elegant natural engine that requires few moving parts because the Good Mother has provided the phasing mechanism for us. The natural heat engine cycle has one fundamental hardware difference with reversible heat engine cycles: the presence of two thermodynamic media. In the thermoacoustic cycle, one medium is the oscillating working fluid (noble gas mixtures, liquid sodium, and air are three examples) and the other is a stationary medium which in Frankenfridge is a set of parallel Mylar<sup>TM</sup> sheets. In a thermoacoustic device, the term coined for this second medium is the *stack* — the term comes from the first thermoacoustic devices which used a stack of parallel plates as the second thermodynamic medium.

The phasing in the thermoacoustic engine is ensured through the fact that the irreversible thermal conduction between the gas and the stack is not instantaneous but takes some finite time which is on the order of one quarter of an acoustic period. This lag between the heat flow and the acoustic gas oscillation is the phase difference that allows the engine to either absorb or generate acoustic work.<sup>†</sup>

The thermoacoustic cycle can be thought of in terms of four distinct stages as illustrated in Fig. 2.4, two adiabatic changes in pressure and two constant pressure heat transfer steps — the four steps which make up the Brayton cycle. In reality, the thermoacoustic cycle differs because the sinusoidal oscillations of the gas are always in contact with the stack which tends to blur the separation of these different steps. However, if these sinusoidal oscillations are replaced with square wave oscillations, the resulting articulated cycle can be more easily described in Fig. 2.4 and in words below:

*Initially:* The stack and gas are at the same temperature,  $T$  and the pressure in the resonator is  $p_0$ . Once the standing wave is introduced, the pressure at the initial position of the gas parcel increases to some value above  $p_0$  which is labeled  $p$ .

*Step 1-2:* The acoustic standing wave does work  $dW''$  on the parcel of gas to both compress it adiabatically to pressure  $p + 2p_1$  and simultaneously translate it a distance  $2x_1$ . The temperature of the gas parcel increases adiabatically by  $2T_1$  due to the pressure rise.

*Step 2-3:* As the gas slows down and stops to change direction, it transfers heat  $dQ_H$  by irreversible thermal conduction to the stack which is at a lower temperature than the gas. This thermal conduction is a constant pressure process which lowers the gas temperature by an amount  $dT$  and increases the volume of the parcel.

*Step 3-4:* The acoustic standing wave picks up the parcel and returns it a distance  $-2x_1$  to its starting place. Because it has moved to a point of lower pressure it expands adiabatically during this move

---

<sup>†</sup> It could be successfully argued that the hot and cold reservoirs in the Carnot cycle constitute a second thermodynamic media. In those terms the difference between the Carnot and the thermoacoustic cycle is that in the thermoacoustic cycle, the first thermodynamic medium (the working fluid) is in constant contact with the second medium (the stack).

and returns energy  $dW''$  to the standing wave in the form of work.

Since the pressure of the parcel has decreased, the temperature is also lowered by an amount  $2T_1$ .

Step 4-1:

The parcel of gas which is again slowing down or at rest while changing direction absorbs heat away from the stack by conduction because it is colder than the region of stack nearest the gas. Because of this conduction, the gas takes up a bigger volume at a pressure  $p$  and returns work  $dW'$  to the standing wave.

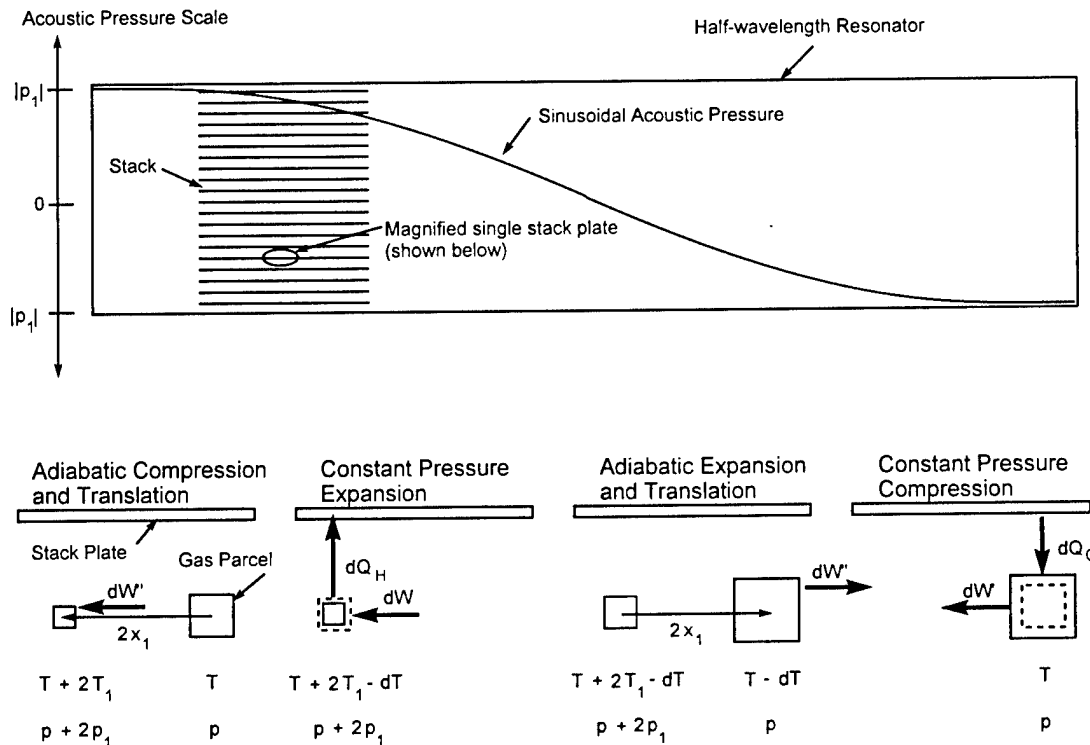


**Figure 2.4:** Articulated thermoacoustic refrigeration cycle in a Lagrangian reference frame

The  $p$ - $v$  diagram for this articulated thermoacoustic cycle, or Brayton cycle, is shown in Fig. 2.5, along with the  $p$ - $v$  diagram for the ideal thermoacoustic cycle where the parcel follows the more realistic sinusoidal motion (as opposed to square wave motion in the articulated cycle description.)

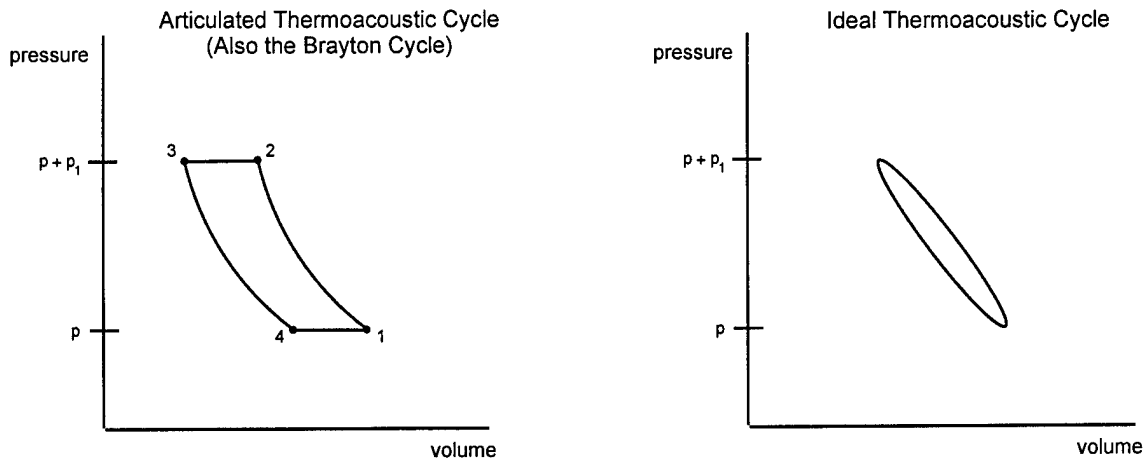


**Figure 2.5:** The  $p$ - $v$  diagrams for the exaggerated and sinusoidal thermoacoustic cycle

The proper phasing in this natural engine, as mentioned above, is ensured because the thermal conduction does not take place instantly, but introduces some time lag between the conduction and the motion/pressure changes. The amount of heat that is conducted from the gas to the stack or vice versa depends upon the distance that separates the gas parcel from the stack in a direction perpendicular to the stack plates. The parcels of gas that oscillate very close to a stack plate transfer heat in a locally isothermal and reversible way while the parcels that are very far away from the plates don't have any thermal contact with the stack and are simply adiabatically expanded and compressed by the standing wave. But, there obviously exists a "sweet spot" where a parcel of gas is far enough away so that thermal contact is poor enough that the heat transfer rate introduces the needed phase relationship, but near enough to not be completely insulated from the stack. This sweet spot is referred to as a thermal penetration depth and is defined as:

$$\delta_\kappa = \sqrt{\frac{2\kappa}{\omega}} \quad (2.6)$$

where  $\omega$  is the angular frequency of the gas oscillation and  $\kappa$  is the thermal diffusivity ( $\kappa = K/\rho_m c_p$  and  $K$  is the thermal conductivity) of the gas. This length can be thought of as the distance that heat can diffuse through the fluid in a time  $\frac{2\pi}{\omega}$ .

Since the acoustic excursion,  $2x_1$ , is on the order of a few millimeters in the Frankenfridge device and the stack is several centimeters long (7.85 cm to be exact), it is apparent

that one parcel of gas doesn't really get the job done of spanning a temperature difference larger than  $2T_1$  or pumping any more heat than a measly  $dQ_C$ ! Because there are many such parcels lined up along the length of the stack, the parcels work like bucket brigade shuttling only a small amount of heat each. The end result can be temperature differences across the stack that have reached  $36^\circ\text{C}$  and heat pumping powers of 30 W in this experiment.

This bucket brigade effect illustrates that an important material property of the stack is low thermal conductivity in the direction of acoustic propagation. If the stack were made of copper it would never be able to sustain a temperature difference across itself — the bucket brigade would be trying to fill a very leaky tub! At the same time, however, the stack must be able to conduct heat in a direction perpendicular to the acoustic flow in order to absorb and release heat to and from the gas parcels. This combination of adequate insulation in a longitudinal direction but sufficient conduction in the lateral direction is more or less satisfied by Mylar<sup>TM</sup> (in the case of this thesis), stainless steel, the ceramic used in catalytic converters and even coffee stirring sticks!

To round out this mostly qualitative discussion of the thermoacoustic cycle, the functionally reversible nature of the cycle should be mentioned. A thermoacoustic device that is attached to a speaker or other type of linear motor can be a refrigerator if this driver excites a standing wave in the resonator. On the other hand, if a temperature difference is imposed across the stack by outside means, the device will produce sound (acoustic work) and will function as a prime mover. Two temperatures are important to the parcel of gas — it's own temperature at the end of an adiabatic compression or expansion and the temperature of the stack at that location. If the parcel is compressed (and heated to a temperature  $T + 2T_1$  by the standing wave), and finds that the stack is hotter than it is, then the stack will transfer heat energy to the parcel. Since the pressure is higher where the parcel is expanded, net work is added to the acoustic standing wave and this is the prime mover mode. On the other hand, if the parcel of gas sees a portion of stack that is colder than it is (the situation illustrated in Fig. 2.4), then the work and heat flows are the opposite of the prime mover and we call this the refrigerator (or heat pump) mode. Obviously then, there must be some stack temperature gradient that is the line of demarcation between a prime mover and a refrigerator. This temperature gradient is called the critical temperature

gradient and is defined as:

$$\nabla T_{crit} = \frac{T_m \beta \omega p_1}{\rho_m c_p u_1}. \quad (2.7)$$

For sinusoidal pressure and velocity oscillations which occur in an acoustic standing wave (and which is assumed throughout this thesis) this ratio  $p_1/u_1$  can be reduced to  $\rho_m a \cot(kx)$  (where  $x$  is the position of the stack in the standing wave relative to the pressure antinode of the fundamental mode and  $k = 2\pi/\lambda$  is the wavenumber). Thermodynamic calculations show that<sup>7</sup>  $\gamma - 1 = T_m \beta^2 a^2 / c_p$ , so that another expression of the critical temperature gradient is:

$$\nabla T_{crit} = \frac{\gamma - 1}{T_m \beta} T_m k \cot(kx). \quad (2.8)$$

Especially for gases,  $(\gamma - 1)/T_m \beta$  is very close to unity (for ideal gases,  $T_m \beta$  is exactly unity) and  $\cot(kx)$  for reasonable stack positions is between 1 and 10 which makes the critical temperature gradient on the order of  $T_m k = 2\pi T_m / \lambda$ . This useful approximation tells us that the critical temperature gradient for the device in this thesis is around  $(290 \text{ K})(3.04 \text{ m}^{-1}) = 882 \text{ K/m}$ . For a stack length of 7.8 cm, the stack temperature difference below which this device is refrigerator and above which it is a prime mover therefore about 70 K.

What happens when the engine operates at this stack temperature difference exactly? As a parcel of gas is compressed, its increase in temperature exactly matches the temperature of the stack along its path and no heat is transferred to the parcel. Operation very close to this critical temperature difference is the most efficient point for the engine; however, this operating point pumps almost no heat in the refrigerator mode or conversely, produces very little work in the prime mover mode. The relationship between stack and parcel temperatures is illustrated below in Fig. 2.6.

A real refrigerator is usually built with a stack and a driver as mentioned above. The stack is housed in a tightly sealed resonator and two heat exchangers are coupled to the ends of the stack. (It is these heat exchangers that are largely responsible for the efficiency decrease in going from an on-paper cycle to a humming engine that can make your beer cold). An important thing to note at this point, only because it has not yet been mentioned explicitly, is that a thermoacoustic refrigerator is operated at the resonance frequency of the combined driver/resonator system. This fact is important because the resonance enhances the acoustic wave generation for a given excursion of the pusher cone — which means that

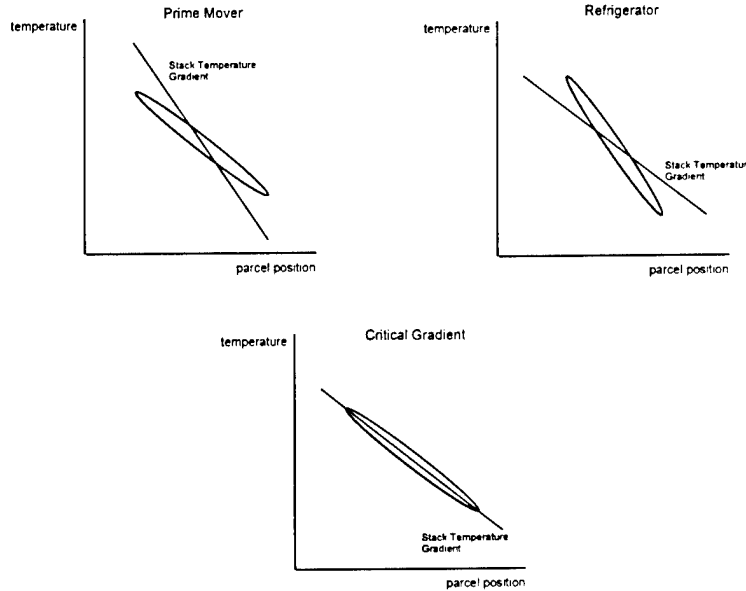


**Figure 2.6:** Relationship of stack and parcel temperatures for heat engine mode determination

the movement of the pusher cone in the driver can be quite small and still generate large acoustic pressure amplitudes. This fact also allows a flexure rather than a sliding seal to be used. Resonant enhancement is a fundamental distinction of the thermoacoustic cycle that is not shared with many other reciprocating heat engine cycles.

## 2.2. Linear Model in DELTAE

### 2.2.1. Introduction of DELTAE

The software package DELTAE (which stands for Design Environment for Low-Amplitude Thermoacoustic Engines<sup>8</sup>) is a text based program written by Drs. Bill Ward and Gregory Swift at Los Alamos National Laboratory that estimates the performance of a thermoacoustic device. A model in DELTAE comprises a series arrangement of transducers (drivers), ducts, heat exchangers, thermoacoustic stacks, and compliances (or any impedance transition.) For each of these segments, the computer solves a one dimensional wave equation with temperature evolution by matching the pressure, volume velocity and temperature at the interface of each segment as boundary conditions. In thermoacoustic elements (the



sameas	0	Gas type	0.0000	D	Ph(U)	deg	
ideal		Solid type	0.1434	E	Hdot	W	
			0.1434	F	Work	W	
			-8.8274E-04	G	HeatIn	W	
!----- 2 -----							
ISODUCT Bellows							
2.0480E-03	a	Area	m^2	4492.6	A	p	Pa
0.3654	b	Perim	m	-5.9538E-02	B	Ph(p)	deg
1.8900E-02	c	Length	m	2.0561E-04	C	U	m^3/s
				-72.353	D	Ph(U)	deg
				0.1405	E	Hdot	W
sameas	0	Gas type	0.1405	F	Work	W	
ideal		Solid type	-2.9039E-03	G	HeatIn	W	
!----- 3 -----							
ISODUCT Insulating Ring							
2.9090E-03	a	Area	m^2	4490.8	A	p	Pa
1.1480	b	Perim	m	-6.5926E-02	B	Ph(p)	deg
3.0200E-03	c	Length	m	2.4846E-04	C	U	m^3/s
				-75.637	D	Ph(U)	deg
				0.1390	E	Hdot	W
sameas	0	Gas type	0.1390	F	Work	W	
ideal		Solid type	-1.4552E-03	G	HeatIn	W	
!----- 4 -----							
ISODUCT Interface							
1.1950E-03	a	Area	m^2	4466.7	A	p	Pa
0.1988	b	Perim	m	-0.1322	B	Ph(p)	deg
1.2700E-02	c	Length	m	3.2299E-04	C	U	m^3/s
				-79.108	D	Ph(U)	deg
				0.1379	E	Hdot	W
sameas	0	Gas type	0.1379	F	Work	W	
copper		Solid type	-1.0722E-03	G	HeatIn	W	
!----- 5 -----							
ISODUCT HX Flange							
1.1400E-03	a	Area	m^2	4393.8	A	p	Pa
0.1240	b	Perim	m	-0.2774	B	Ph(p)	deg
2.6240E-02	c	Length	m	4.6986E-04	C	U	m^3/s
				-82.675	D	Ph(U)	deg
				0.1366	E	Hdot	W
sameas	0	Gas type	0.1366	F	Work	W	
copper		Solid type	-1.3848E-03	G	HeatIn	W	
!----- 6 -----							
HXFRST Exhaust HX							
1.1400E-03	a	Area	m^2	4344.3	A	p	Pa
0.5000	b	GasA/A		-0.2524	B	Ph(p)	deg
6.3500E-03	c	Length	m	4.8958E-04	C	U	m^3/s
2.5400E-04	d	y0	m	-83.295	D	Ph(U)	deg
-0.2366	e	HeatIn	W	-0.1000	E	Hdot	W

295.10	f	Est-T	K	(t)	0.1288	F	Work	W
sameas	0	Gas type			-0.2366	G	Heat	W
ideal		Solid type			297.32	H	MetalT	K
!----- 7 -----								
STKSLAB	Stack							
1.1100E-03	a	Area	$m^2$		3723.2	A	p	Pa
0.7730	b	GasA/A			1.2014	B	Ph(p)	deg
7.8500E-02	c	Length	m		8.3121E-04	C	U	$m^3/s$
1.9100E-04	d	y0	m		-88.138	D	Ph(U)	deg
7.6200E-05	e	Lplate	m		-0.1000	E	Hdot	W
					1.7844E-02	F	Work	W
					297.44	G	T-beg	K
sameas	0	Gas type			257.31	H	T-end	K
mylar		Solid type			-0.1110	I	StkWrk	W
!----- 8 -----								
HXLAST	Cold HX							
1.1400E-03	a	Area	$m^2$		3684.3	A	p	Pa
0.5000	b	GasA/A			1.2823	B	Ph(p)	deg
2.5400E-03	c	Length	m		8.3796E-04	C	U	$m^3/s$
2.5400E-04	d	y0	m		-88.196	D	Ph(U)	deg
0.1000	e	HeatIn	W	= 8G?	0.0000	E	Hdot	W
280.00	f	Est-T	K	(t)	1.4055E-02	F	Work	W
sameas	0	Gas type			0.1000	G	Heat	W
copper		Solid type			257.34	H	MetalT	K
!----- 9 -----								
INSCONE	Cold Reducer							
sameas	8a	a Areal	$m^2$		3572.6	A	p	Pa
0.1197	b	PerimI	m		1.2748	B	Ph(p)	deg
9.2200E-03	c	Length	m		8.6546E-04	C	U	$m^3/s$
3.8350E-04	d	AreaF	$m^2$		-88.220	D	Ph(U)	deg
6.9420E-02	e	PerimF	m		0.0000	E	Hdot	W
sameas	0	Gas type			1.3622E-02	F	Work	W
copper		Solid type			0.0000	G	HeatIn	W
!----- 10 -----								
INSDUCT	Cold Duct							
sameas	9d	a Area	$m^2$		352.16	A	p	Pa
sameas	9e	b Perim	m		0.3915	B	Ph(p)	deg
0.1400	c	Length	m		9.8603E-04	C	U	$m^3/s$
					-88.335	D	Ph(U)	deg
					0.0000	E	Hdot	W
sameas	0	Gas type			3.8601E-03	F	Work	W
copper		Solid type			0.0000	G	HeatIn	W
!----- 11 -----								
INSCONE	Horn							
sameas	10a	a Areal	$m^2$		841.36	A	p	Pa
sameas	10b	b PerimI	m		-178.22	B	Ph(p)	deg
6.9220E-02	c	Length	m		9.6987E-04	C	U	$m^3/s$

```

7.4320E-04 d AreaF    m^2          -88.340  D Ph(U)    deg
9.6630E-02 e PerimF   m            0.0000  E Hdot      W
sameas 0  Gas type
copper    Solid type          8.8184E-04 F Work      W
                                0.0000  G HeatIn    W
!---- 12 -----
COMPLIANCE Bulb
6.8300E-02 a Area    m^2          841.36   A |p|      Pa
1.0310E-03 b Volum   m^3          -178.22   B Ph(p)    deg
                                1.7848E-09 C |U|      m^3/s
                                -76.437   D Ph(U)    deg
                                -1.5328E-07 E Hdot      W
sameas 0  Gas type
stainless  Solid type          -1.5328E-07 F Work      W
                                -1.5328E-07 G HeatIn    W
!---- 13 -----
HARDEND  End Impedance
0.0000  a R(1/Z)      =13G?    841.36   A |p|      Pa
0.0000  b I(1/Z)      =13H?    -178.22   B Ph(p)    deg
                                1.7848E-09 C |U|      m^3/s
                                -76.437   D Ph(U)    deg
                                -1.5328E-07 E Hdot      W
                                -1.5328E-07 F Work      W
                                -1.8297E-08 G R(1/Z)
sameas 0  Gas type          8.7741E-08 H I(1/Z)
ideal      Solid type          257.31   I   T      K

```

The numbered segments that are separated by dashed lines are the series representation of the elements of the Frankenfridge device. The characters in the upper left hand corner of the segment are the DELTAE name for the type of segment. Some terms are complete and their meaning is obvious. The ones that are not follow<sup>9</sup>:

ISODUCT                    a duct that is constrained to be isothermal by an energy source or sink not accounted for by DELTAE.

INSDUCT                    a duct that is insulated. The heat generated by the thermoviscous losses in this type of segment is transported onto the nearest heat exchanger so that DELTAE calculations of coefficient of performance reflect this deleterious effect.

HXRST                    the first heat exchanger in a system. For a quarter wavelength device with the stack nearest the pressure antinode, this heat exchanger is the hot side heat exchanger. In a heat pump, this exchanger dumps the exhaust heat plus work (enthalpy) from the device.

HXLAST	this is the heat exchanger on the other side of the stack. In the Frankenfridge configuration this is the cold side heat exchanger, or the heat exchanger that takes on the heat that the device is obligated to move. Since it is followed by <b>INSDUCT</b> segments, it also absorbs the thermoviscous power generated in these segments.
STKSLAB	the thermoacoustic stack. There are many varieties of stacks, many of which DELTAE is capable of modeling. The <b>STKSLAB</b> segment is for modeling a parallel plate type stack.
INS/ISOCONE	just like the duct, but has an initial cross sectional area that is larger or smaller than its final cross sectional area.
COMPLIANCE	a series impedance that is an acoustic volume. Unlike the ducts and cones which have both thermal and viscous losses, the compliance only has thermal losses.
HARDEND	this ends a device with a rigid termination that requires that the volume velocity of the working fluid be identically zero.

The \*.out file is divided into two columns: the column on the left is the input column while the column on the right is the output column which displays the results after the program is executed. Notice that these quantities in the output column have a capital letter to designate them. For example, the phase of the acoustic pressure that DELTAE calculates in segment 8 would be denoted as quantity '8B.' In the input column, the quantities that describe the geometry and initial values pertinent to each segment are designated with a lower case letter. The ratio of the cross sectional area available for fluid flow to the total cross sectional area in the cold heat exchanger is denoted as quantity '8b.' (Remember that the fins of a heat exchanger occlude some fraction of the cross sectional area.)

It is from the input column of the model file that the Guess and Target vectors come. As mentioned above, a Guess is a parameter that the user allows DELTAE to vary in order to get the Target parameter to match the user specified value. A convenient way to think about the Guesses and Targets is to consider a Target to be something that we think of as an experimentally controlled variable or a given in the problem. A Guess is something that we might consider to be an experimental result. The Guesses are used as input to the DELTAE solver and a Target is a variable that DELTAE computes on every iteration.

In the Frankenfridge model as it stands here, there are two entries each in the Guess and Target vectors. As one might imagine, these vectors must be balanced: there must be as many Targets as there are Guesses. The Guesses are denoted in the input column with a capital G next to the parameter of a segment. The values that DELTAE converges upon for the Guess parameters after a run appear in the output column in segment 0. Possible Targets are delineated in the input column with a lower case 't' in parentheses, (t), next to a parameter in a segment. A parameter that has been chosen to be part of the Target vector is noted in the input column with an equal sign, followed by the parameter in the output side that functions as a comparator and ends with a question mark. For example, in the Frankenfridge model, the real part of the admittance at the **HARDEND** is a target that should have the value of 0 (we define this condition to ensure that a standing wave exists in the resonator). This Target is marked with '=13G?' to show that it is a Target and should be compared to parameter 13G in the output column.

### 2.2.3. A More Detailed Look at the DELTAE Solver

The DELTAE software models acoustic wave propagation, with temperature evolution, by integrating the coupled differential equations (shown in the paragraphs below) from the model's **BEGIN** segment to the **HARD** or **SOFT END** segment with respect to five variables<sup>9</sup>: real mean temperature  $T_m(x)$ , complex acoustic pressure  $p_1(x)$ , and complex acoustic volume velocity,  $U_1(x)$ . For each segment, the algorithm uses the differential equation that governs that type of segment, using the segment specific (local) user defined variables like geometry and required enthalpy flow and model (global) variables like mean pressure and frequency. The boundary conditions used for the solution are the continuity of temperature, pressure and volume velocity at segment junctions.

If these boundary conditions are known at the beginning of each segment, then this process is very simple. However, the power of DELTAE is that the user can specify a boundary condition (or Target) anywhere in the model, even at the end of the last segment of the model. In the Frankenfridge model, the admittance at the **HARDend** segment is pinned to be zero (This is the equivalent of specifying the volume velocity equal to zero at the wall.) So, lacking enough definite boundary values at the beginning of the **BEGIN** segment, DELTAE uses a shooting method whereby the algorithm "guesses" the value of the unknown quantities and then comparing the finished calculation results with the Target vectors. In

this way, the algorithm converges to a solution specified by the user. In fact, DELTAE forms a non-linear system of equations from the Target vector and massages the Guess vector so that the difference between the Targets and the results of the calculation are within a user specified tolerance. The routine that performs this part of the simulation is called DNSQ and is part of the SLATEC Common Mathematical Library at <http://www.netlib.org>. This algorithm is a modification of the Powell hybrid method.<sup>9</sup>

Instead of integrating one equation — the wave equation with temperature evolution — DELTAE uses three uncoupled equations: a modified form of Euler's Equation, a modified form of the continuity of mass equation and an expression of heat transfer that describes the mean temperature distribution in the gas. In order to present the way that DELTAE simulates a thermoacoustic device, let's study the wave equation with thermoviscous losses (the irreversibility that makes the thermoacoustic cycle a useful heat engine) as it applies in a standing wave resonator with a plate inserted at some point in the standing wave<sup>10</sup>.

The plate is long in the direction of acoustic propagation and has width but has negligible thickness. We'll call the direction of propagation the  $x$  direction. The dimension normal to the plate is the  $y$  direction and the width of the plate is in the  $z$  direction.

The conservation of momentum expression that includes viscous losses is:

$$\langle u_1 \rangle = \frac{i}{\omega \rho_m} (1 - f_\nu) \frac{dp_1}{dx} \quad (2.9)$$

The term  $f_\nu$ , which is the spatial average of  $h_\nu$ , is called by the thermoacoustic community a *Rott function in viscosity*<sup>7</sup> and it describes how viscosity reduces the magnitude of the oscillatory velocity near the plate and shifts its phase. For flow along a plate not near an edge of the plate, (near the middle of a parallel plate stack geometry, for example) this effect is most prevalent. In the modified Euler's Equation (Eq. (2.9)) above, the term  $(1 - f_\nu)$  alters the oscillatory velocity so that gas that is much closer than a viscous penetration depth ( $\delta_\nu$ ) to the nearest solid surface (right next to the surface) is almost at rest. Likewise, a parcel of gas that is oscillating much farther than  $\delta_\nu$  from the surface "feels" no viscous shear at all and has no spatial dependence in the  $y$  or  $z$  directions. A parcel of gas that oscillates near a viscous penetration depth away from the wall, however, does so with reduced velocity and a non-trivial phase shift that opposes phasing of the thermoacoustic transport. It is much easier, both analytically and computationally, to consider the spatial average in  $y$  rather than to retain the functional dependence since this reduces the integration to only

a one dimensional problem. The spatial average of the Rott function for velocity follows in Eq. (2.10).

$$f_\nu = \frac{\tanh \left[ (1 + i) y_0 / \delta_\nu \right]}{(1 + i) y_0 / \delta_\nu} \quad (2.10)$$

Here,  $y_0$  is half of the stack plate spacing. Note that Eq. (2.10) only includes a geometrical parameter and a penetration depth,  $\delta_\nu$ . The viscous penetration depth, like the thermal penetration depth defined in Eq. (2.6), defines the length of the effective boundary layer and is inversely proportional to the square root of frequency.

The conservation of mass equation that is relevant to thermoacoustic heat transport includes both viscous and thermal dissipation:

$$\frac{d\langle u_1 \rangle}{dx} = -\frac{i\omega}{\rho_m a^2} \left[ 1 + (\gamma - 1) f_\kappa \right] p_1 + \frac{(f_\kappa - f_\nu)}{(1 - f_\nu)(1 - \sigma)} \frac{1}{T_m} \frac{dT_m}{dx} \langle u_1 \rangle \quad (2.11)$$

Here,  $f_\kappa$  is equivalent to  $f_\nu$  except that it involves the thermal penetration depth rather than the viscous. That is, thermal contact with the solid reduces the magnitude of the temperature oscillations in the  $x$  direction and introduces a significant phase shift. Explicitly, a parcel of gas that is much less than a penetration depth away from the surface is nearly isothermal and those far away from the boundary layer expand and contract adiabatically in phase with the pressure oscillations. Those parcels at about a penetration depth from the surface are at neither extreme and experience magnitude reduction and a phase shift (that aids the thermoacoustic transport) with respect to the pressure oscillations. Since both temperature and velocity fluctuations affect the density gradient in the direction of acoustic propagation, both viscous and thermal terms make their appearance in the continuity equation. The first term in the right hand side of Eq. (2.11) describes the density fluctuations due to pressure oscillations of the gas (and involves only thermal loss) while the second term includes the density oscillations due to velocity and includes both thermal and viscous loss.

To complete the system of equations that combine to form the wave equation for thermoacoustics (Rott's wave equation), the temperature profile that appears in Eq. (2.11) must be described:

$$\begin{aligned} \frac{dT_m}{dx} = & \left\{ \frac{\dot{H}}{A_{gas}} - \frac{1}{2} \Re \left[ p_1 \langle \tilde{u}_1 \rangle \left( 1 - \frac{(f_\kappa - f_\nu)}{(1 - \tilde{f}_\nu)(1 + \sigma)} \right) \right] \right\} \div \\ & \left\{ \frac{\rho_m c_p |\langle u_1 \rangle|^2}{2\omega (1 - \sigma^2) |1 - f_\nu|^2} \Im \left( f_\kappa + \sigma \tilde{f}_\nu \right) - \kappa - \frac{A_{solid}}{A_{gas}} \kappa_{solid} \right\} \end{aligned} \quad (2.12)$$

While this is not as intuitively obvious as the two familiar conservation equations, this equation can be loosely explained physically as follows. The last two terms in the denominator account for the thermal conduction losses in the direction opposite useful heat transfer along the stack: one term for conduction in the gas and one for conduction in the solid. The second term in the numerator represents the acoustic intensity in the standing wave and also accounts for the magnitude and phase complexities within the boundary layer. The first term in the denominator is tricky but basically it represents the internal energy and kinetic energy that is convected along the temperature gradient. This equation is very muddled and it is difficult to get an intuitive feel for it by considering it term by term. A more intuitive feel for thermoacoustic theory can be had by considering the "Short Stack" approximation found in Swift's 1988 paper (Ref. 7) that presents a better explanation of the subtle points involved in these equations.

The point of all of this is to get an understanding of what DELTAE uses to model the thermoacoustic cycle. It has been stated that the program numerically integrates the 1-D wave equation. In fact, it integrates these three coupled equations, in only one dimension, using a Runge-Kutta technique. This is such a simple problem that it takes no time at all for the computer to perform and ultimately contributes to the usefulness of DELTAE. The user can create a model and see the results of a simulation in less than a second on a Pentium™ processor. Once the user understands how the program works, he or she can use it much more effectively; that is, since it uses a shooting method to fill in the unknown boundary conditions it can get "off the track" quite easily if the user lets the model start at non-realistic or non-intelligent places. It is very frustrating for the new user who may not have much experience with thermoacoustic refrigerators to know what these realistic conditions are. Also, big changes in the parameters can cause DELTAE to have a hard time converging. A big change in gas mixture or driving frequency can drive the model to either an instability or a mode that doesn't make any physical sense. In these cases the new user must be careful — the program conveys little warning if it has converged to a non-meaningful solution. By checking the heat fluxes in the heat exchangers and work flux along stack for violations of energy conservation as well as making a reality check of the heat exchanger and gas temperatures, the user can guard against accepting a garbage solution.

## Chapter 3.

# Frankenfridge Instrumentation

---

---

This chapter will detail the instrumentation used to collect data about the performance of Frankenfridge. The data that is collected using this instrumentation has proven to be quite “clean,” repeatable and consistent with expected results based on STAR performance. The first section outlines the signal paths for each sensor. Because the measurement of exhaust heat is new for the STAR resonator (and is exciting at such low power levels), a section is included here that outlines the design, instrumentation and calibration of the exhaust heat sink flange. The last section briefly overviews the LabVIEW<sup>TM</sup> Data Acquisition system. One purpose of this chapter is to provide a resource for future experimenters working with the Frankenfridge device, or some modification thereof, and for that reason may be otherwise inexcusably dense. The manufacturer’s calibration sheets for the sensors described below can be found in Appendix C.

To better understand the instrumentation, that for the most part measures the flow of heat and work in Frankenfridge, it is important for the reader to have an overall idea of this energy flux. The diagram shown in Fig. 3.1 illustrates the paths of energy flow.

### 3.1. Sensors and Signal Paths

The numbered paragraphs below describe the instrumentation at the corresponding numbered point on Fig. 3.2.

1. **SETAC Driver:** The SETAC driver contains two sensors, a microphone and an accelerometer, that are central to the measurement of Frankenfridge acoustic input power,  $\dot{W}_{ACS}$  in Fig. 3.1.

1.1. The microphone is an Endevco Model 8514-10 (SN: Not available).

The sensor is a piezoresistive “strain gauge” type that requires an ultra-stable bias supply to power the four-arm strain gauge Wheatstone bridge that is doped on a silicon diaphragm. This bias supply, as well as the pre-amplification of its signal is accomplished with a very nice circuit constructed in the lab. See Appendix C for

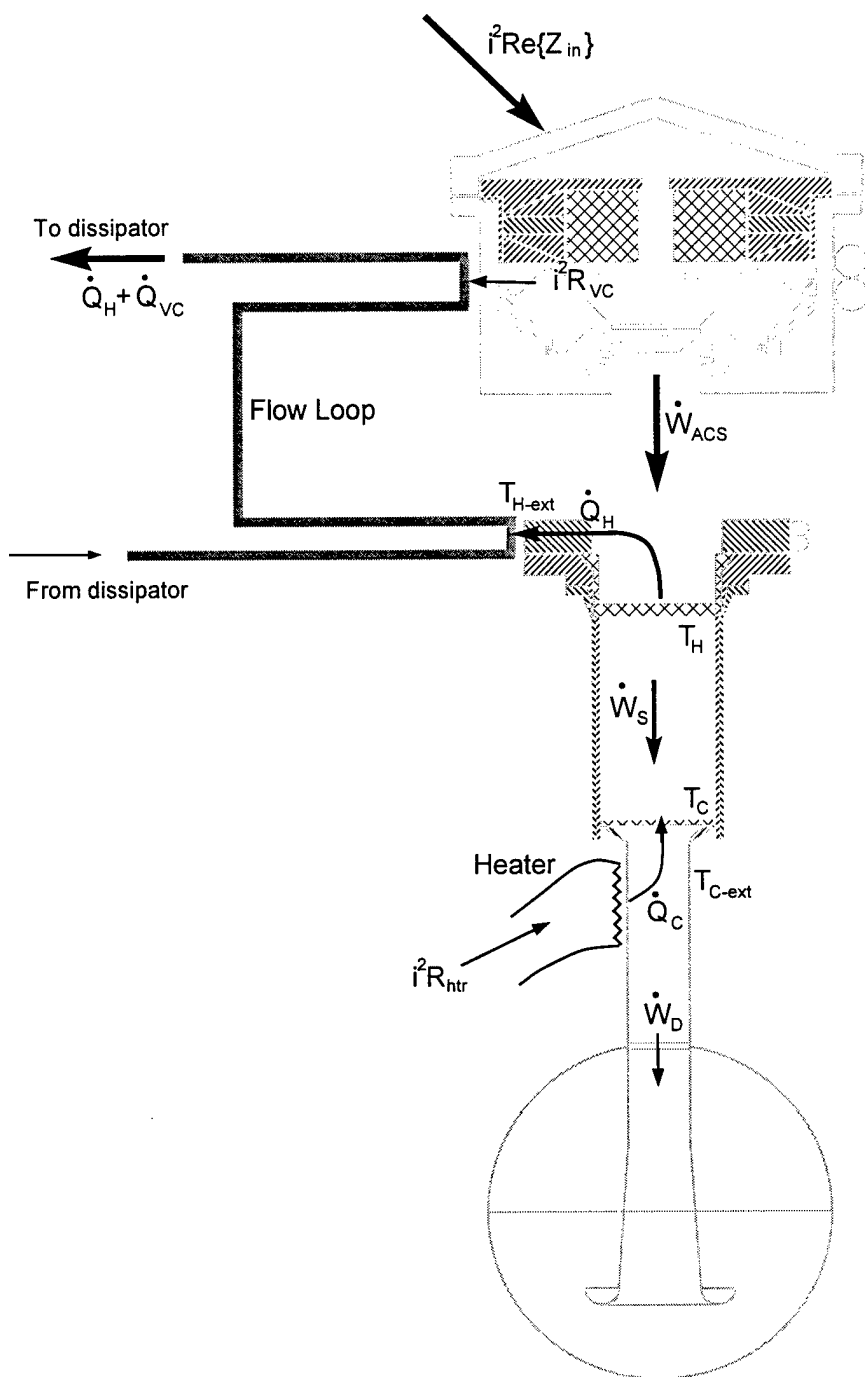


**Figure 3.1:** Cross-sectional view of Frankenfridge showing work and heat flow.

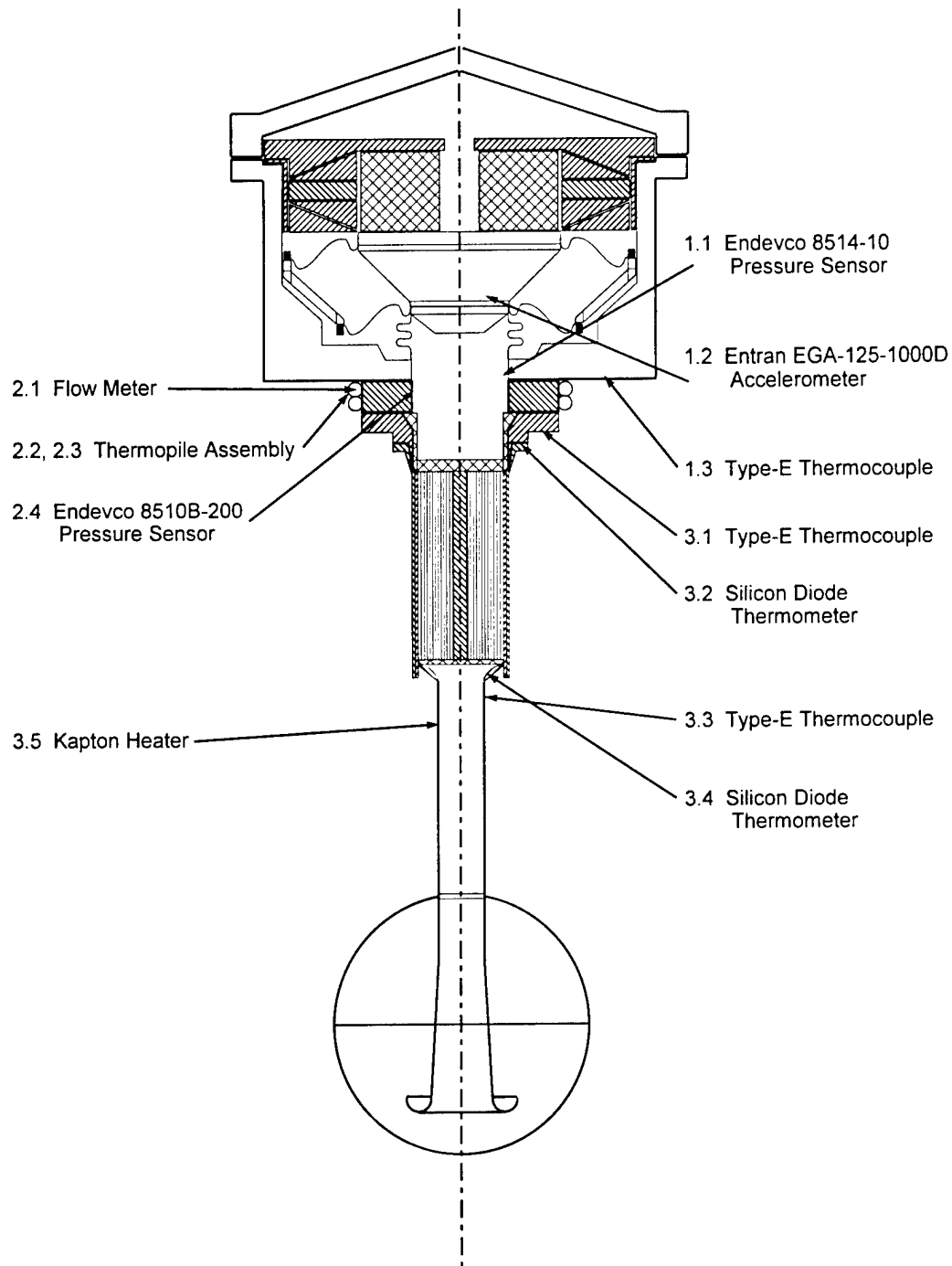


**Figure 3.2:** Cross-sectional view of Frankenfridge showing sensor locations.

a complete description and of this preamp, the PR100. The Endevco 8514 is a subminiature design that has a diameter of 1.65 mm and is mounted in the aluminum driver housing. It is a differential pressure gauge and its reference port is vented to a small volume which is connected to the back volume of the driver through a small capillary leak. This venting arrangement, which acts as an acoustic low pass filter, lets the sensor sense the acoustic pressure oscillations on its diaphragm but not the large static pressure in the resonator since the back volume of the microphone is allowed to equilibrate to the back volume of the driver. (The resonator and the back volume of the driver are also in static pressure equilibrium via a separate capillary.) For this reason, the pressure sensor can have a small range of only  $\pm 10$  psia and therefore a higher sensitivity than a sensor that would have to carry the static pressure as well as the acoustic pressure. The measured sensitivity of this microphone is  $3.45 \mu\text{V}/\text{Pa}$  at 250 Hz. See Section 3.1.1 for the calibration history of this sensor. The nominal factory calibration is reported as  $30 \pm 10 \text{ mV}/\text{psi} = 4.35 \pm 1.45 \mu\text{V}/\text{Pa}$ .

- 1.2. The accelerometer is an Entran Model EGA-125-1000D (SN: Not available). The Entran is also a piezoresistive strain gauge device based on a semiconductor Wheatstone bridge. It has a very miniature but robust package that is  $6.86 \text{ mm} \times 3.56 \text{ mm} \times 3.56 \text{ mm}$ . The accelerometer also uses the PR100 ultra-stable bias supply and preamp mentioned previously. The sensor is mounted on the pusher cone assembly (the side that faces away from the resonator). The sensor has a range of  $\pm 1000 \text{ g} = \pm 9800 \text{ m/s}^2$  and a measured (see Section 3.1.1) sensitivity of  $23.2 \frac{\mu\text{V}}{\text{m/s}^2}$  at 15 V bias. The factory calibration at 15 V bias is reported to be:  $0.222 \text{ mV/g} = 22.6 \frac{\mu\text{V}}{\text{m/s}^2}$ . Since the PR100 supplies a 10 V bias, not 15 V, the measured scaled sensitivity is  $15.5 \frac{\mu\text{V}}{\text{m/s}^2}$  (at 10 V bias).

1.3. The driver is also equipped with a self adhesive Omega No. SA1-E Type-E thermocouple mounted on the face on which the resonator attaches. This thermocouple serves to monitor possible heat leak to and from the driver to the exhaust heat sink flange as well as to make sure that the driver does not overheat. This thermocouple voltage is read with the Keithley 740.

**2. Exhaust Heat Sink Flange:** The flow loop that encircles the copper exhaust heat sink is instrumented with five sensors: a flow meter, a thermopile, two thermocouples and a pressure sensor. The main function of this flange is to measure the exhaust heat flux,  $\dot{Q}_H$  in Fig. 3.1. Since the acoustic power is measured, knowledge of the exhaust heat and the First Law of Thermodynamics is adequate to determine the heat pumping power from resonator's cold end.

2.1. The flow meter is a Hedland IR-OPFlow Model 502-101 (SN: none) which is an axial paddle wheel (Pelton wheel) turbine type flow meter. The sensor has an infrared transmitter and receiver molded into the body of the meter that provides a square wave output signal whose frequency is directly proportional to flow rate (1 pulse per rotation). The amplitude of the square wave is 1.2 V below the DC bias voltage supplied to the sensor which can be between 5 V and 15 V. Because of an unknown sensitivity of the sensor to line pressure, this sensor is calibrated *in situ*.

2.2. The thermopile is a ten junction Type-T thermopile. Its construction is very similar to that outlined in Appendix A of the Master of Science Thesis by Richard Russel<sup>11</sup> except that Russel used a six junction pile. The sensitivity of the ten junction pile is measured to be  $396.5 \mu\text{V}/^\circ\text{C}$  by pouring water of known temperature through one leg and keeping the other leg at the measured room temperature and recording the thermopile voltage response and the known temperature difference. Theoretically, since a Type-T junction has a nominal sensitivity of  $40 \mu\text{V}/^\circ\text{C}$  at  $27^\circ\text{C}$ , the ten junction pile should have a sensitivity of  $400 \mu\text{V}/^\circ\text{C}$  at that

temperature. The pile voltage is read with the Keithley 740 Thermocouple Reader. Even though each thermocouple junction in the pile is mounted to the copper tubing and therefore measures the tubing temperature, the tubing has such a low thermal resistance that it is assumed the temperature drop across the tubing is negligible and the tubing temperature is the water temperature.

- 2.3. The thermopile is also outfitted with Type-E thermocouples on the inlet and discharge tubes. The voltage from these thermocouples are read with the Keithley 740 as well.
- 2.4. The pressure sensor mounted on this flange has nothing to do with measurements of exhaust heat flux, but is just a convenient place to mount a differential pressure sensor that is vented to the atmosphere. This Endevco Model 8510B-200 (SN: 10063) is vented to the atmosphere so that it will measure the static gauge pressure in the resonator (as well as the acoustic fluctuations). The range of this sensor is 200 psi and therefore has a lower sensitivity than the microphone in the driver. Because of this fact, the flange microphone is primarily used to monitor the static pressure in the resonator and provides a cross-calibration transfer standard for the driver microphone (this calibration procedure is described in Section 3.1.1). The Endevco 8510B-200 is a piezoresistive sensor like the 8514-10 except that it has a larger package and mounts snugly in a 10 – 32 tapped hole. Like the 8514-10, the 8510B-200 uses the PR100 bias supply/preamplifier. The AC sensitivity of this sensor is measured to have an AC response of 203.9 nV/Pa and a DC offset of 19.92 mV (see Section 3.1.1). The manufacturer claims the AC sensitivity is 1.45 mV/psi = 210.3 nV/Pa at a 10.00 V<sub>dc</sub> bias.
3. **The STAR Resonator:** The STAR resonator in Frankenfridge is instrumented in much the same way as it was as part of STAR.

- 3.1. The hot side thermocouple is an Omega No. WTE-14-60 screw mounted Type-E and its voltage is read by the Keithley 740.
- 3.2. The hot side silicon diode thermometer that was used when STAR flew on *Discovery* seems to no longer be accurate and is not used for Frankenfridge measurements.
- 3.3. The cold side thermocouple is a self adhesive Omega No. SA1-E Type-E and is, of course, read with the Keithley 740.
- 3.4. The cold side silicon diode thermometer also seems to have lost some accuracy, possibly due to the space-qualified “goop” that enclosed all exposed electrical components for spark suppression. The biggest reason that they are not used is that they don’t seem to agree with each other at ambient conditions.
- 3.5. The Minco Kapton resistance heater that is attached to the cold side duct just under the stack has a nominal room temperature resistance of  $52 \Omega$  and changes slightly with temperature ( $\pm 0.5 \Omega$ ) as it dissipates up to 30 W. The voltage and current supplied to the heater are measured to know precisely the electrical heat load supplied on the resonator’s cold side,  $\dot{Q}_C$  in Fig. 3.1.

These signals are all measured with two instruments, the HP 3457A Multimeter, and the Keithley 740 Thermocouple reader. The HP 3457A contains the 44491A Scanner Card that allows the instrument to scan up to ten channels of AC or DC voltage, AC or DC current, resistance and frequency. The signals that are routed to the HP 3457A include:

- Driver Pressure Sensor, from the Endevco 8514-10, amplified by the PR100 to produce an AC voltage
- Driver Accelerometer, from the Entran EGA-125-1000D, amplified by the PR-100 to produce an AC voltage
- Flange Pressure Sensor, from the Endevco 8510B-200, conditioned by the PR100 to produce a DC voltage
- Flow Meter, Hedland IR-OPFlow 502-101, Frequency
- Acoustic Driving Frequency, from HP 3314A Function Generator, Frequency
- Kapton Heater supply voltage, DC voltage

- Kapton Heater supply current, DC current

The signals from the thermocouples and thermopile are read with a Keithley 740 Thermocouple Reader with an optional 7057A Scanner Card that allows the Keithley to scan up to nine channels of thermocouple signals. The Keithley provides a silicon based cold junction compensation and conversion of the thermocouple voltage to a temperature in either degrees Fahrenheit or Celsius. For a thermopile signal that requires no cold junction compensation or conversion to a temperature scale, the Keithley will measure and report the tiny voltage produced by the thermopile directly in millivolts with a resolution of  $\pm 1 \mu\text{V}_{\text{dc}}$ . The signals that are routed to the Keithley include:

- Cold Side Thermocouple, Type-E
- Hot Side Thermocouple, Type-E
- Thermopile Thermocouple, Discharge side, Type-E
- Thermopile Thermocouple, Intake side, Type-E
- Thermopile voltage, Voltage
- Driver Thermocouple, Type-E
- Bath Thermocouple, Type-E (see following section that describes the exhaust heat sink flange)

A diagram of the signal paths of all of the sensors that are part of Frankenfridge is shown in Fig. 3.3.

### 3.1.1. Sensor Calibration History and Cross-Checks

The Entran accelerometer attached to the driver's pusher cone was calibrated by comparison to an Entran model EGA-125-1000D (SN: 92J91G12-P06), which is an accelerometer that is used only as a reference. This reference accelerometer was calibrated with a B & K Calibration Exciter Type 4294 (SN: 1759853). Further confidence is assured by checking the Calibration Exciter with a B & K Accelerometer Type 4382 (SN: 1504375) which has been calibrated by the National Institute for Standards and Technology (NIST). These two calibration routines were performed twice, once on January 17, 1997, before serious measurements began and again on March 10, 1998 after most of the measurements were complete. These two calibrations show that over the course of a year or more the Entran accelerometer mounted in the driver has become 5% less sensitive. The Calibration Exciter

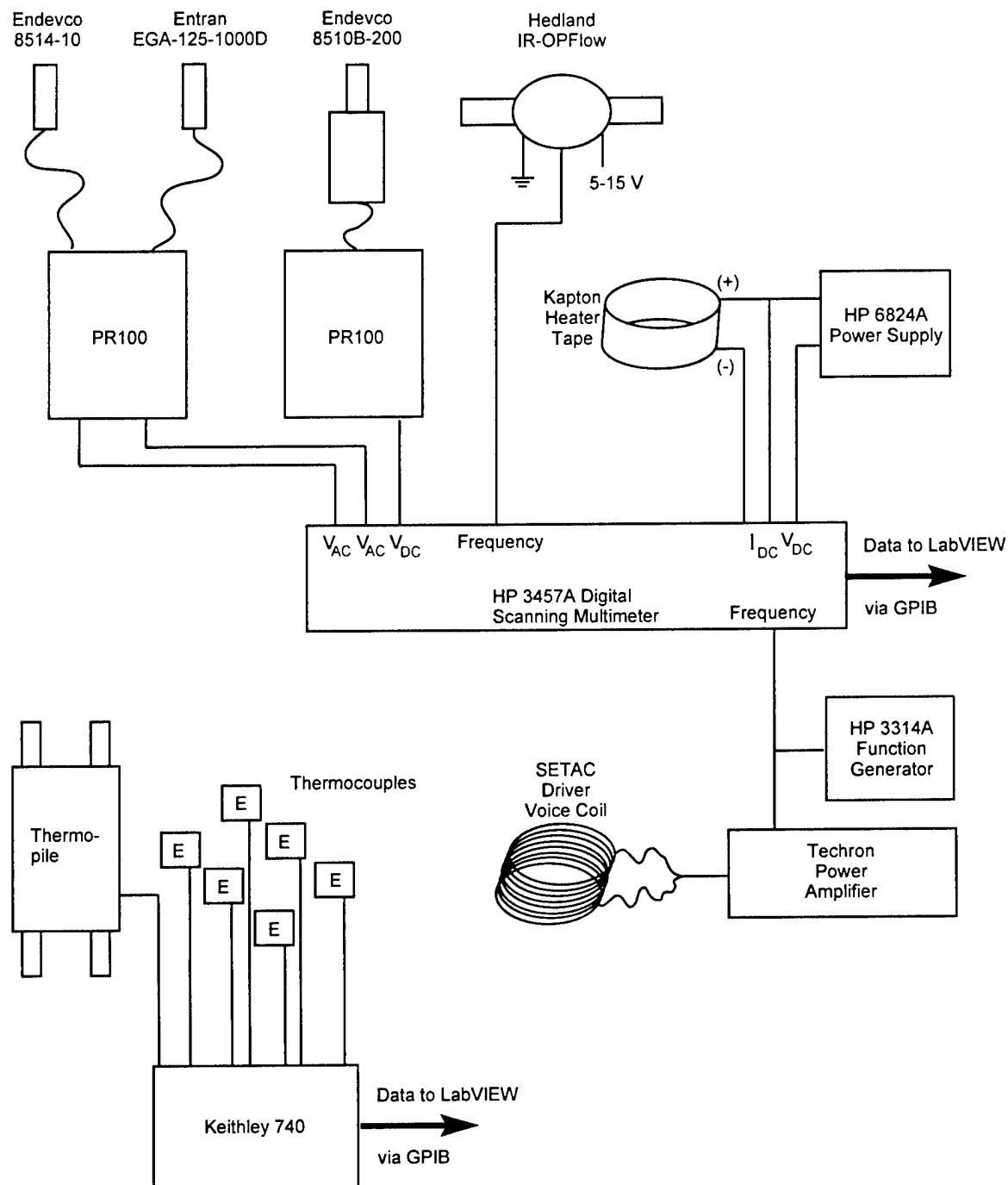


Figure 3.3: Signal Paths of Frankenfridge Sensors and Instrumentation

has not changed its output level ( $10.1 \text{ m/s}^2$  with respect to the NIST calibrated B & K accelerometer).

The AC response of the Endevco 8514-10 microphone mounted in the driver was calibrated on January 20, 1997 before measurements began. It was calibrated by comparison using two General Radio Type 1962-9611 capacitive pressure microphones as reference (SN: 11882 and SN: 11811). These two references (using the factory calibrations) yield two sensitivity values for the Endevco microphone that are within 9% of each other at 250 Hz. The sensitivity value that was used for these experiments is the sensitivity found by using the General Radio microphone (SN: 11882) as the transfer standard.

The Endevco 8510B-200 microphone mounted on the exhaust heat sink flange was calibrated at DC pressure using as a reference the Heise 200 psia Bourdon Tube (SN: CM-96728) gauge that is part of the gas fill manifold. This Heise absolute pressure gauge is set to zero psia using a good turbo vacuum pump. The relative error in the slope of the response curve of the Endevco 8510B-200 and the Heise gauge outputs is 0.029%. Subsequent DC calibration of the Heise with a Baratron MKS 390H absolute pressure standard (SN: 77730-1) showed the Heise to be reading about a half of a psia too high. The Heise offset was corrected to agree with the Baratron on March 20, 1997. However, the relative error in the slope of this DC level calibration of the Heise to the Baratron is still quite small at 0.016%. This is important because the AC sensitivities of the two Endevco pressure sensors are ultimately tied to the slope of the DC response of the Heise gauge.

During Run #1 (see Table 4.1), the AC response of the Endevco 8510B-200 was compared to the AC response of the Endevco 8514-10. Using the Endevco 8510B-200 as a reference, the microphone in the driver housing (Endevco 8514-10) showed a 5% lower sensitivity than was measured with the General Radio microphones. The relative error in the slope of a response curve of the two microphone outputs is 0.15% over a range of 6 kPa to 45 kPa.

The AC response of the two Endevco sensors were compared to each other on March 14, 1998 and are now found to be within 0.5% of each other as opposed to the 5% agreement found on February 10, 1997. On March 17, 1998 the AC response of the Endevco 8510B-200 was checked against the Heise gauge and the Endevco 8510B-200 AC sensitivity is found to have shifted by only 0.37%. Assuming that the Heise Bourdon Tube gauge has not

experienced a change in its mechanical sensitivity, the sensitivity of the Endevco 8514-10 seems to have shifted by 5% since the flange mounted sensor has been measured to be quite stable. There has been a shift of about 1 psi in the DC response of the Endevco 8510B-200 compared to the Heise in the past year.

The measured sensitivity of the Hedland flow meter has varied quite a bit which makes this the least reliable sensor in the Frankenfridge apparatus. The sensitivity is measured using an HP 5316A Universal Counter, a beam balance and a stop watch. The beam balance is calibrated using NIST calibrated standard masses and compared against a Mettler AE200 Analytical Balance. Some amount of water is pumped into a clean beaker for a measured amount of time. The mass of this amount of water is measured and the quotient gives the mass flow rate. The sensitivity of the flow meter has been measured in this way to be between  $1.236 \times 10^5$  pulses/gal and  $1.548 \times 10^5$  pulses/gal. This range is approximately  $\pm 10\%$  of the manufacturer's published sensitivity of  $1.363 \times 10^5$  pulses/gal. In each of the five calibrations, the response of this sensor was very nicely linear. A sensitivity of  $0.6657 \frac{\text{Hz}}{\text{g/min}}$  was used which corresponds to  $1.5090 \times 10^5$  pulses/gal. (The offset used was  $-133.52$  Hz.) This sensitivity resulted from one of three separate calibrations performed on 1 October 1997 over the range 350 g/min to 800 g/min. All three results were similar and between 7% and 14% of the nominal value quoted by the manufacturer.

The calibration of these sensors is very critical to the power measurements made on Frankenfridge. The input acoustic power measurement hangs on the accelerometer (which tells us the acoustic velocity), the bellows effective area and the driver housing microphone (which measures acoustic pressure). The product of the RMS magnitudes of acoustic volume velocity and the acoustic pressure at resonance determines the acoustic input power. The product of the temperature change that the thermopile measures and the flow rate from the flow meter determines the exhaust power.

### 3.2. Details of the Exhaust Heat Sink Flange and Flow Loop

The motivation for constructing and instrumenting a exhaust heat sink for the Frankenfridge apparatus is to be free from the cumbersome vacuum insulation used in the STAR apparatus. Knowledge of the cooling power of a refrigerator is obviously critical to measuring the performance of one. With imperfect insulation around the part of the device that gets cold, it is not certain that the heat flux introduced by the heater is the only heat that gets pumped; some heat from the room most certainly diffuses through the insulation to the cold side of the device and is seen as a heat load to the device. To get around this problem there are two solutions. One is to infer the amount of heat transferred from the room to the cold side from the First Law of Thermodynamics (Eq. (2.2)): if the exhaust heat flux of a refrigerator and the input power to the engine are both known, then the amount of heat flux that the device moves is the difference of the exhaust heat flux and the input acoustic power. The other solution is to directly measure the heat flow from the cold side of the refrigerator to the room. This direct measurement is a hard one to make because of the difficulty in measuring the convective heat transport; therefore, measuring the exhaust heat flux seems preferable.

To make the exhaust heat measurement, a copper flange was built that mates to the existing copper flange that is part of the STAR refrigerator hot heat exchanger assembly. Around this flange was soldered two loops of 1/8 in. copper refrigeration tubing through which water is circulated at a steady rate. It is hypothesized that the heat generated at the hot side from the thermoacoustic cycle (both the heat removed from the cold side plus waste heat) will raise the temperature of the water as it travels around the flange in the tubing. The following relationship:

$$\frac{d}{dt} [Q_H] = \frac{d}{dt} [mc_p \Delta T] \quad (3.1)$$

relates the rate at which exhaust heat is generated to a temperature change ( $\Delta T$ ) of the water for some mass of water ( $m$ ). This equation leads us to the exhaust heat flux, or exhaust power at steady state. The specific heat of water is tabulated to be  $4.181 \frac{\text{J}}{\text{g}\cdot\text{K}}$  at 295K and the other two quantities are measured directly — mass flow rate is measured with the flow meter and the temperature difference of intake and discharge water is measured with the thermopile. A small variable speed pump (Micropump Integral Series, Model

EG152-0024) is used to circulate the water and there is a small filter in the line to protect the pump and especially the flow meter.

The water must also be cooled somewhere in the loop if a temperature difference is going to be maintained across the flange inlet and discharge. This is accomplished with a large (50 gallons) bucket of water. The reason for this extravagance is that a very stable “heat dissipator” with a large heat capacity is required. At first, a small forced-air radiator was used as a dissipator but it is found that small hot and cold “pockets” of air moving through the radiator change its efficiency enough that a steady state condition is hard to maintain. It is not immediately apparent, but the dissipator must remove heat at a fairly constant rate if the temperature difference seen by the thermopile can be attributed only to heat conduction in the copper flange. The radiator failed this requirement but the large bucket of water seems to fit the bill because of its large heat capacity which translates into very slow changes in heat exchange rate.

Fig. 3.4 should be of some help in understanding this measurement of exhaust heat flux. The heat flow rate,  $\dot{Q}_H$ , is the exhaust heat flux of the thermoacoustic engine and  $\dot{Q}_d$  is the heat leak from the copper flange to the driver housing. The thermal resistance,  $R_d$ , across the Delrin™ ring that insulates the flange from the driver is measured to be 1.0 K/W and calculated to be 1.4 K/W using thermophysical parameters of the similar material, Teflon™. This means that the heat flux that is measured with the thermopile/flow-meter combination is the exhaust heat flux less the amount that escapes to the driver housing. The dissipator is expected to dissipate this same amount of heat from the water loop that is introduced at the exhaust heat sink flange. In an effort to minimize the amount of heat leak from the flange to the driver, the flow loop is diverted to loop twice around the driver housing after the discharge from the heat sink flange. This helps keep the driver housing and the flange at the same temperature which reduces  $\dot{Q}_d$  and also prevents the driver from overheating. No heat flux measurements are made across the driver cooling coil.

This measurement system is verified by running a closed water loop through two reservoirs of water. One reservoir is the 50 gallon bucket of water mentioned above. For proofing purposes, the closed flow loop is allowed to pass into thermal contact with another very small (1/4 gallon) reservoir of water that includes an electrical resistance heater. For testing purposes, the part of the loop that is immersed in this small reservoir is a coil of copper

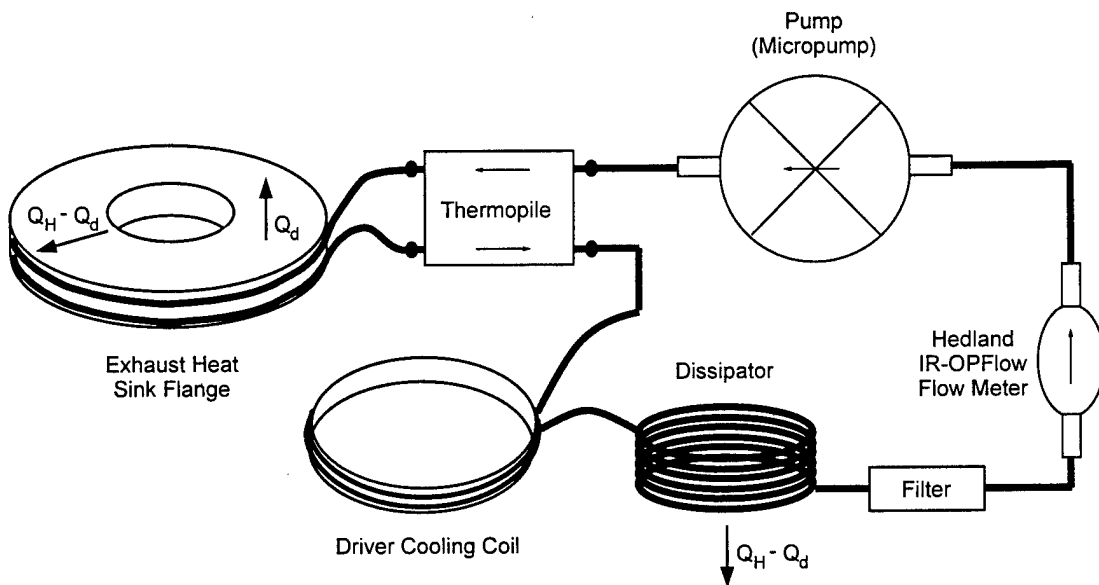


**Figure 3.4:** Schematic of the exhaust heat sink flange and heat flux measurement instrumentation. The small arrows show the water flow direction and the large arrows indicate heat flux.

tubing (but is analogous to the copper tubing soldered to the exhaust heat sink flange on Frankenfridge). The flow rate is monitored with the HP 3457A, and the thermopile voltage by the Keithley 740, and the data from these instruments recorded in LabVIEW<sup>TM</sup>. For a very long run of 9 hours (the system reached steady state in 15 minutes) where 5.35 W of electrical power is injected into the small reservoir, the instrumentation measures an average heat flux of 5.27 W. The variability in this measurement is critical because the experimenter does not want to wait nine hours for one data point; the standard deviation of the measurement of 5.27 W is 0.052 W and the standard deviation of the electrical input power measurement is 0.085 W! This small variability (0.052 W/5.27 W = 1.0%) is within an acceptable range.

### 3.3. The Data Recording System using LabVIEW

The software from National Instruments<sup>12</sup> called LabVIEW™ is used to record the signals read by the HP 3457A and Keithley 740. The LabVIEW™ software runs on a Pentium™ 100 personal computer with 32 MB of RAM running DOS with Windows 95. The communication between the two instruments and the computer is accomplished with GPIB (General Purpose Interface Bus) hardware. To add to the public good, two somewhat general programs are written by the experimenter in LabVIEW™ to communicate with the HP3457A and the Keithley 740 — programs that are not specific to the Frankenfridge application. It is hoped that these so-called “instrument drivers” will be at least useful to other experimenters in the local laboratory, if not users at different locations.

The program that is specific to the recording of Frankenfridge data requires a small amount attention here for the use of future experiments and experimenters. The programs “Frank Rev 2.2” and “Frank Rev 3.0” are well documented in the *Show VI Info* option under the *Windows* menu option. This information is reproduced here.

VI Name: Frank v3.0

This VI takes data from the Frankenfridge device. It assumes that the HP 3457A Scanning Voltmeter and Keithley 740 Thermocouple Scanner are used to read the sensor package on Frank in the following way.

HP 3457A Configuration

Channel Connection

0	Flange Mic (Endevco) AC Voltage
1	Driver Accelerometer (Driver) AC Voltage
2	Driver Mic (Endevco) AC Voltage
3	Flange Mic (Endevco) DC Voltage
4	No connection
5	Flow Meter (OPFLOW) Frequency (Hz)
6	Drive Frequency (Hz)
7	Heater load voltage (DC Voltage)
8	Heater load current (DC Current)
9	No connection

Keithley 740 Thermocouple Scanner Configuration

Channel Connection

2	Cold Side Temperature (Type E)
3	Hot Side Temperature (Type E)
4	Thermopile output temperature (Type E)

5	Thermopile intake temperature (Type E)
6	Thermopile response (mV)
7	Driver housing temperature (Type E)
8	Thermal Bath temperature (Type E)

This VI creates (or appends) to a data file with the prefix and location specified in frame 12. The fields that are written to this file are outlined below in the order that the columns appear when the ASCII file is viewed with a viewer (e.g. Notepad) or imported into a spreadsheet (e.g. Excel).

Field	Units
Drive Frequency	Hz
Stroke	mm
RMS Acoustic Pressure	Pa
Pressure Ratio	Percent
Acoustic Impedance	Ns/m <sup>5</sup>
Hot Side Temperature	deg C
Cold Side Temperature	deg C
Exhaust delta T	deg C
Flow Rate	g/min
Heat Load	W
Exhaust Power	W
Acoustic Power	W
Driver Housing Temp	deg C
Bath Temp	deg C
T-Pile Discharge	deg C
T-Pile Inlet	deg C
Time	
Date	

The LabVIEW™ programming environment has a very shallow learning curve and serves the purpose of recording the data of this experiment quite nicely.

## Chapter 4.

# Measurement Analysis and Results

---

---

This chapter analyzes the subsystems that play a large part in the performance measurements and then presents the measurement results. Because the space qualified STAR resonator has no penetrations for sensor leads and heat exchanger fluids, cooling power and the temperatures of the stack must be inferred from direct measurements that require no resonator penetration. The measurement of exhaust heat flux with the exhaust heat sink flange is used together with the First Law of Thermodynamics to infer the heat pumped from the refrigerator's cold side. A conduction model of the hot and cold heat exchangers is created to infer the stack temperatures from the temperatures measured outside of the resonator at the cold and hot side. First, this chapter will describe how these measurements and inferences are made. Secondly, the results of the measurements are described and compared to a (linear) DELTAE model. Finally, the Frankenfridge measurement results are compared to STAR performance.

### 4.1. Summary of Experiments

The performance of Frankenfridge was measured in eight controlled experiments. The first three runs were mainly diagnostic in nature to determine that the driver and all of the measurement systems functioned correctly and that the device behaved as expected at low amplitudes. Run #4, #5 and #6 produced the most fruitful data. Each was a helium/argon run and the fridge is operated in the same manner for each of these experiments. First, the fridge was turned on with no heat load and the cold side was stabilized at 17.2 °C by adjusting the acoustic pressure amplitude created by the driver. This temperature was chosen to be just a bit under room temperature to minimize the heat leak from the cold side to the room. The frequency of the driver piston oscillation was adjusted so that an in-phase relationship<sup>†</sup> between pressure and velocity at the face of the driver piston was maintained. Once the fridge reached a steady state at the pre-established cold side temperature, the

---

<sup>†</sup> The operator monitors a Lissajous pattern on an oscilloscope that is tracing the driver microphone and accelerometer signals.

electric heat load was activated to dissipate  $\frac{1}{2}$  W at the cold side. The acoustic pressure is again adjusted to keep the cold side at 17.2 °C. Once this new state is stable (taking about six to eight minutes) the heat load is again incremented by 1/2 W and the acoustic pressure is adjusted accordingly to maintain a constant cold resonator temperature. The operation is continued in this way up to 6.13% pressure ratio in Run #6. See Table 4.1 for a description of all of the experimental runs.

Because there is significant interest in the time-to-failure of the SETAC drivers, the total amount of time logged on the driver used in Frankenfridge during these experiments is 48.6 hours. No driver degradation was detected in the course of these experiments.

#### 4.2. Exhaust Heat Sink Flange

See the section in the Chapter 3 for a detailed discussion about the operation of the heat sink flange.

The analysis of the exhaust heat sink flange is a straightforward forced convection treatment.<sup>13</sup> A mass flow rate in the hot heat exchanger flange of 660 g/min is used throughout all of these experiments. The Reynolds number,  $Re_D$ , for this flow rate is calculated to be:

$$Re_D = \frac{4\dot{m}}{\pi\mu D} = 2576 \quad (4.1)$$

where  $\dot{m}$  is the mass flow rate,  $\mu$  is the dynamic viscosity of the fluid and  $D$  is the inner diameter of the 1/8 in. (O.D.) copper refrigeration tubing (the inner diameter is measured to be 0.0625 in.). This Reynolds number is just outside of the laminar flow regime. The laminar flow regime for flow in pipes is accepted to be  $0 \lesssim Re_D \lesssim 2300$  while fully developed turbulent flow is not found with Reynolds numbers less than 10,000.

The hydrodynamic entry length, that defines the length that it takes the velocity profile of the flow to become fully developed is,

$$x_{fd,h} \approx 0.05Re_D \times D = 205 \text{ mm} \quad (4.2)$$

Since the total length of 1/8 in. copper refrigeration tubing surrounding the flange is 820 mm, the flow has a fully developed velocity profile for about 75% of the tubing length.

The thermodynamic entry length, that defines the length that it takes the temperature profile of the flow to become fully developed is,

$$x_{fd,t} \approx 0.05Re_D Pr \times D = 1190 \text{ mm} \quad (4.3)$$

**Table 4.1:** Summary of measurements made with Frankenfridge.

<i>Run</i>	<i>Date</i>	<i>Conditions and Comments</i>
1	10 Feb. 1997	Mainly a diagnostic check of instrumentation and proof of concept, includes run at lab inaugural. Gas mix is 136 psia, 85.5% He, 14.5% Ar. Cold side is not insulated, exhaust loop instrumentation is not operational. Data recorded and analyzed manually. Run time: 220 min
2	13 Nov. 1997	Gas mix: 150 psia, 85.5% He, 14.5% Ar. Flow loop instrumentation operational, check first law balance. Cold side insulated, record thermal decay after shut-off for insulation effectiveness. Fix instrumentation snags. Data recorded manually. Pressure ratio does not exceed 3%. Diagnostic run. Run time: 240 min
3	20 Nov. 1997	Gas mix: 157 psia, 85.5% He, 14.5% Ar. Use LabVIEW™ data recording system. First Law agreement is good at high exhaust power, bad at low. Pressure ratio does not exceed 3.5%. Last diagnostic run. Run time: 280 min
4	21 Nov. 1997	Gas mix: 151 psia, 85.5% He, 14.5% Ar. Step through heat loads from 0 to 15 W, pressure ratio up to 3.3%. Good data set. Run time: 360 min
5	8 Dec. 1997	Gas mix: 151 psia, 85.5% He, 14.5% Ar. Check LabVIEW™ modifications and measure bath temperature in attempt to correct low power First Law imbalance. Learned that imbalance is not strongly correlated to bath temperature. Completely a duplicate of Run #4. Run time: 120 min
6	9 Jan. 1998	Gas mix: 155 psia, 85.5% He, 14.5% Ar. Step through heat loads from 0 to 26.5 W, pressure ratio up to 6.2%. Measure driver housing temperature for First Law correction. Good data set. Run time: 660 min
7	27 Feb. 1998	Gas mix: 156 psia, 85.5% He, 14.5% Ar. This run at 2% pressure ratio is made to compare Frankenfridge performance to STAR performance. Run time: 375 min
8	3 Mar. 1998	Gas mix: 155 psia, 85.5% He, 14.5% Ar. This run at 3% pressure ratio is made to compare Frankenfridge performance to STAR performance. Run time: 780 min

which means that the temperature profile of the flow is never fully developed in the length of copper tubing that undergoes heat transfer from the flange. In this expression,  $Pr$  is the Prandtl number, which is the ratio of the momentum and thermal diffusivities; for water at 300 K the Prandtl number has value of 5.83.

Since  $\bar{h}$ , the average convective heat transport coefficient is:

$$\bar{h} = \frac{\overline{Nu}_D K}{D} \quad (4.4)$$

a value for  $\overline{Nu}_D$ , the average Nusselt number in internal flow, must be calculated. Two correlations<sup>13</sup> for the Nusselt number of flow in the entrance (not fully developed) region, the Hausen correlation and the Sieder & Tate correlation. The Sieder & Tate correlation is:

$$\overline{Nu}_D = 1.86 \left( \frac{Re_D Pr}{(L/D)} \right)^{\frac{1}{3}} \left( \frac{\mu}{\mu_s} \right)^{0.14} \quad (4.5)$$

where  $L$  is the length of the copper tube,  $\mu$  is the free stream dynamic viscosity and  $\mu_s$  is the dynamic viscosity at the pipe surface. The ratio of these viscosities is taken to be unity. This correlation gives a value for the average Nusselt number of 17.5 which leads to a value of 6760 W/m<sup>2</sup> · K for  $\bar{h}$ , the average convection coefficient.

The relationship for the total heat transport from the fluid to the pipe wall is:

$$\dot{Q} = \bar{h} A_s \Delta T_{lm} \quad (4.6)$$

where  $\Delta T_{lm}$  is the log mean temperature difference and is  $(\Delta T_o - \Delta T_i) / (\ln(\frac{\Delta T_o}{\Delta T_i}))$ . In this log mean temperature difference,  $\Delta T_o$  is the temperature difference of the free stream liquid and the pipe wall at the outlet of the pipe, and  $\Delta T_i$  is the same at the inlet of the pipe. Using the result of Eq. (4.5) the value for  $\bar{h} A_s$ , the equivalent thermal resistance, is calculated to be 34.0 W/K. This thermal resistance is measured experimentally to be 17.7 W/K. The measurement of log mean temperature difference was made with the thermopile, a thermocouple mounted on the inlet to the thermopile and a thermocouple mounted on the hot heat exchanger flange. The outputs from these sensors were read with the Keithley 740. The measured value is expected to be lower because the calculation assumed that the whole of the tube is in contact with the flange when in fact, only roughly half of the surface area of the tube is in thermal contact.

As described in the instrumentation chapter, the measurement system has an absolute accuracy of 65 mW when a second reservoir is used to add heat in place of Frankenfridge. However, when the system is used to monitor the exhaust heat flux of Frankenfridge, a 2 W offset is measured when the refrigerator (*i.e.*, the driver) is not even powered. This offset is measured because there is a significant temperature difference between the copper heat

sink flange and the water in the large thermal bath. Since the water is one to three degrees Kelvin cooler than the flange, it extracts heat from the flange that does not represent exhaust heat from the fridge. This offset was not observed in the verification test because two water baths are used that are initially at the same temperature.

**Table 4.2:** Subset of data from Run #6 that exhibited a large First Law imbalance

Time	Acoustic Pressure (Pa <sub>rms</sub> )	Hot Side Ext. Temp (°C)	Cold Side Ext. Temp (°C)	Exhaust Temp Rise (°C)	Heat Load (W)	Exhaust Heat Flux (W)	Acoustic Input Power (W)	Total Input Power (W)	First Law Deficit (W)
11:55	0.0	21.9	22.5	0.043	0.00	2.00	0.00	0.00	2.00
12:46	3182.1	21.9	17.2	0.053	0.00	2.46	0.29	0.29	2.18
13:03	4561.7	22.0	17.3	0.066	0.49	3.03	0.54	1.03	2.00
13:12	5931.7	22.1	17.3	0.083	0.99	3.86	0.92	1.90	1.96
13:25	6941.7	22.2	17.3	0.101	1.48	4.68	1.25	2.74	1.94
13:41	7873.9	22.3	17.3	0.119	2.00	5.49	1.60	3.60	1.89
14:00	8810.3	22.5	17.2	0.134	2.50	6.22	2.00	4.50	1.72
14:22	9624.0	22.6	17.3	0.161	3.00	7.50	2.38	5.38	2.11
14:29	10412.0	22.7	17.2	0.177	3.50	8.12	2.78	6.28	1.84
14:44	11084.0	22.8	17.2	0.192	4.01	8.87	3.15	7.15	1.72
14:54	11814.0	22.9	17.2	0.212	4.50	9.83	3.57	8.07	1.76
15:07	12668.0	23.1	17.2	0.237	5.10	11.01	4.10	9.20	1.81
15:16	13402.0	23.2	17.2	0.257	5.61	11.98	4.58	10.19	1.79
15:22	13974.0	23.3	17.2	0.275	6.12	12.74	4.97	11.09	1.65
15:38	14571.0	23.4	17.3	0.293	6.62	13.66	5.40	12.02	1.64

Some typical data, just after startup, is displayed in Table 4.2. This data came from Run #6, which is typical of the measurements made for this thesis. In Run #6, the cold side of the fridge is well insulated and the cold side exterior temperature (“Cold Side Ext. Temp”) is intentionally held fixed at 17.2 °C. With no (or very little) heat leak to the room (the room is usually about 3 °C colder than the hot side), all of the heat produced by the resistance heater (“Heat Load”) is thermoacoustically pumped to the exhaust flow loop and measured (“Exhaust Heat Flux”). The column marked “First Law Deficit” is the difference

between the total input power and the exhaust heat flux measured in the flow loop. With this well insulated, “no heat leak” assumption, the First Law restricts this deficit to be zero.

A correction must be applied to the measurement of exhaust heat flux that accounts for the heat flux associated with the temperature imbalance of the flange and the cooling water. The simplest correction is to simply subtract the value of exhaust heat flux measured when the driver is not powered. This initial exhaust heat flux should be zero if the fridge has been idle for a long period of time (a day) as it was in Run #6. Furthermore, there is almost an hour between turn-on and the first (zero heat load) data point—this time lets the fridge settle into steady state at a cold side temperature of 17.2 °C. Subtraction of this offset from the data results in a much better First Law agreement as shown below in Table 4.3.

**Table 4.3:** Subset of data from Run #6 that have been corrected for the First Law imbalance. These are the same data as shown above in Table 4.2

Time	Total Input Power (W)	Measured Exhaust Power (W)	Corrected Exhaust Power (W)	Corrected Deficit (W)	Relative Deficit (%)
11:55	0.00	2.00			
12:46	0.29	2.46	0.46	0.18	61.65
13:03	1.03	3.03	1.03	0.00	-0.39
13:12	1.90	3.86	1.86	-0.04	-2.34
13:25	2.74	4.68	2.68	-0.06	-2.19
13:41	3.60	5.49	3.49	-0.11	-3.04
14:00	4.50	6.22	4.22	-0.28	-6.26
14:22	5.38	7.50	5.50	0.11	2.09
14:29	6.28	8.12	6.12	-0.16	-2.62
14:44	7.15	8.87	6.87	-0.28	-3.89
14:54	8.07	9.83	7.83	-0.24	-3.00
15:07	9.20	11.01	9.01	-0.19	-2.09
15:16	10.19	11.98	9.98	-0.21	-2.09
15:22	11.09	12.74	10.74	-0.35	-3.18
15:38	12.02	13.66	11.66	-0.36	-2.99

The fact that the corrected deficit grows with increasing exhaust power is suggestive of a heat leak (this trend would be more apparent if a whole data set were presented here). The first place to look for such a leak is across the heat sink flange/driver interface. There is a 0.119 in. thick Delrin<sup>TM</sup> ring that insulates the large aluminum driver housing from the resonator, however, it is certain that the thermal resistance of this ring is not very large. The ring has a 2.00 in. outer radius and a 1.198 in. inner radius with a bolt circle in between that matches the driver and the flange. The ring could be made thicker to improve its insulative properties but the corresponding increase in distance between the stack and the driver is not desirable.

The thermal resistance of the Delrin<sup>TM</sup> ring is calculated using a standard conduction analysis that ignores contact resistances. The calculated value (using a contact area of  $6.97 \times 10^{-3} \text{ m}^2$ , a conduction length of 3.2 mm and the thermal conductivity of Teflon<sup>TM</sup>, which is much like Delrin<sup>TM</sup>, as 0.35 W/m · K) for the thermal resistance offered by the insulating ring is 1.3 K/W. The thermal resistance offered by the ring is about 300 times better than would exist with no ring. By no means is the ring a perfect insulator, rather, at steady state it will provide enough of a thermal bottleneck to allow a measurable amount of exhaust heat to gather on heat sink flange and be removed by the circulating water. The heat flux across the ring between the heat sink and the driver housing is accounted for in post-processing of the data or on the fly in the LabVIEW<sup>TM</sup> system by measuring the driver housing temperature as well as the hot side flange temperature.

The thermal resistance offered by the insulating ring was measured by monitoring an E-type thermocouple mounted on the face of the driver housing that contacts the ring and monitoring the hot side flange temperature. A resistance heater was wrapped around the driver housing and heated to several elevated temperatures to let the housing absorb heat to a steady state. After recording several such points, the value of the thermal resistance of the insulating ring is found to be 1.0 K/W. This is in acceptable agreement with the simple conduction calculation (1.3 K/W) because an accurate value of the thermal conductivity of Delrin<sup>TM</sup> is not known and because the convection mode of heat transfer is not accounted for in the simple calculation, nor are two-dimensional effects.

If the measured value of the thermal resistance of the Delrin™ washer is used to apply a further correction to the exhaust heat flux measurement, the overall agreement gets a bit better.

**Table 4.4:** Subset of data from Run #6 that have been corrected for driver housing heat leak. These are the same data as shown above in Table 4.2

Time	Total Input Power (W)	Ring Temp Drop (°C)	Driver Heat Leak (W)	Exhaust Power (W)	Exhaust Plus Heat Leaked (W)	New Deficit (W)	Relative Deficit (%)
11:55	0.00	0.1	0.1				
12:46	0.29	0.1	0.1	0.46	0.58	0.29	100.64
13:03	1.03	0.1	0.1	1.03	1.14	0.11	10.34
13:12	1.90	0.0	0.0	1.86	1.86	-0.04	-2.34
13:25	2.74	0.0	0.0	2.68	2.68	-0.06	-2.19
13:41	3.60	0.0	0.0	3.49	3.49	-0.11	-3.04
14:00	4.50	0.0	0.0	4.22	4.22	-0.28	-6.26
14:22	5.38	0.1	0.1	5.50	5.61	0.22	4.15
14:29	6.28	0.1	0.1	6.12	6.23	-0.05	-0.86
14:44	7.15	0.1	0.1	6.87	6.99	-0.17	-2.34
14:54	8.07	0.1	0.1	7.83	7.94	-0.13	-1.62
15:07	9.20	0.1	0.1	9.01	9.06	-0.14	-1.49
15:16	10.19	0.1	0.1	9.98	10.03	-0.16	-1.55
15:22	11.09	0.0	0.0	10.74	10.74	-0.35	-3.18
15:38	12.02	0.1	0.1	11.66	11.72	-0.30	-2.53

The heat leak to the driver is minimized with the help of the driver cooling coil. This heat exchanger consists of two loops of 1/4 in. copper refrigeration tubing soldered to a piece of copper shim stock formed into a ring. A hose clamp secures the ring snugly to the perimeter of the aluminum driver housing. The water that is first circulated around the exhaust heat sink flange enters the driver cooling coils and absorbs the heat produced by the driver before being circulated through the large thermal bath. The driver cooling coil serves dual purposes: one of which is to help dissipate the Joule heating in the voice coil that threatens to destroy the voice coil windings at high drive currents. The second

function of the driver cooling coil is to maintain the driver housing at a temperature much closer to the temperature of the exhaust heat sink flange, thus minimizing the heat leaked to the driver housing from the hot heat sink flange. At the highest power operating points, the temperature difference between the driver housing and the heat sink flange (and thus across the Delrin™ insulating washer) is only a few degrees Celsius.

The average First Law energy deficit in a range from 0 to 80 W is 450 mW with a standard deviation of 582 mW. The average relative error (comparing the deficit to the total input power) is 1.9% in the same range.

It is still bothersome that there is some heat leak from the exhaust heat sink flange to the room. If the flow loop is monitored for a long time (with no acoustic excitation), nearly four hours in one measurement, the measured exhaust heat flux never gets below 1.5 W.

### 4.3. Heat Exchanger Performance Model

In order to compare experimental data to the DELTAE model, knowledge of the stack end temperatures (hot and cold side) is necessary. Space qualification of the resonator in its past life required that no penetrations were made in the resonator for signal leads. A simple mathematical calculation for the parallel thermal resistance of the fins of the heat exchanger allows the temperature of the central fin region of the heat exchanger to be calculated.

The heat exchangers in Frankenfridge are composed of 50 copper fins (0.254 mm thick) separated by 0.51 mm. The hot side and cold side temperatures are monitored outside of the resonator. The hot side thermocouple is located on the copper flange where the hot heat exchanger is seated and the cold side thermocouple is located just below the cold side heat exchanger. Between an end of the stack and the corresponding heat exchanger (either hot or cold) there are at least two paths for heat flow. Conduction from the gas oscillating near the end of the stack to the fins of the heat exchanger and convection between the same are two of these paths. The alternating flow convective heat exchange is not well characterized theoretically. If the heat exchangers are designed properly, the thermal resistance of this mode is small enough that there is only a small temperature drop associated with the convection resistance (in DELTAE this drop is only a Kelvin or two at most). The conduction resistance through the gas is so large that very little heat is transferred in this manner from the gas to the fins and can be ignored.

However, since the thermocouples are mounted outside the resonator and not right on the fins, a method to infer the temperature of the fins (and hence the stack temperature) is needed. The addition of a fin to a surface is usually motivated by the increase in surface area that enhances the convection heat transfer. However, this addition of surface area (and hence material) also carries with it some thermal resistance that depends not only on the amount, but the type of material that makes up the fin. Since the potential for heat transfer to or from a surface depends on the temperature of the surface and the temperature of the surrounding medium, the best performance from a fin would be realized if that fin were at the same temperature across the whole length of the fin. However, because a fin has non-zero thermal conduction resistance, the fin sustains a temperature gradient and performs below this optimum. The fin efficiency is a multiplicative constant<sup>13</sup> that expresses the degradation of heat transfer due to the addition of the conduction resistance by the fin and is defined as:

$$\eta_f \equiv \frac{q_f}{q_{max}} = \frac{q_f}{hA_f(T_b - T_\infty)} \quad (4.7)$$

where  $q_f$  is the actual heat transferred by the fin,  $q_{max}$  is the optimum,  $h$  is the convective heat transfer coefficient,  $A_f$  is the surface area of the fin,  $T_b$  is the temperature at the base of the fin and  $T_\infty$  is the temperature of the medium surrounding the fin. If we assume the end of the fin is insulated from the medium,  $q_f$  is:

$$q_f = \sqrt{hPKA_c}(T_b - T_\infty) \tanh(mL) \quad (4.8)$$

where  $P$  is the perimeter of the fin,  $K$  is the thermal conductivity of the fin material and the critical length  $m$  is defined by  $m^2 = \frac{hP}{KA_c}$ . With a little manipulation, the fin efficiency (Eq. (4.7)) can be expressed as:

$$\eta_f = \frac{\tanh(mL)}{mL}. \quad (4.9)$$

All of the parameters that make up the critical length,  $m$ , are geometric or tabulated except for the convective heat transfer coefficient,  $h$ . This parameter is not well defined for oscillating flow convective heat transfer and several correlations are offered here as possibilities.

The fin efficiency, a value less than one, increases the value for the effective thermal resistance of the fin:

$$R_{fin} = \frac{1}{\langle h \rangle \eta A_f} \quad (4.10)$$

where  $A_f$  is the surface area of the fin.

In a paper<sup>14</sup> describing the heat exchangers for the TALSR/SETAC device, Garrett claims that a rough approximation to the convective heat transfer coefficient,  $h_{AC}$ , is:

$$h_{AC} = \frac{Q_{AC}}{A\Delta T} = \frac{k}{\delta_\kappa} \quad (4.11)$$

From the values of the thermophysical properties of the gas mixture shown in Table 1.1, the simplest model for the convective heat transport predicts  $h_{AC} = 1020 \text{ W/m}^2\text{K}$ . Since the flow is oscillating sinusoidally, a root-mean-square average makes sense, and the time averaged convective heat transport coefficient,  $\langle h_{AC} \rangle$  is  $720 \text{ W/m}^2\text{K}$ .

A better approximation to  $h_{AC}$  can be calculated if the flow is known to be turbulent or laminar. The Reynolds number<sup>15</sup> is a non-dimensional ratio that compares the inertial forces of the flow to the viscous forces imposed by a boundary on the flow. For an isolated flat plate, which like the fins in the heat exchangers except for the fact there is another flat plate above and below, the Reynolds number is:

$$Re_l = \frac{u_\infty \Delta x_{EX}}{\nu} \quad (4.12)$$

where  $\Delta x_{EX}$  is the fin length along the resonator axis and  $\nu$  is kinematic viscosity. The flow is turbulent if Reynolds number is large (inertia forces are much greater than viscous forces) and a low Reynolds number means that the viscous forces are able to restrain the inertia forces creating a laminar flow. For flow over a flat plate, a Reynolds number of 500,000 marks the transition from laminar to turbulent flow. At the hot heat exchanger in Frankenfridge, the time averaged sinusoidal free-stream velocity,  $\langle u_\infty \rangle$ , is 5.56 m/s for an acoustic pressure of 30 kPa (see Table 1.1 for gas mixture thermophysical properties). This leads to a Reynolds number of 6522 which is well below the laminar limit. Likewise, the fins of the cold side heat exchanger experience average velocity oscillations of 7.93 m/s (with pressure oscillations of 30 kPa) which leads to a Reynolds number of 3721. The Reynolds number corresponding to flow in the cold exchanger is a little greater than half the value at the hot exchanger because although the flow velocity is faster here, the fin length of the hot exchanger is twice the length of the cold exchanger (see Table 1.1).

The Nusselt number, which can be thought of as the ratio of total heat transfer to conduction heat transfer, is shown in Eq. (4.13) spatially averaged over a plate of length L:

$$\overline{Nu} \equiv \frac{\overline{h}L}{K} \quad (4.13)$$

where  $K$  is the thermal conductivity of the fluid. Scaling arguments<sup>15</sup> (similitude) guarantee that the average Nusselt number is correlated to the Reynolds number and the Prandtl number (a non-dimensional ratio of the viscous to thermal diffusivity). The standard correlation for laminar flow is:

$$\frac{\bar{h}L}{K} = \overline{Nu} = 0.664Re^{1/2}Pr^{1/3} \quad (4.14)$$

The above expression leads easily to the average convective heat transfer coefficient for a fin in the heat exchanger. The value that corresponds to flow through the hot side heat exchanger is  $\bar{h}_H = 700 \text{ W/m}^2\text{K}$ . Since the Nusselt number depends on the square root of the free-stream flow velocity (see Eq. (4.14)) and this velocity is oscillating sinusoidally, a time average value of the heat transfer coefficient makes sense. Because the heat transfer is independent of the sign of velocity, an average over half a period is required.<sup>14</sup>

$$\frac{\langle u_\infty^{1/2} \rangle}{u_\infty^{1/2}} = \frac{1}{\pi} \int_0^\pi (\sin x)^{1/2} dx = 0.763 \quad (4.15)$$

The time average heat transfer coefficient corresponding to the hot side and cold side flow is shown in Table 4.5. It is comforting to note that these numbers are not substantially different from the crude calculation shown at the beginning of this section in Eq. (4.11). With these values of  $\bar{h}$ , the characteristic length,  $m$ , can be calculated using values for the fin cross sectional area and cross sectional perimeter,  $A_c$  and  $P_c$ , respectively. The results are shown in Table 4.5.

Now that the heat transfer coefficient has been obtained, only the geometrical aspects of the exchanger remain to be calculated. Since each fin has different length, the thermal resistance including the fin efficiency is easily calculated for each fin with a FORTRAN program or spreadsheet. The symmetry of the cylindrical heat exchanger can be exploited so that the resistance of each fin in only one-quarter of the exchanger needs to be calculated on a fin-by-fin basis. Fig. 4.1 shows the geometry of both the hot and cold heat exchanger (the only difference between the two is that the hot exchanger has fins that are twice as long in the direction of acoustic flow). In both exchangers, the center-to-center fin spacing,  $b$  is 0.762 mm. The radius of the exchanger,  $R$  is 1.9 cm which gives a total number of fins,  $N = 2R/b = 50$ . By the Pythagorean Theorem, the length of fin  $n$  is

$$L_n = \sqrt{(R^2 - (nb)^2)} \quad (4.16)$$

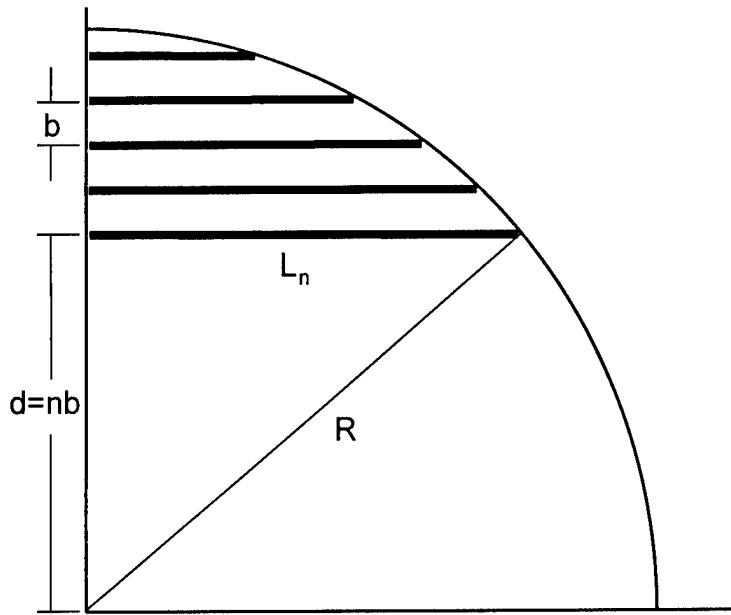


**Figure 4.1:** Geometry of the hot and cold heat exchanger, end view of a 1/4 slice.

The total surface area of each fin is twice the depth of the fin,  $2x_{EX}$  times the length of the fin. The surface area of the edges of the fin is neglected. The thermal resistance between the fins and the inside of the resonator body of the hot exchanger is calculated in a spreadsheet to be  $R_H = 0.172 \text{ K/W}$  and the cold exchanger  $R_C = 0.303 \text{ K/W}$ . Since the resonator body is thin copper, it is assumed that there is very little thermal resistance from the inside of the resonator body to the thermocouple.

**Table 4.5:** Heat exchanger model summary

Parameter	Hot Exchanger	Cold Exchanger
$A_c$	$1.62 \times 10^{-6} \text{ m}^2$	$6.45 \times 10^{-7} \text{ m}^2$
$P_c$	$1.32 \times 10^{-2} \text{ m}$	$5.59 \times 10^{-3} \text{ m}$
$\langle \bar{h} \rangle$	$530 \text{ W/m}^2\text{K}$	$1,000 \text{ W/m}^2\text{K}$
$m$	$104.2 \text{ m}^{-1}$	$147.4 \text{ m}^{-1}$
$R$	$0.172 \text{ K/W}$	$0.303 \text{ K/W}$

## 4.4. Performance of Frankenfridge

### 4.4.1. Performance at low amplitudes ( $P_A/p_m \leq 3\%$ )

Fig. 4.2 shows two graphs: the measured input acoustic power required to attain a certain pressure ratio inside the resonator and the cooling power for  $P_A/p_m \leq 3\%$ . In the presence of a stack and heat exchangers, this acoustic power is responsible for pumping heat from the side of the stack that gets cold to the side that gets hot.

The DELTAE model is generated by entering each experimental datum point into the model one at a time and letting the model generate a solution for each point. For the comparison in Fig. 4.2, the hot and cold side heat exchanger temperatures are targets for DELTAE and the program is allowed to solve for the input acoustic power and heat pumping power that correspond to the target temperatures. The pressure at the specific datum point is also given to DELTAE not as a Guess or Target, but just as an invariant input parameter. In the same way, the acoustic and heat pumping power is set to be an output parameter of DELTAE, not a Guess or Target. This allows DELTAE to very accurately model an experimental condition. The acoustic power required to attain a certain pressure ratio under the experimental condition is more than 30% greater than DELTAE predicts it to be. The graph of heat pumping power (or cooling power) shows excellent agreement with DELTAE at low amplitudes.

### 4.4.2. Performance at high amplitudes ( $P_A/p_m \leq 6\%$ )

The high amplitude data from Run #6, where operation up to a 6% pressure ratio was measured, is presented in Fig. 4.3.

It is reassuring that data from Run #6 below about 4% pressure ratio match data of Run #4 quite nicely. The offset between measured data and DELTAE in the acoustic power required to attain some pressure ratio that was evident in the Run #4 data still exists and is roughly the same—between 30 and 40 percent. The fact that the offset seems to be a very weak function of pressure amplitude suggests that Frankenfridge possesses some thermoviscous loss mechanism not modeled by DELTAE and that the bulk of the discrepancy between the DELTAE model and measurements is not due to nonlinear effects. This linear effect could be a dent in the bulb termination of Frankenfridge or some leak or undocumented cavity introduced between the driver, insulating ring, heat sink flange, and resonator interfaces. The

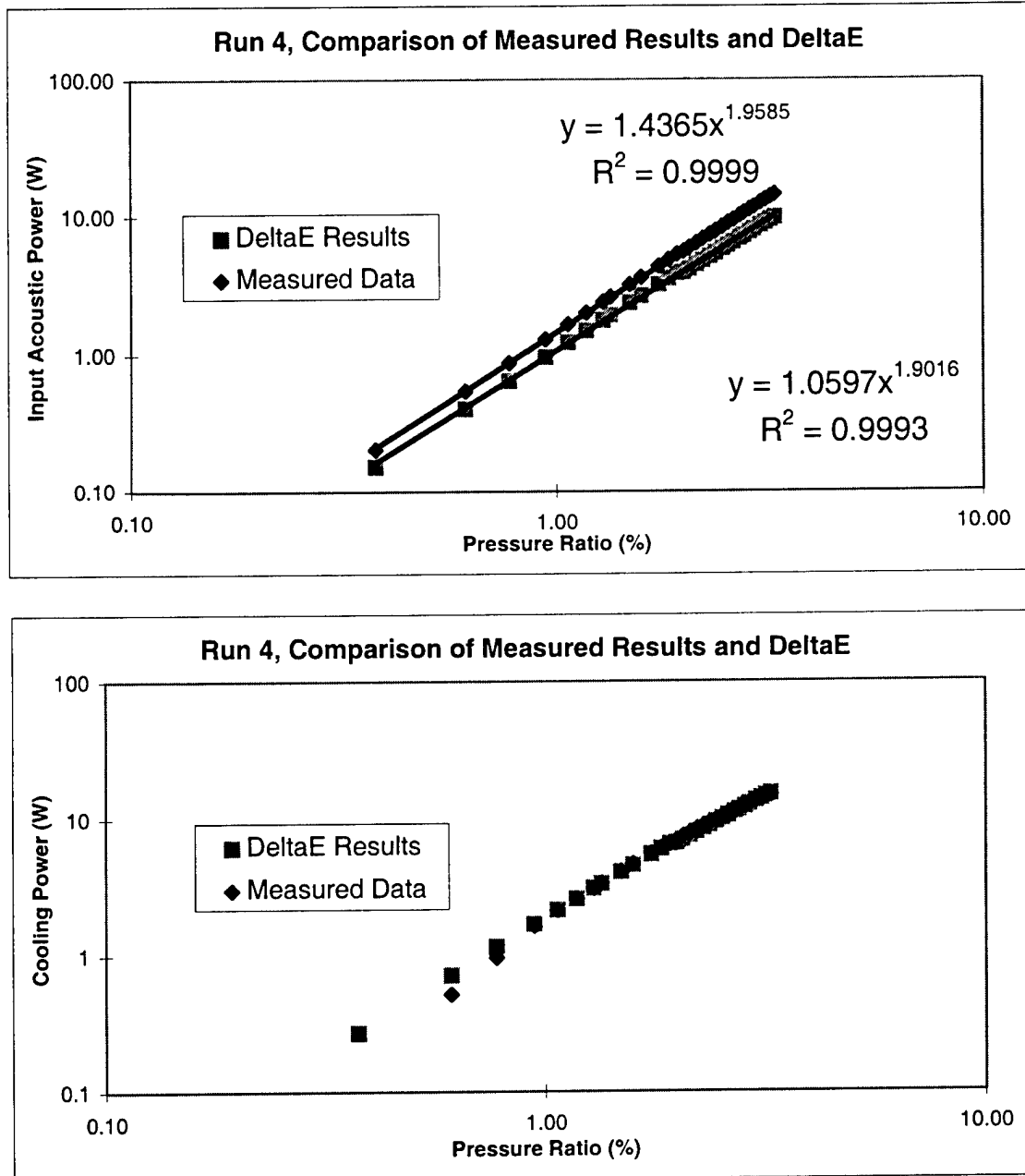


**Figure 4.2:** Comparison of measured data and DELTAE prediction for  $P_A/p_m \leq 3\%$ . The outside cold metal temperature is  $17.2^\circ\text{C}$ .

Run #6 data does show a nonlinear degradation in cooling power between the measured data and the (linear) DELTAE results above a 4% drive ratio. This nonlinear performance degradation is not so significant as to scare a designer of thermoacoustic engines away from

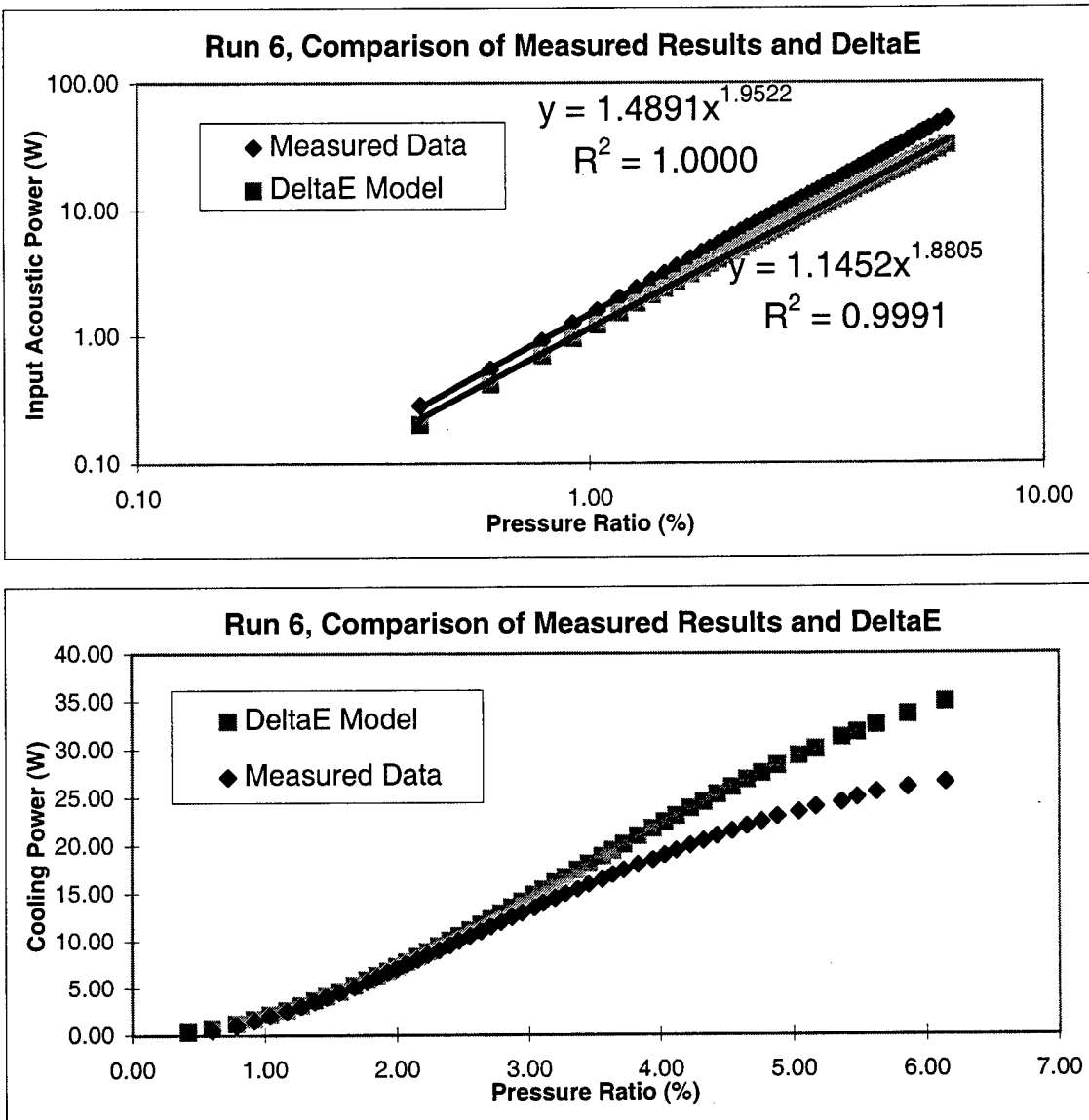


**Figure 4.3:** Comparison of measured data and DELTAE prediction for  $P_A/p_m \leq 6\%$ . The outside cold metal temperature is  $17.2^\circ\text{C}$ .

a device that operates above 4% — especially if she is willing to make the small sacrifice in *COP* for the substantial increase in power density.

#### 4.4.3. DELTAE Model Perturbations

Because this disagreement in acoustic input power between measured performance of Frankenfridge and the DELTAE is troubling, different physical effects are magnified with new DELTAE models to uncover clues about the discrepancy. A DELTAE model is created that includes turbulent flow, another that includes a larger surface area for added thermoviscous loss and another that uses a different stack geometry that may more closely represent the rolled Mylar<sup>TM</sup> and fishing line stack in Frankenfridge.

The thermoacoustic modeling software DELTAE has the capability to model turbulent acoustic flow; the parameter that DELTAE uses to determine the turbidity of the flow is the relative roughness. In a duct this is defined<sup>15</sup> as the ratio of the surface roughness,  $e$  to the diameter of the duct:  $rel\ roughness = e/D$ . A typical value<sup>15</sup> of surface roughness ( $e$ ) for drawn tubing is  $5 \times 10^{-6}$  in.

The result from the DELTAE model with turbulence that is shown in Fig. 4.4 corresponds to a relative roughness value of 0.1. This value is assigned to the cold reducer, cold duct and the trumpet but is outrageously large for hardware of the size and type in Frankenfridge. However, the lip of the trumpet could provide an obstacle to the flow on the order of 10% of the diameter of the cold duct. While it is not certain that this obstacle could be modeled as a pipe roughness, it is interesting to see what DELTAE predicts for such a value. At the least, it sheds some light on the very turbulent limit.

Because the amplitude independent discrepancy of DELTAE predictions and measured data suggests an inaccurately modeled thermoviscous loss, the surface area of the cold reducer, cold duct and trumpet is increased by 30% in DELTAE. This new model should have a lower value for  $Q$  and should lessen the difference in the original DELTAE model and measured data. It does make the discrepancy smaller, but only by a few percent.

Instead of using **STKS**lab which models a parallel plate stack in DELTAE, a **STKRECT** is substituted. It is possible that this stack segment will more closely model the Mylar<sup>TM</sup> film/fishing-string stack used in Frankenfridge. This modification only decreases the discrepancy by a few percent as well. The graphs shown in Fig. 4.4 illustrate these different models. These data are plotted on a logarithmic axes to highlight any linear deviations from the unaltered (“Straight”) DELTAE results. The fit corresponds to the particular model — please use the fit in Fig. 4.3 to compare the power law dependence of the different models.

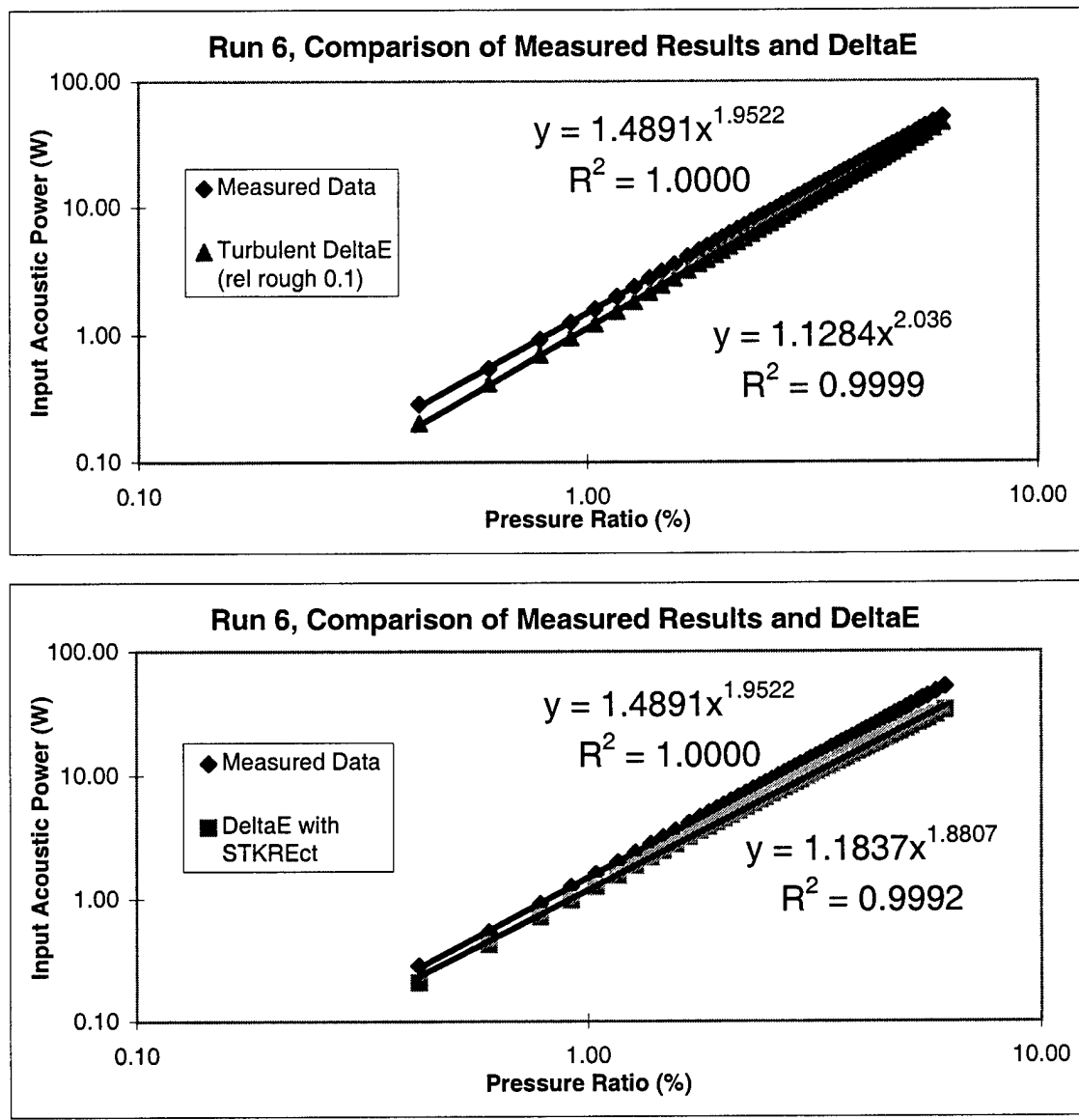


**Figure 4.4:** Acoustic power requirements for DELTAE models of Run #6 operating conditions.

The effect of these various model perturbations on cooling power is shown on the graph in Fig. 4.5. Included on this graph is the measured Run #6 cooling power.

Each one of the model perturbations exhibits the expected behavior—that is, the turbulent flow shows a nonlinear roll-off at about 4% pressure ratio (which agrees well with the measured data), the addition of thermoviscous damping degrades the cooling power

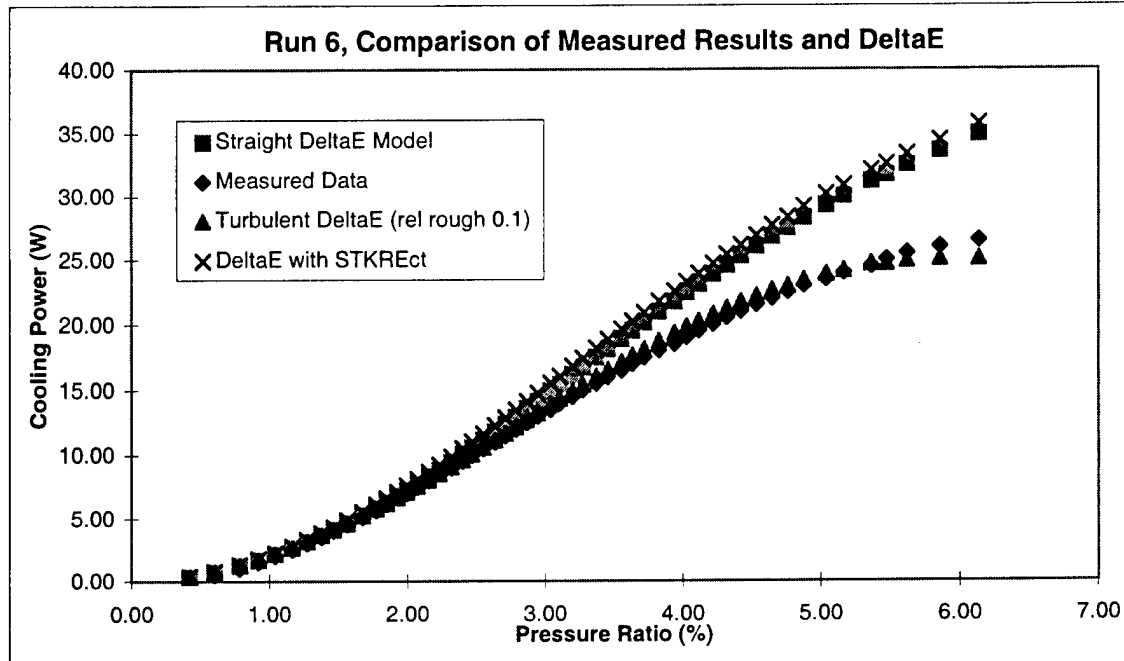


**Figure 4.5:** Cooling power of DELTAE models of Run #6 operating conditions.

independently of amplitude (not shown in Fig. 4.5). The change from STKSlab to STKREct shows a slight increase in cooling power for a given pressure ratio which makes sense since the fishing line now gets to participate in thermoacoustic heat transport.

In summary, none of these artificial perturbations to the DELTAE model correct the acoustic power discrepancy, nor do they destroy the excellent agreement of cooling power for a given pressure ratio below pressure ratios of 3%.

#### 4.4.4. Comparison of Frankenfridge Performance with STAR Performance

Data points were recorded on STAR with two gas mixtures, helium/argon and helium/xenon. Run #7 and Run #8, using a helium/argon mix, were made under similar conditions and in a similar manner as the STAR data were gathered. The plots in Figs. 4.6 and 4.7 compare the performance of STAR to the performance of Frankenfridge at 2% and 3% pressure ratios using coefficient of performance relative to Carnot ( $COPR = COP/COP_{Carnot}$ ) as a performance metric.

The operation of Run #7 and Run #8 was different than in the high power runs. The conditions of Run #7 and Run #8 spanned much larger temperature differences and saw a lower cooling power to simulate STAR experiments. The fridge was first turned on with no heat load and a large drive ratio ( $\approx 3\%$ ) and the cold side cooled to a low temperature ( $\approx -18^{\circ}\text{C}$ ). At this steady condition, a small heat load was applied ( $\approx 2 \text{ W}$ ) and the cold side temperature allowed to increase. As the cold side temperature increased, the heat load was reduced by about 20% to 30% to “catch” the cold side temperature and be at steady state. This procedure eliminates the long exponential approach to steady state (the experimenter is too impatient and likes to play with knobs and buttons). Since the cold side temperature is much colder than the room, the heat leak from the room to the cold side is quite significant. Where in the high power, low  $\Delta T$  runs, the exhaust heat sink flange measurement system was used mainly as a First Law energy check, it is now used to infer the cold side heat flux ( $\dot{Q}_C = \dot{Q}_{EX} - \dot{W}_{AC}$ ).

The performance of Frankenfridge at 2% and 3% show significant deviations from the DELTAE predictions. This is consistent with the discrepancies in the model and the data of Runs #4 and #6 shown in Figs. 4.2 and 4.3. Frankenfridge performance in Fig. 4.6 and 4.7 also show significant differences compared to the STAR data at 2% and 3%. This difference may be due to the fact that the stack position in the standing wave has changed with the addition of the exhaust heat sink flange and the Delrin<sup>TM</sup> insulating ring. The flange moves the stack 0.5 in. away from the driver while the insulating ring moves it another 0.12 in. The STAR driver had a much smaller bellows length than the SETAC driver used in Frankenfridge which accounts for the largest change in the stack position. This movement is significant because the classic trade-off between efficiency and heat pumping power in an engine depends on the product of wavenumber and stack position ( $kx$ ) in the

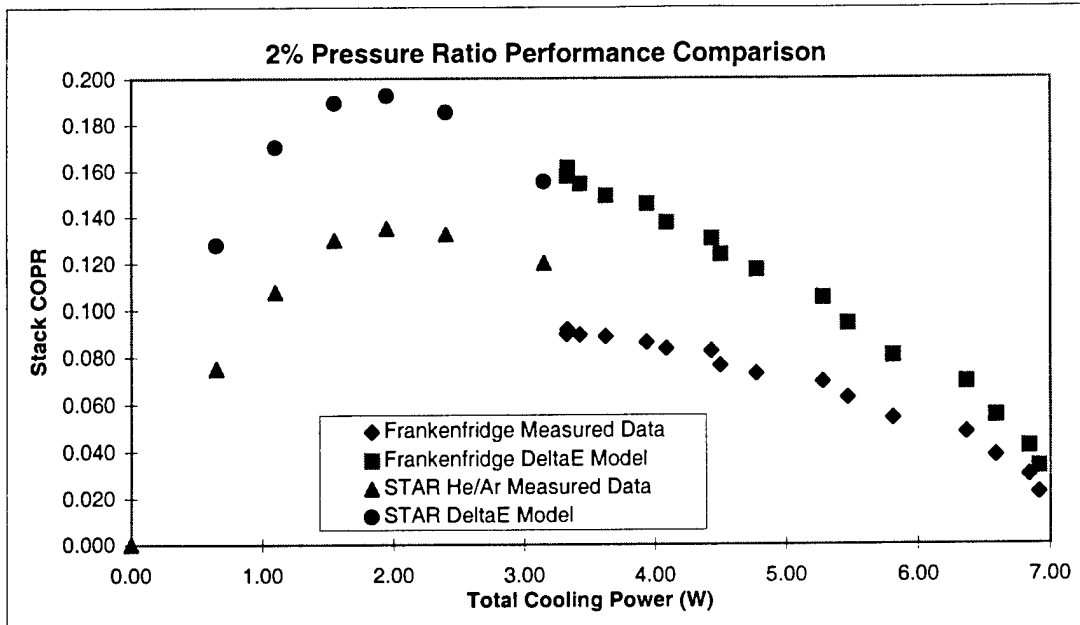


**Figure 4.6:** Comparison of  $COPR$  at 2% pressure ratio for Frankenfridge, STAR and DELTAE models. STAR data from Ref. 4

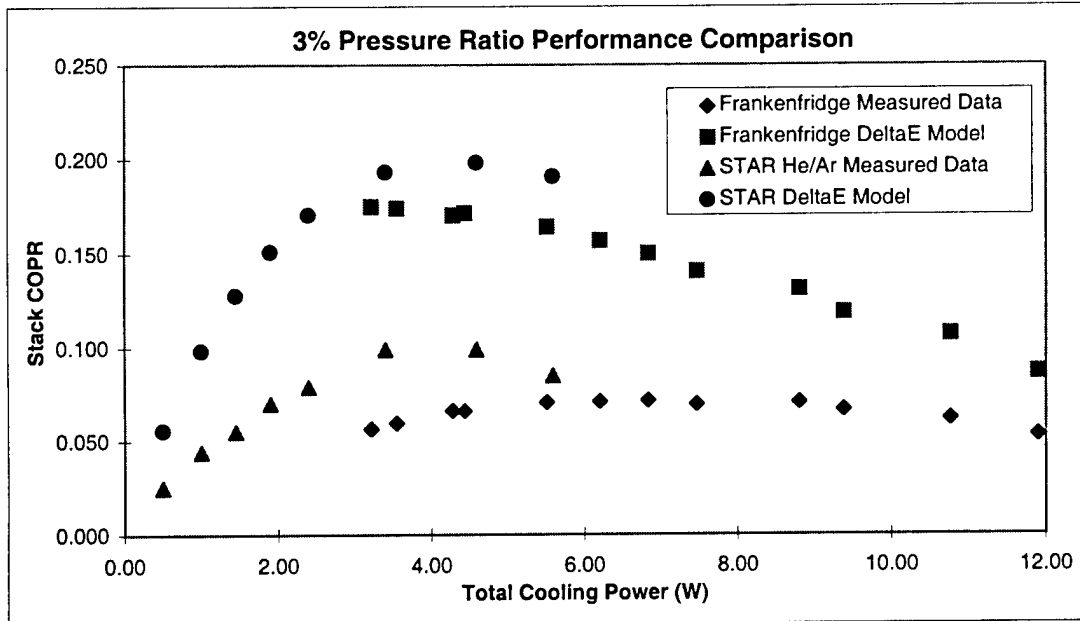


**Figure 4.7:** Comparison of  $COPR$  at 3% pressure ratio for Frankenfridge, STAR and DELTAE models. STAR data from Ref. 4

standing wave for a thermoacoustic refrigerator. The *COPR* is a monotonically decreasing function as  $kx$  moves away from the driven end of the resonator. See Appendix A for a short overview of the effect of  $kx$  on stack performance and the short stack approximation to the thermoacoustic heat transport equations. The value of  $kx$  for Frankenfridge is about 0.32 and the value for STAR is about 0.28, a significant difference of 14%. By examining the curves of STAR and Frankenfridge DELTAE model results, one can see that the STAR DELTAE model<sup>†</sup> predicts a larger value of maximum *COPR* than does the Frankenfridge model. (Although this appears not to be the case in Fig. 4.6, one only has to extrapolate the curve of the Frankenfridge model by eye to see that it will not peak as high as the STAR model.)

#### 4.4.5. Resonator Losses

Comparison of the quality factor of the resonator to the quality factor predicted by the DELTAE model should reflect the discrepancy in input acoustic power if this discrepancy is caused by inaccurate modeling of thermoviscous loss.

The quality factor of the resonator is measured by using the driver to introduce a small acoustic pressure from a constant voltage source (an HP 3562A Dynamic Signal Analyzer, 2-channel). The analyzer makes a sweep of frequency and records the driver microphone response divided by the driver accelerometer response (but first divides the acceleration by the angular frequency to obtain velocity). Using the pole and zero values that the analyzer calculates from a pole-zero curve fit of this impedance ( $p/v$ ) curve allows a determination of  $Q$ , or the quality factor of the resonance. Using this technique,  $Q$  is measured to be 11.0.

The Frankenfridge model in DELTAE can be programmed to produce a frequency sweep at a very low pressure amplitudes to allow a determination of the model resonator's  $Q$ . This sweep is executed at a constant volume velocity and at such very low pressure amplitudes that no heat is pumped and no temperature gradient evolves across the stack. A half power point fit for  $Q$  from this pressure response sweep yields a value of 11.75. Using the relationship of  $Q$  to the rate of change of phase angle with frequency ( $Q = \frac{\pi f_0}{360} \frac{d}{df} [\phi]$ ) gives a

---

<sup>†</sup> DELTAE did not exist at the time of STAR construction; the model has been constructed as part of this project. The only difference in the STAR model is that  $kx$  is smaller than it is the Frankenfridge model.

$Q$  of 11.6. The plot of the magnitude and phase of the DELTAE modeled pressure response appears below.

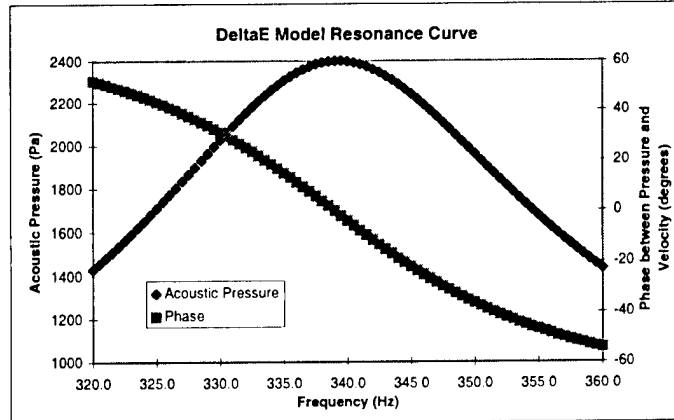


**Figure 4.8:** Acoustic pressure magnitude and phase of the Frankenfridge DELTAE model around the acoustic resonance.

With the stack removed from the resonator of Frankenfridge, the input power required to attain several pressure ratios was measured. The gas mixture used with no stack is 80.14% helium and 19.86% argon. The results of this experiment are shown in Fig. 4.9 and compared to two DELTAE models — one that uses **INSDUct** segments for heat exchangers (with an augmented perimeter to account for thermoviscous loss on the fins) and one with **HX\*\*\*\*** (a finned heat exchanger) segments. The result of both computer models is the value of acoustic power imparted to the resonator and the input to the model is the same values for acoustic pressure that were used to experimentally determine the acoustic power imparted into the physical resonator. The discrepancy seen in Fig. 4.9 between the measured data and the DELTAE results suggest that there is some part of the resonator that is not understood, or not modeled in DELTAE correctly.

The quality factor of the physical stackless resonator was measured to be 56. The models predict that  $Q$  to be 66 for the model that has heat exchangers and 83 for the model with enhanced **INSDUcts** in place of the heat exchangers.

The fact that  $Q$  is larger for the duct model compared to the model with real heat exchangers is consistent with our understanding of heat exchanger performance because the

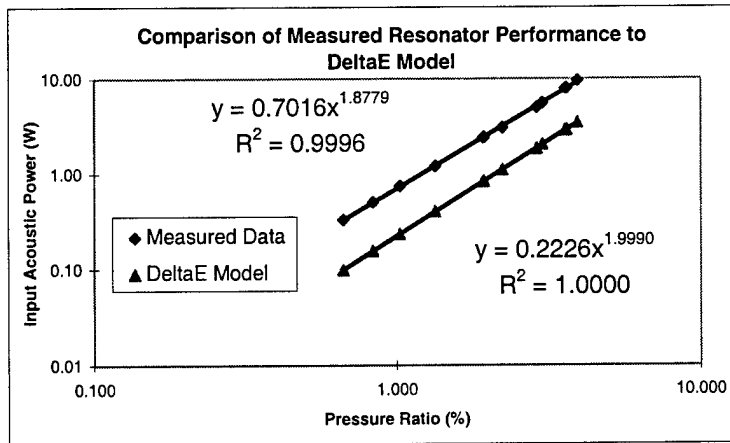


**Figure 4.9:** Frankenfridge resonator power requirements and DELTAE model (with HX\*\*\*\* segments) prediction.

fins act to speed up the flow (due to the fact that they constrict the cross-sectional area of the resonator) thereby increasing the viscous loss more than their simple duct counterparts.

#### 4.5. Conclusions

This project has successfully restored STAR to working condition with the addition of an exhaust heat flux measurement system and high-power driver. The exhaust heat flux measurement system has allowed the device to trade the complicated vacuum insulation used in the STAR experiments for a simple fiberglass insulation shield. The new driver can create stack power densities which are almost six times greater than STAR could obtain and has made the measurements presented in this thesis possible. Additionally, a good model of Frankenfridge has been created with the DELTAE software. It is important to keep in mind that the *COPR* for Frankenfridge is poor because the long stack, which was originally designed for a large temperature span and small cooling load, has now been used to pump five times as much heat at a much smaller temperature difference. A refrigerator designed for a low temperature span and high cooling power would exhibit a much higher *COPR*.

It was found that there is a small but measurable deviation in heat pumping power from the power predicted with a linear acoustic computer model. This deviation in heat pumping power at 4% pressure ratio is not more than 5% and at 6% pressure ratio is

about 15%. The correspondingly poorer coefficient-of-performance is small enough not to deter a thermoacoustic refrigerator designer from designing for high pressure ratio to take advantage of the dramatically increased power density.

While these experiments have shown excellent agreement with computer models of the stack, the resonator performance has significant deviations from the DELTAE model. The computer model predicts the acoustic power requirements to be 2/3 of the measured acoustic input power needed to reach a certain pressure ratio. This deviation is consistent in experiments (and the corresponding models) with (Figs. 4.2 and 4.3) and without (Fig. 4.9) the stack. The discrepancy is greater in the stackless resonator model because the stack is the dominant loss mechanism and reduces the effect of the resonator model inaccuracy.

The parameter  $Q$ , a dimensionless ratio of the amount of energy stored in a resonator compared to the amount of energy lost per acoustic cycle, is used to compare the model and the measured results. With the stack and heat exchangers in the resonator, the measured  $Q$  is 11.0 and the  $Q$  of the model is 11.7. This agreement is quite good because the loss in the stack dominates the other thermoviscous losses in the resonator. With the stack out, the measured  $Q$  increases to 56 while the model  $Q$  increases to 66. This shows that there is some thermoviscous resonator loss that is not modeled in DELTAE correctly. In Fig. 4.4 this discrepancy can be seen to be independent of acoustic amplitude which leads one to believe that the loss is not a nonlinear one, as turbulence would introduce, but a thermoviscous loss that is independent of drive amplitude, such as a small leak or gap in the resonator. It is also possible that this discrepancy in  $Q$  is evidence of an energy storage mechanism in the resonator that is not modeled in DELTAE.

Although there is significant disagreement between the curve of  $COPR$  for Frankenfridge compared to the Frankenfridge DELTAE model, there also exists a large discrepancy between the STAR data and the STAR DELTAE model as shown in Figs. 4.6 and 4.7. The hypothesized thermoviscous loss mechanism not modeled in DELTAE has apparently not been introduced in the Frankenfridge modification and construction. Indeed, it is possible that there is a problem with the DELTAE model, or a problem with the way it is used in this project or even with the software itself (although this last possibility is unlikely—DELTAE results have been verified on several other occasions.)

Further work on this project will be to find the loss mechanism that provides the disagreement between DELTAE and the measured data. The exhaust heat flux measurement system will also be examined to correct for the erroneous offset of about 2 W in a more rigorous way. Since the instrumentation of Frankenfridge has been so successful, it is hoped that Frankenfridge can be a test bed for research into new stack or heat exchanger designs.

## References

1. Shelley, M. W., *Frankenstein; or, The Modern Prometheus*, (London, Lackington and Co., 1818).
2. Garrett, S. L., Adeff J. A., Hofler, T. J., "Thermoacoustic Refrigerator for Space Applications," *AAIA J. Thermophys. Heat Trans.* **7**, 595-599 (1993).
3. Ballister, S. C., McKelvey, D. J., "Shipboard Electronics Thermoacoustic Cooler," Master of Science Thesis, Physics Department, Naval Postgraduate School, (1995). DTIC Report No. ADA 300514; U.S. Patent No. 5,647,216 (Jul. 15, 1997).
4. Adeff J. A., Garrett, S. L., Hofler, T. J. "Measurement of the Space Thermoacoustic Refrigerator Performance," Master of Science Thesis, Physics Department, Naval Postgraduate School, (1990). DTIC Report No. AD A241-320.
5. Moran, M. J., Shapiro, H. N. *Fundamentals of Engineering Thermodynamics, 2nd Ed.* (Wiley & Sons, New York, 1992).
6. Wheatley, J. C., Swift, G. W., Migliori, A., "The Natural Engine," *Los Alamos Science* **14**, (1986).
7. Swift, G. W., "Thermoacoustic Engines," *J. Acous. Soc. Am.* **84**, 1145-1180 (1988).
8. Ward, W. C. and Swift, G. W., *Design Environment for Low Amplitude Thermoacoustic Engines, Version 3.04b*. (Software available from Energy Science and Technology Center, U. S. DOE, Oak Ridge, Tennessee. <http://rott.esa.lanl.gov>).
9. Ward, W. C., Swift, G. W. *DELTAE Tutorial and Users Guide, Version 2.0*. (Los Alamos National Laboratory, LA-CC-93-8, Sept. 1995).
10. Swift, G. W. "Thermoacoustic Engines and Refrigerators," *Encyclopedia of Applied Physics, Vol. 21* (Wiley & Sons, New York, 1997), pp. 245-264.
11. Russel, R. A., "Energy Analysis of the Thermoacoustic Life Science Refrigerator," Master of Science Thesis, Physics Department, Naval Postgraduate School, (1994).
12. LabVIEW™ Full Development System Version 4.1, National Instruments Corporation, Austin, TX, 1997.
13. Incropera, F. P., DeWitt, D. P., *Fundamentals of Heat and Mass Transfer, 3rd Ed.* (Wiley & Sons, New York, 1990).

14. Garrett, S. L., "Thermoacoustics Life Sciences Refrigerator: Heat Exchanger Design and Performance Prediction", June (1992); Garrett, S. L., Perkins, D. K., Gopinath, A., "Thermoacoustic Refrigerator Heat Exchangers: Design, Analysis and Fabrication," *Heat Transfer 1994* Proc. 10th International Heat Trans. Conf. 4, 375-380 (1994).
15. Fox, R. W., McDonald, A. T., *Introduction to Fluid Mechanics 4th Ed.* (Wiley & Sons, New York, 1992).

## Appendix A. Effects of Stack Position on Engine Performance

---

---

The complicated equations that predict thermoacoustic heat transport given in the explanation of DELTAE in Chapter 2, or found in Swift's 1988 paper (Ref. 7) are much too cumbersome to easily understand. However, a much simpler set of equations can be written if the thermoacoustic stack is considered to be parallel plates that are very short compared to the acoustic wavelength and that this stack is short compared to the distance that the stack is positioned from the rigid end of the resonator. A short stack<sup>7</sup> allows the magnitude of acoustic pressure and velocity oscillations to be considered constant throughout the stack which simplifies the equations dramatically. Further, if the viscosity of the gas is ignored, there is no dependence of fluid velocity in the direction normal to the stack plates (perpendicular to the acoustic flow).

A sound wave not near a boundary is largely adiabatic, which means that a parcel of the medium (assumed to be compressible ideal gas in this development) experiences a temperature change as it is expanded and compressed. The term, "parcel of gas" refers to a small element of gas that is composed of many molecules so that a macroscopic treatment of the element can be applied, but the element is small enough that the material properties and acoustic variables may be treated as constant within the element. The temperature change of a parcel of gas is related to the pressure change with the following expression:

$$T_1 = \left( \frac{\partial T}{\partial p} \right)_s p_1 \quad (A.1)$$

Using a Maxwell relation, along with the fact that the inverse of specific volume is the density ( $\frac{1}{v} = \rho$ ) this expression can be written as:

$$T_1 = -\frac{1}{\rho_m^2} \left( \frac{\partial \rho}{\partial s} \right)_p p_1 \quad (A.2)$$

where  $s$  is the entropy per unit mass of the gas parcel. By the standard properties of partial derivatives, Eq. (A.2) can be written as,

$$T_1 = -\frac{1}{\rho_m^2} \left( \frac{\partial \rho}{\partial T} \right)_p \left( \frac{\partial T}{\partial s} \right)_p p_1 \quad (A.3)$$

which allows convenient substitution of the isobaric coefficient of thermal expansion when the expansion coefficient is expressed as  $\beta = -\frac{1}{\rho_m}(\frac{\partial \rho}{\partial T})_p$ .

The First Law of Thermodynamics can be written as:

$$\delta Q = \delta U + \delta W \quad (A.4a)$$

$$T_m ds = c_p dT - v dp \quad (A.4b)$$

where  $c_p$  is the gas specific heat at constant pressure and  $v$  is specific volume. If this expression of the First Law is considered for a constant pressure process, the second term on the right vanishes and:

$$\left(\frac{\partial T}{\partial s}\right)_p = \frac{T_m}{c_p} \quad (A.5)$$

which can substitute nicely into Eq. (A.3) to give:

$$T_1 = \frac{T_m \beta}{\rho_m c_p} \quad (A.6)$$

For fluid that can thermally communicate with the stack, the heat per unit volume of the fluid that is transferred perpendicular to the direction of acoustic flow is  $\rho_m c_p \delta T$ , where  $\delta T$  is the change in fluid temperature due to the flow of heat. The volume velocity of the fluid that is considered to be thermally active is  $\Pi \delta_\kappa u_1$  where  $\Pi$  is the perimeter of the stack measured transversely to the acoustic flow direction,  $\delta_\kappa$  is the thermal penetration depth (see Eq. (2.6)) and  $u_1$  is the acoustic velocity magnitude. The product of these two quantities (the change in heat per unit volume and the volume velocity of thermally active fluid) is the thermoacoustic heat flux given below:

$$\dot{Q} \sim \Pi \delta_\kappa u_1 \rho_m c_p \delta T \quad (A.7)$$

From a picture like the one in Fig. 2.4 in Chapter 2, one can see that

$$\delta T = 2T_1 - 2x_1 \nabla T = T_1 \left(1 - \frac{\nabla T}{T_1/x_1}\right) \quad (A.8)$$

where  $\nabla T$  is the temperature gradient along the stack and  $x_1$  is the peak acoustic displacement.

The critical gradient, as defined in Eq. (2.7) is the value of  $\nabla T$  that makes  $\delta T = 0$ . In the short stack approximation, the critical gradient is

$$\nabla T_{crit} = \frac{T_1}{x_1} \quad (A.9)$$

If we call  $\Gamma$  the ratio of  $\nabla T / \nabla T_{crit}$  and combine Eqs. (A.7) and (A.8) we get:

$$\dot{Q} \sim \Pi \delta_\kappa T_m \beta p_1 u_1 (\Gamma - 1) \quad (A.10)$$

This expression points out that when  $\Gamma < 1$  heat flows against the temperature gradient as in a refrigerator. When  $\Gamma > 1$  heat flows “downhill” and the device operates as a prime mover. When  $\Gamma = 1$  heat does not flow and the cycle does no useful work.

The work flux is estimated by considering the volume change experienced by a parcel of gas as it translates an acoustic displacement and is acted on by the acoustic pressure. This volume change is expressed as

$$\frac{\delta V}{V} = \beta \delta T \quad (A.11)$$

where  $V$  is the total volume of gas that is thermodynamically active and is equal to  $\Pi \delta_\kappa \Delta x$ . In this expression,  $\Delta x$  is the length of the stack. The work flux, in general, is  $p_1 \delta V \omega$  and by combining Eqs. (A.6), (A.8), (A.10) and Eq. (A.11) we can express the work flux as

$$\dot{W} \sim \Pi \delta_\kappa \frac{T_m \beta^2}{\rho_m c_p} p_1^2 \omega \Delta x (\Gamma - 1) \quad (A.12)$$

If we employ another thermodynamic relation,  $\gamma - 1 = \frac{T_m \beta^2 a^2}{c_p}$  where  $\gamma$  is the polytropic coefficient, or the ratio of the specific heat of an ideal gas at constant pressure to the specific heat at constant volume, and  $a$  is the speed of sound. Using this equality we can recast the work flux in a more convenient form for ideal gases:

$$\dot{W} \sim \Pi \delta_\kappa (\gamma - 1) \frac{p_1^2}{\rho_m a} (\Gamma - 1) k \Delta x \quad (A.13)$$

where the wavenumber,  $k$ , is equal to  $\omega/a$ . In the short stack approximation, both heat and work flux are quadratic in the acoustic pressure or velocity and both heat and work flux change sign as  $\Gamma$  passes through unity.

As discussed in Chapter 2, the efficiency or COP of an engine relates the heat flux to the work flux. In a refrigerator, the COP is

$$COP = \frac{\dot{Q}}{\dot{W}} \quad (A.14)$$

into which we can substitute our new expressions for heat and work flux to obtain Eq. (A.15). The COP will be regarded as an equality even though the above expressions for heat and

work flux were not — had we developed the equations quantitatively there would be a coefficient of 1/4 multiplying each expression.

$$COP = \frac{\rho_m a (T_m \beta) u_1}{(\gamma - 1) k \Delta x p_1} \quad (A.15)$$

The above expression can be further simplified for sinusoidal excitation where  $u_1 = u_0 \sin kx$  and  $p_1 = \rho_m a u_0 \cos kx$ . Making these substitutions yields this simple expression for COP:

$$COP = \frac{T_m \beta}{(\gamma - 1) k \Delta x} \tan kx \quad (A.16)$$

By noticing that there is a good deal of similarity between the above expression for COP and the expression for critical temperature gradient in Eq. (2.8), the COP could be expressed as

$$COP = \frac{T_m}{\nabla T_{crit} \Delta x} \quad (A.17)$$

The Carnot coefficient of performance is realized when the temperature increase  $\delta T$  approaches zero — or when the actual temperature gradient approaches the critical temperature gradient. Since  $\Delta T = \Delta x \nabla T_{crit}$  when  $\nabla T = \nabla T_{crit}$ , the coefficient of performance at this operating point is

$$COP = \frac{T_m}{\Delta T} \quad (A.18)$$

Since the Carnot COP is  $\frac{T_c}{T_h - T_c}$  and if  $\Delta T/T_c$  is small so that  $T_c$  can be replaced by  $T_m$ , then the expression for Carnot COP is Eq. (A.18). The actual temperature gradient approaches the critical temperature gradient when the stack is moved very near the driven end of the resonator.

Although this expression is quite simple, several important things have been left out. The inclusion of viscosity and thermal conduction in the stack and the gas parallel to the acoustic flow are two such omissions. If the development of heat and work flux are done carefully, with consideration of viscosity and thermal conduction, the following expressions result<sup>7</sup> if  $y_0 \sim \delta_\kappa$ :

$$\dot{H}_2 = -\frac{1}{4} \Pi \delta_\kappa \frac{T_m \beta p_1 \langle u_1 \rangle}{(1 + \epsilon_s)(1 - \sqrt{\sigma})} (\Gamma - 1) - \Pi (y_0 K_g + l K_s) \frac{dT_m}{dx} \quad (A.19)$$

and

$$\dot{W}_2 = \frac{1}{4} \Pi \delta_\kappa \Delta x \frac{(\gamma - 1) \omega (p_1)^2}{\rho_m a^2 (1 + \epsilon_s)} (\Gamma - 1) - \frac{1}{4} \Pi \delta_\nu \Delta x \omega \rho_m \langle u_1 \rangle^2 \quad (A.20)$$

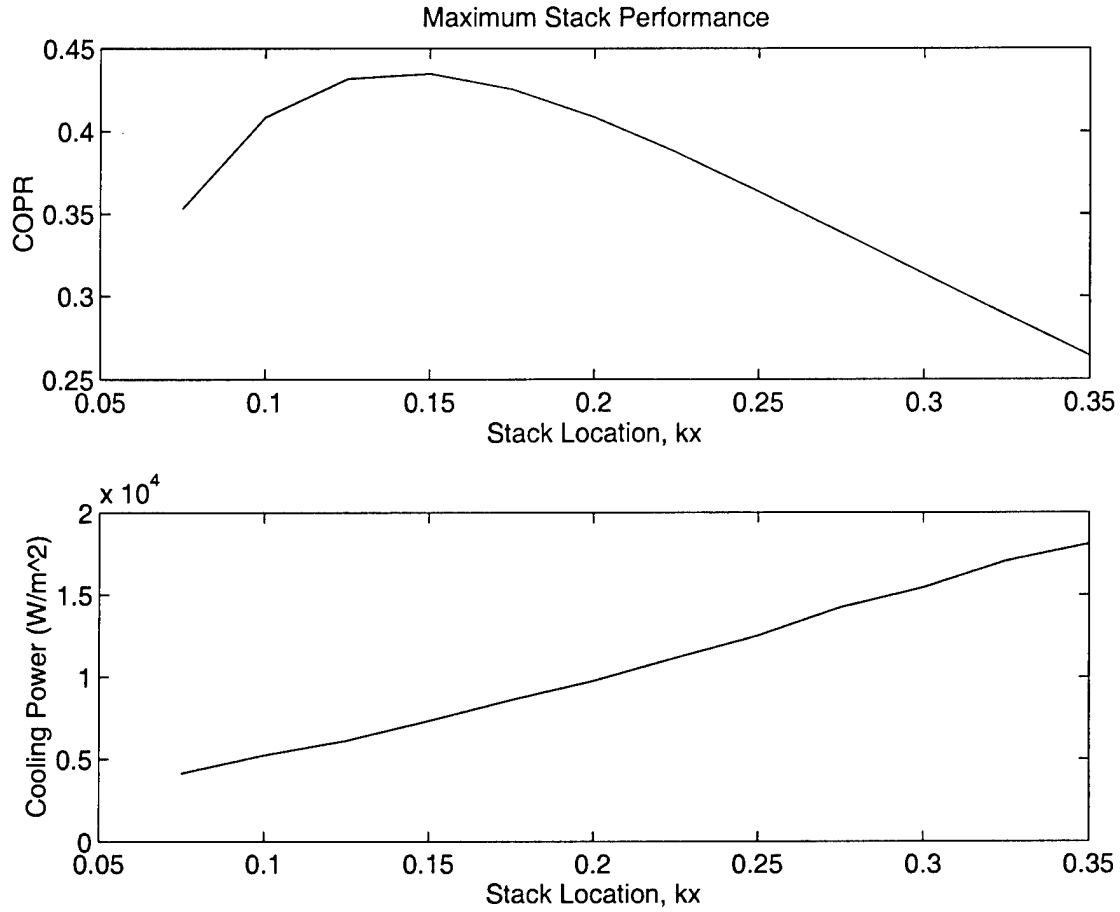


**Figure A.1:** Stack performance as a function of stack position in the standing wave

Eq. (A.19) is an expression for the enthalpy, or total energy flux, which is the sum of the heat and work flux, or,  $\dot{H}_2 = \dot{Q}_2 + \dot{W}_2$ . Indeed, Eq. (A.19) looks much like our  $\dot{Q}$  except that it has some extra terms in the denominator, a specific heat correction ( $\epsilon_s$ ) for the stack material and the square root of the Prandtl number ( $\sigma$ ). The second term, the one that subtracts energy from the first term, represents the heat loss due to conduction in the stack and the gas in the direction parallel to acoustic propagation. The fact that the enthalpy and work flux variables have a subscript 2 signifies that they are second order in the acoustic variables,  $p_1$  and  $u_1$ , which are first order. Just like the expanded enthalpy equation, the work flux equation, Eq. (A.20) has an extra term that represents the extra viscous loss caused by the stack.

Using these equations, an idea of the effect that  $kx$  has on efficiency and heat pumping power can be quantitatively explored. Fig. A.1 illustrates that as the stack is moved away from the driven end of a refrigerator, the COP relative to Carnot comes to a peak at some small distance from the driver and then decreases monotonically. When the stack is right against the driver face the magnitude of the pressure oscillations is very large and consequently the stack temperature span is large. This large temperature span causes the thermal conduction “down” the stack to decrease the COPR. As the stack moves away from the driven end into the “sweet spot” that gives highest COPR, the refrigerator is pumping very little heat and the actual temperature gradient is very close to the critical temperature gradient. (In fact, the idea of critical temperature gradient as a single number is not true in the presence of viscosity. It really spans a range of values, sort of a “no man’s land” where the device is neither a refrigerator nor a heat pump.)

To be able to pump more heat, the stack must be moved into a region where the velocity amplitudes are greater, which implies larger viscous losses in the stack. Although the COP gets larger for increasing stack position ( $kx$ ), the Carnot COP goes to infinity as the magnitude of the pressure oscillations go to zero at the pressure node (because the stack temperature difference,  $\Delta T$ , approaches zero). This increase in Carnot COP is larger than the increase in COP for a given increase in  $kx$  which makes the ratio of COPR decrease. The lower plot in Fig. A.1 shows that the stack can pump more heat as the stack moves away from the driven end.

Because the stack in Frankenfridge is not at all short, according to our criterion, a shorter stack length was used to create the graphs in Fig. A.1. In addition, some of the values for gas mixture thermophysical parameters are not the values that are accurate for the Frankenfridge device. Although the values used in this exercise are realistic, the purpose is to point out the dependence of stack performance on the position of the stack in the standing wave.

## Appendix B.

# Heat Capacity of the Cold Side Resonator

---



---

The heat capacity of the resonator section that gets cold is easily computed. The table below summarizes the mass of each component of Frankenfridge that gets cold.

**Table B.1:** Mass and specific heat of cold side resonator components (specific heat values taken from Incropera & DeWitt<sup>13</sup>)

<i>Component</i>	<i>Mass (g)</i>	<i>Material Specific Heat, (<math>\frac{J}{kgK}</math>)</i>
Reducer	132.95	Copper, 385
Trumpet	56.51	Copper, 385
Joining Ring	4.90	Copper, 385
Cold Heat Exchanger	4.63	Copper, 385
Bulb Fitting	14.45	Stainless Steel, 477
Bulb	203.35	Stainless Steel, 477
Thermal Switch	36.10	Bronze, 380

The calculated heat capacity of these components, calculated with these values, amounts to 194 J/K.

The heat capacity can also be inferred from a set of data recorded at the end of Run #6. With Frankenfridge being driven at its record-setting 6% pressure ratio, at a cold side temperature of 17.2 °C, pumping 26.5 W of heat, the heat load was removed and the temperature of the cold side allowed to drop as low as the insulation would allow. One can imagine that in the first ten or so seconds, the heat pumped from the cold side is still around 26.5 W as the fridge starts to pump out the heat stored in the cold side hardware. Since the data acquisition rate was increased to a 10 second sampling rate, these critical initial points are recorded. The heat removal rate from the cold hardware is

$$\frac{d}{dt} [Q] = \frac{d}{dt} [mc_p\Delta T] \quad (B.1)$$

If the  $\Delta T$  term is a function of time (which it is in this experiment), the heat flux on the cold side is a function of the time rate of change the temperature. A graph of this temperature dependence in Frankenfridge is shown in Fig. B.1.

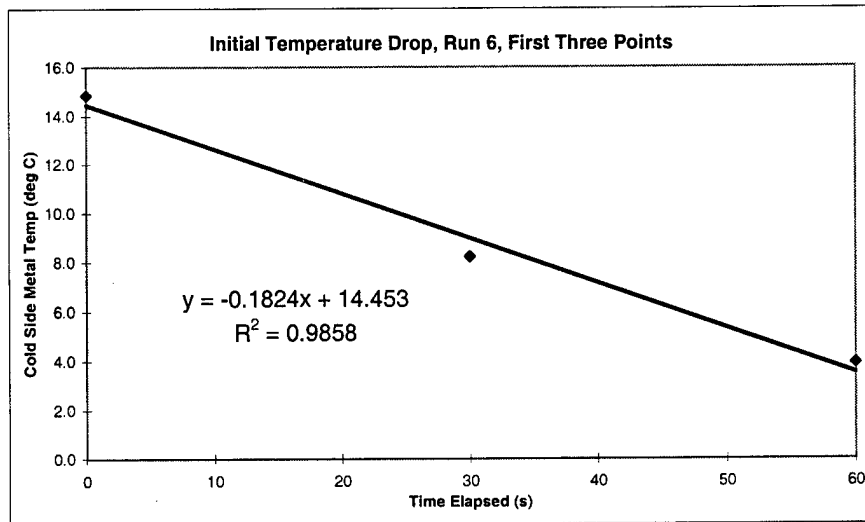


**Figure B.1:** Graph of the initial temperature drop in Run #6.

If the heat flux is taken to be 26.5 W during this 60 seconds, then the heat capacity of the cold side hardware can be inferred. Taking the magnitude of  $\frac{\Delta T}{dt}$  to be  $0.18 \pm 0.02$  °C/s yields a value for heat capacity of 145 J/K which is comparable to the calculated value (the calculated value is 34% larger).

## **Appendix C.**

# **Manufacturer Specifications of Sensors**

---

---

This appendix includes the manufacturers specifications of the sensors used in Frankenfridge. Unfortunately, the exact serial numbers of the Entran accelerometer and Endevco microphone that are inside of the driver are not known (without breaking the driver apart). For these sensors, the generic specification sheet is included.

Also included in this section is information about the PR100 preamplifier for the piezoresistive strain gauge sensors. These amplifiers were made in the lab in May of 1997.

The pages in this appendix are numbered consecutively with the body of the thesis.

## Piezoresistive Pressure Transducer

**ENDEVCO**  
**MODEL**  
**8510B**

### Model 8510B-200, -500 and -2000

- 200 to 2000 psi, 300 mV Full Scale
- Rugged, Miniature

#### DESCRIPTION

The ENDEVCO® Model 8510B is a rugged, miniature, high sensitivity piezoresistive pressure transducer. It has a 10-32 mounting thread, 0.15 inch (3.8 mm) face diameter and is available in ranges from 1 psi to 2000 psi. Its high sensitivity combined with resonance makes it ideal for measuring dynamic pressure.

ENDEVCO pressure transducers feature a four-active arm strain gage bridge diffused into a unique sculptured silicon diaphragm for maximum sensitivity and wideband frequency response. Self-contained hybrid temperature compensation provides stable performance over the temperature range of 0°F to 200°F (-18°C to +93°C). ENDEVCO transducers also feature excellent linearity (even to 3X range), high shock resistance, and negligible sensitivity to temperature transients.

The Model 8510B is designed for a wide variety of aerospace, automotive and industrial measurements which require a combination of small size, high sensitivity, and wideband frequency response. Its vent tube may be connected to a standard reference manifold or used for differential pressure measurements.

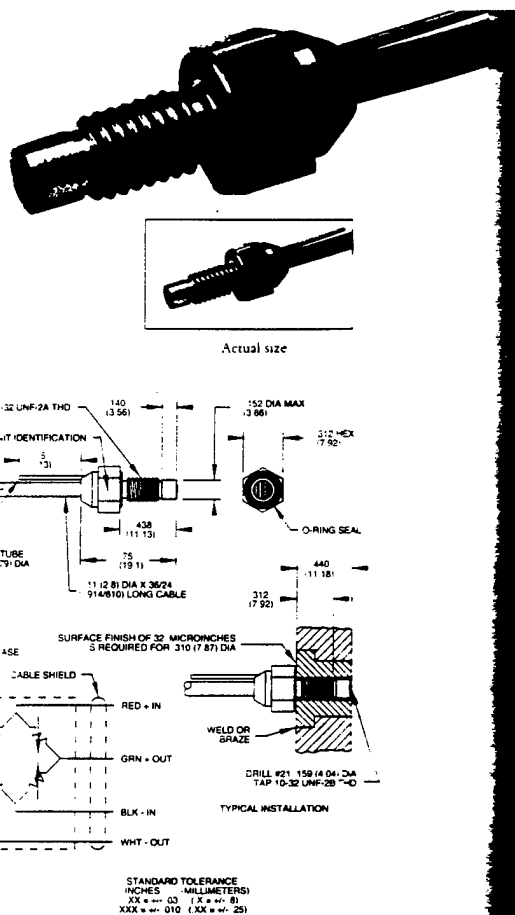
The Model 8510B is available with Metric M5X0.8 mounting thread as 8510B-XXM5 on special order.

ENDEVCO Model 106/109 Dual Channel System, Model 4430A Signal Conditioner, or Model 68207 BCAS™ Computer Controlled System are recommended as signal conditioner and power supply.

#### SPECIFICATIONS

**CERTIFIED PERFORMANCE:** All specifications assume +75°F (+24°C) and 10 Vdc excitation unless otherwise stated. The following parameters are 100% tested. Calibration data, traceable to the National Institute of Standards and Technology (NIST), is supplied.

	Model		
RANGE [1]	Units	8510B-200	-500
POSITIVE SENSITIVITY [2]	psig	0 - 200	0 - 500
COMBINED: NON-LINEARITY, NON-REPEATABILITY, PRESSURE HYSERESIS [3]	% FSO RSS Max	0.50	0.50
Non-Linearity, Independent	% FSO Typ	0.25	0.25
Non-Repeatability	% FSO Typ	0.1	0.1
Pressure Hysteresis	% FSO Typ	0.1	0.1
ZERO MEASURAND OUTPUT [3]	mV Max	±10	±10
ZERO SHIFT AFTER 3X RANGE	±% 3X FSO Max	0.2	0.2
THERMAL ZERO SHIFT			
From 0°F to 200°F (-18°C to +93°C)	±% FSO Max	3	3
THERMAL SENSITIVITY SHIFT			
From 0°F to 200°F (-18°C to +93°C)	±% Max	4	4



# ENDEVCO Piezoresistive Pressure Transducer

## MODEL 8510B

### SPECIFICATIONS—continued

TYPICAL PERFORMANCE CHARACTERISTICS The following parameters are established from testing of sample units.

	Units	Model	-500	-2000
RESONANCE FREQUENCY	Hz	8510C-200 320 000	500 000	900 000
NON-LINEARITY AT 3X RANGE	% 3X FSO	1	1	1
HERMAL TRANSIENT RESPONSE PER ISA-S37.10, PARA. 6.7, PROCEDURE I	psv/F psv/C	0.01 0.02	0.01 0.02	0.16 0.30
PHOTOFASL RESPONSE [5]	Equiv. psv	28	70	1300
WARM-UP TIME [6]	ms	1	1	1
ACCELERATION SENSITIVITY	Equiv. ps/vg	0.0003	0.0004	0.00027
BURST PRESSURE (Diaphragm/Reference Side) [7]	psi Min	1000/300	2500/300	10 000/300

#### ELECTRICAL

FULL SCALE OUTPUT	300 ±100 mV at 10.0 Vdc
SUPPLY VOLTAGE [8]	10.0 Vdc recommended, 18.0 Vdc maximum
ELECTRICAL CONFIGURATION	Active four-arm piezoresistive bridge
POLARITY	Positive output for increasing pressure into (+) port (end with screen on it)
RESISTANCE	
Input	2000 ±800 ohms
Output	1600 ±500 ohms
Isolation	100 megohms minimum at 50 Volts; leads to case, leads to shield, shield to case
NOISE	5 microvolts rms typical, dc to 50 000 Hz; 50 microvolts rms maximum, dc to 50 000 Hz

#### MECHANICAL

CASE MATERIAL	Stainless Steel (17-4 PH CRES)
CABLE, INTEGRAL	Four conductor No. 32 AWG Teflon® insulated leads, braided shield, silicone jacket, 30 ±3 in (760 ±76 mm)
DEAD VOLUME (+) PORT	0.0003 cubic inches (0.005 cc)
MOUNTING/TORQUE	10-32 UNF-2A threaded case 0.438 inch (11.12 mm) long/15 ±5 lbf-in (1.7 ±0.6 Nm)
WEIGHT	2.3 grams (cable weighs 9 grams/meter)

#### ENVIRONMENTAL

MEDIA [9][10]	
TEMPERATURE [10][11]	-65°F to +250°F (-54°C to +121°C)
VIBRATION	1000 g pk
ACCELERATION	1000 g
SHOCK	20 000 g, 100 microsecond haversine pulse
HUMIDITY	Isolation resistance greater than 100 megohms at 50 volts when tested per MIL-STD-202E, Method 103B, Test Condition B

#### CALIBRATION DATA

Data supplied for all parameters in Certified Performance section. Optional calibrations available for all parameters in Typical Performance section

#### ACCESSORY

EHR93 O-Ring, Viton

#### OPTIONAL ACCESSORIES

EHR96 O-Ring, Fluorosilicone  
24328 4 Conductor Shielded Cable

#### NOTES

- Pressure ranges can be considered bidirectional, e.g., an 8510B-200 can be used to measure + or -200 psig. Sensitivity in the positive direction is typically within 1% of sensitivity in the negative direction. Sensitivity calibration provided with each unit is for the positive direction.
- 1 psi = 6 895 kPa = 0.069 bar.
- FSO (Full Scale Output) is defined as transducer output from 0 to full scale pressure, which is nominally 300mV.
- Measurand Output (ZMO) is the transducer output with 0 psig applied.
- Per ISA-S37.10, Para. 6.7, Proc. II. The metal screen partially shields the silicon diaphragm from incident radiation. Accordingly, light incident at acute angles to the screen generally increases the error by a factor of 2 or 3.

- Warm-up time is defined as elapsed time from excitation voltage "turn on" until the transducer output is within ±1% of reading accuracy.
- Reference side pressure may be 300 psi on all ranges if differential limits (psid) are not exceeded.
- Use of excitation voltages other than 10.0 Vdc requires manufacture and calibration at that voltage since thermal errors increase with high excitation voltages.
- Internal seals are epoxy compatible with clean dry gas media. Media in (+) measurand port is exposed to CRES, nickel-iron alloy, Parylene C, epoxy, and the VITON O-Ring. Media in (-) measurand port is exposed to the above and RTV silicon coating. For use in water or corrosive media, contact the factory for modifications and installation precautions which may be taken to extend service life.
- O-Ring, Parker 5-125, compound V747-75 (VITON) is supplied unless otherwise specified on purchase order. Fluorosilicone O-ring for leak-tight operation below 0°F is available on special order.
- Units can be compensated over any 200°F (93°C) span from -65°F to +250°F (-54°C to +121°C) on special order.

NOTE: Tighter Specifications are available on special order.

Continued product improvement necessitates that Endevco reserve the right to modify these specifications without notice. Endevco maintains a program of constant surveillance over all products to ensure a high level of reliability. This program includes attention to reliability factors during product design, the support of stringent Quality Control requirements, and compulsory corrective action procedures. These measures, together with conservative specifications, have made the name Endevco synonymous with reliability.

**ENDEVCO** 

**PRESSURE TRANSDUCER TEST REPORT**

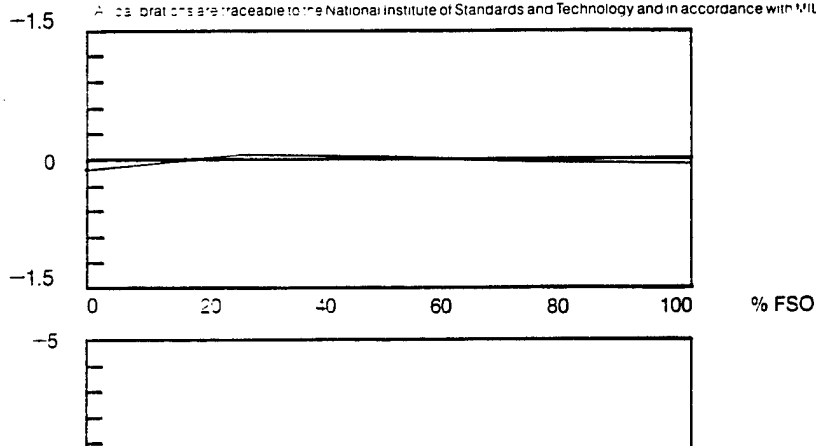
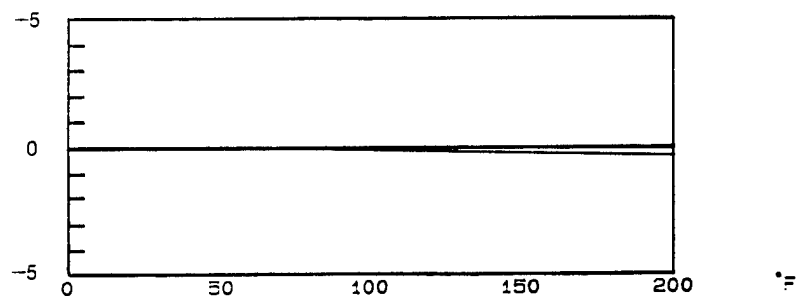
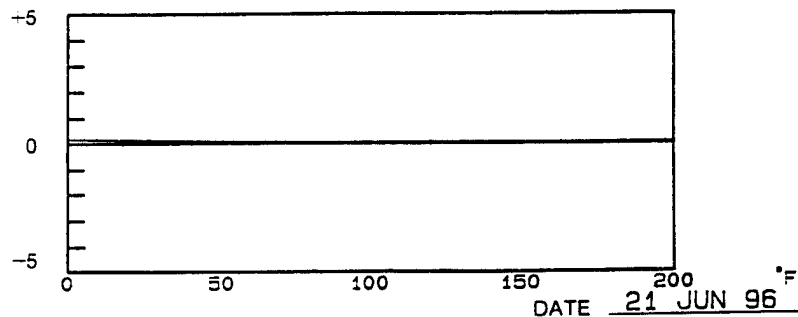
MODEL 8510B-200

SERIAL # 10063

Range	200	psig
Sensitivity	1.45	mV/psi
Excitation	10.00	Vdc
Zero Pressure Output	1	mV
Full Scale Output	290	mV
Non-Linearity	.09	%FSO
Hysteresis	.03	%FSO
Non-Repeatability	.03	%FSO
Combined Lin., Hyst., & Rep.*	.1	%FSO
Thermal Zero Shift	.31	%FSO
Zero Shift After 3 X FSO	.01 %	3 X FSO
Thermal Sensitivity Shift	.14	%
Input Resistance	1690	$\Omega$
Output Resistance	1526	$\Omega$
Isolation Resistance	>100	M $\Omega$

\*RSS

All calibrations are traceable to the National Institute of Standards and Technology and in accordance with MIL-STD-45662A.

NON-LINEARITY  
(% FSO)THERMAL  
ZERO  
SHIFT  
(% FSO)THERMAL  
SENSITIVITY  
SHIFT  
(%)

DATE 21 JUN 96





## Piezoresistive Pressure Transducer

**ENDEVCO  
MODEL  
8514**

### Model 8514-10, -20 and -50

- 10 to 50 psi, 300 mV Full Scale
- Rugged, Subminiature
- 0.065 Inch Diameter

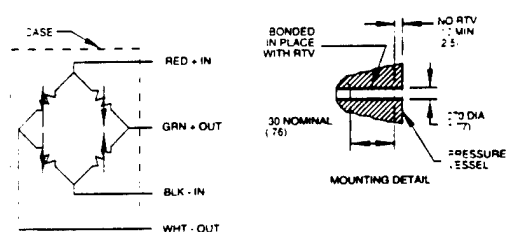
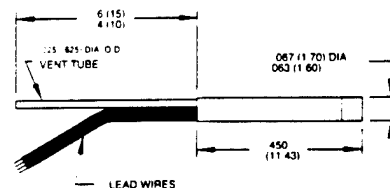
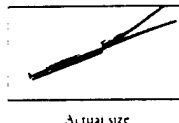
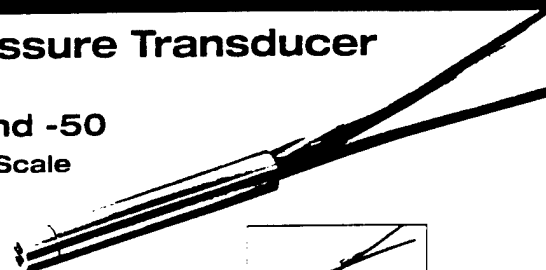
#### DESCRIPTION

The ENDEVCO® Model 8514 is a rugged, subminiature piezoresistive pressure transducer. It has a case diameter of only 0.065 inch (1.65 mm) and is available in ranges from 10 to 50 psi full scale. Full scale output is 300 mV with high overload capability and high frequency response.

ENDEVCO pressure transducers feature an active four-arm strain gage bridge diffused into a sculptured silicon diaphragm for maximum sensitivity and wideband frequency response. Self-contained hybrid temperature compensation provides stable performance over the wide temperature range of 0°F to 200°F (-18°C to +93°C). ENDEVCO transducers also feature excellent linearity (even to 3X range), high shock resistance, and high stability during temperature transients.

The Model 8514 can be installed in locations which are difficult to reach. Its small size permits flush mounting on curved surfaces. Its high sensitivity combined with small size and high resonance makes the Model 8514 suitable for use on small-scale models in wind tunnels.

ENDEVCO Model 106/109 Dual Channel System, Model 4430A Signal Conditioner, or Model 68207 BCAS™ Computer Controlled Systems are recommended as signal conditioner and power supply.



STANDARD TOLERANCE  
(INCHES / MILLIMETERS)  
XX = +/- .03 (X = +/- .8)  
XXX = +/- .010 (XX = +/- .25)

#### SPECIFICATIONS

**CERTIFIED PERFORMANCE:** All specifications assume +75°F (+24°C) and 10 Vdc excitation unless otherwise stated. The following parameters are 100% tested. Calibration data, traceable to the National Institute of Standards and Technology (NIST), is supplied.

RANGE [1]	Units	Model		
		8514-10	-20	-50
POSITIVE SENSITIVITY [1]	mV/psi	30 ± 10	15 ± 5	6 ± 2
COMBINED: NON-LINEARITY, NON-REPEATABILITY.				
PRESSURE HYSERESIS [2]	% FSO RSS Max	1.0	0.50	0.50
Non-Linearity, Independent	% FSO Typ	0.50	0.25	0.25
Non-Repeatability	% FSO Typ	0.1	0.1	0.1
Pressure Hysteresis	% FSO Typ	0.1	0.1	0.1
ZERO MEASURAND OUTPUT [3]	mV Max	± 10	± 10	± 10
ZERO SHIFT AFTER 3X RANGE	± % 3X FSO Max	0.1	0.1	0.1
THERMAL ZERO SHIFT				
From 0°F to 200°F (-18°C to +93°C)	± % FSO Max	3	3	3
THERMAL SENSITIVITY SHIFT				
From 0°F to 200°F (-18°C to +93°C)	± % Max	4	4	4

## ENDEVCO Piezoresistive Pressure Transducer

### MODEL

### 8514

#### SPECIFICATIONS—continued

TYPICAL PERFORMANCE CHARACTERISTICS: The following parameters are established from testing of sample units.

	Model	8514-10	-20	-50
RESONANCE FREQUENCY	Units	140 000	180 000	320 000
NON-LINEARITY AT 3X RANGE	% 3X FSO	1.0	0.7	0.5
THERMAL TRANSIENT RESPONSE PER	psr/F	0.001	0.003	0.005
ISA-S37.10, PARA. 6.7. PROCEDURE I [4]	psr/C	0.002	0.005	0.009
PHOTOFASh RESPONSE, [5]	Equiv. psi	0.1	0.5	1.0
WARM-UP TIME [6]	ms	1	1	1
ACCELERATION SENSITIVITY				
Longitudinal	Equiv. psr/g	0.00015	0.0002	0.0003
Lateral	Equiv. psr/g	0.00006	0.00005	0.0002
BURST PRESSURE				
(Diaphragm/Reference Side)	psi Min	100/25	150/25	200/25
ELECTRICAL				
FULL SCALE OUTPUT	300 ±100 mV at 10.0 Vdc			
SUPPLY VOLTAGE [5]	10.0 Vdc recommended, 18 Vdc maximum			
ELECTRICAL CONFIGURATION	Active four-arm piezoresistive bridge			
POLARITY	Positive output for increasing pressure into (+) port (end with screen on it)			
RESISTANCE				
Input	1800 ±800 ohms			
Output	1600 ±500 ohms			
Isolation	100 megohms minimum at 50 Volts; leads to case, leads to shield, shield to case			
NOISE	5 microvolts rms typical, dc to 50 000 Hz; 50 microvolts rms maximum, dc to 50 000 Hz			
MECHANICAL				
CASE, MATERIAL	Nickel - Iron Alloy			
CABLE, INTEGRAL	Four leadwires No. 36 AWG solid copper conductor, FEP Teflon® insulated 30 ±3 in. (760 ±76 mm)			
DEAD VOLUME (+) PORT	0.000015 cubic inches (0.0002 cc)			
MOUNTING	Bond into #50 drill hole (1.78 mm) using an RTV, such as DOW CORNING Silastic® 738; RTV is not permitted within 0.10 inch (2.5 mm) of unit's face			
WEIGHT (excluding lead wires)	0.08 gram (Leadwires weigh 0.9 grams/meter. Sleeved leadwires weigh 2 grams/meter)			
ENVIRONMENTAL				
MEDIA	Internal seals are epoxy and are compatible with clean dry gas media. Media in (+) measurand port is exposed to nickel-iron alloy, Parylene C, and epoxy. For use in water or corrosive media, contact the factory for modifications and installation precautions which may be taken to extend service life			
TEMPERATURE [7]	-65°F to +250°F (-54°C to +121°C)			
VIBRATION	1000 g pk			
ACCELERATION	1000 g			
SHOCK	20 000 g, 100 microsecond half-sine pulse			
HUMIDITY	Isolation resistance greater than 100 megohms at 50 volts, per MIL-STD-202E, Method 103B, Test Condition B. External case is sealed with epoxy. Circuit within case, vented through tube, is coated with Parylene C			
CALIBRATION DATA				
	Data supplied for all parameters in Certified Performance section. Optional calibrations available for all parameters in Typical Performance section			

#### OPTIONAL ACCESSORIES

25011-1	Leadwire Red
25011-2	Leadwire Black
25011-3	Leadwire White
25011-4	Leadwire Green

#### NOTES

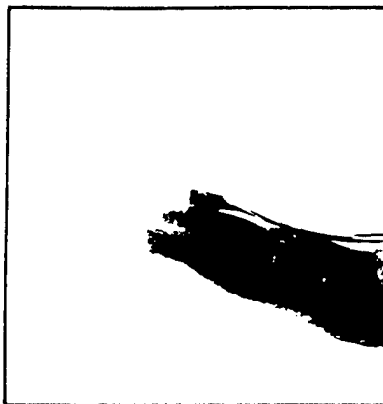
- 1 psi = 6.895 kPa = 0.069 bar.
- FSO (Full Scale Output) is defined as transducer output change from 0 psig to + full scale pressure. Calibration provided is for positive pressure.

3. Zero Measurand Output (ZMO) is the transducer output with 0 psig applied.
4. Use of excitation voltages other than 10.0 Vdc requires manufacture and calibration at that voltage since thermal errors increase with high excitation voltages.
5. Per ISA-S37.10, Para 6.7, Procedure II.
6. Warm-up time is defined as elapsed time from excitation voltage "turn on" until the transducer output is within ±1% of reading accuracy.
7. Units can be compensated over any 200°F (93°C) span from -65°F to +250°F (-54°C to +121°C).

NOTE: Tighter specifications are available on special order.

Continued product improvement necessitates that Endevco reserve the right to modify these specifications without notice. Endevco maintains a program of constant surveillance over all products to ensure a high level of reliability. This program includes attention to reliability factors during product design, the support of stringent Quality Control requirements, and compulsory corrective action procedures. These measures, together with conservative specifications, have made the name Endevco synonymous with reliability.

**Entran®**



## “OFF-THE-SHELF” STOCK PROGRAM

### EGA-125 Series Miniature Accelerometers

- 5g TO 5000g RANGES
- TO 250 mV FULL SCALE
- VARIETY OF MOUNTINGS – SMALL SIZE & WEIGHT
- STEADY STATE AND DYNAMIC RESPONSE

Entran's EGA-125 Series accelerometers are a state of the art achievement in miniature accelerometer design. Developed with the user in mind, the EGA offers an optimum combination of characteristics which permit acceleration, vibration and shock measurements where small size and mass are of prime importance.

The EGA's rugged construction eliminates the fragility normally associated with miniature accelerometers. Entran's EGA is offered in a variety of mounting styles to allow ease of handling and mounting. This mounting versatility is well suited to meet most requirements from aerospace to industrial usage and is available at no extra charge. 0.7cr damping is also available as an option.

The EGA-125 is a piezoresistive accelerometer which com-

bines a fully active semiconductor Wheatstone bridge with the technology of sensor design. Its high output enables the EGA to drive most recorders and data monitoring systems directly, without amplification or costly signal conditioning. The semiconductor circuitry is fully compensated for temperature changes in the environment and possesses excellent thermal characteristics.

The EGA-125 is functional from steady state to high dynamic responses and is ranged for "g" loads which are commonly experienced in research, testing, and control. Available in "g" ranges from 5g to 5000g. Entran's EGA miniature accelerometer is well suited for a myriad of applications from aerospace to consumer industries. Typical applications vary in scope from flutter testing to wind tunnel models to vibratory and shock disturbances in industrial testing.

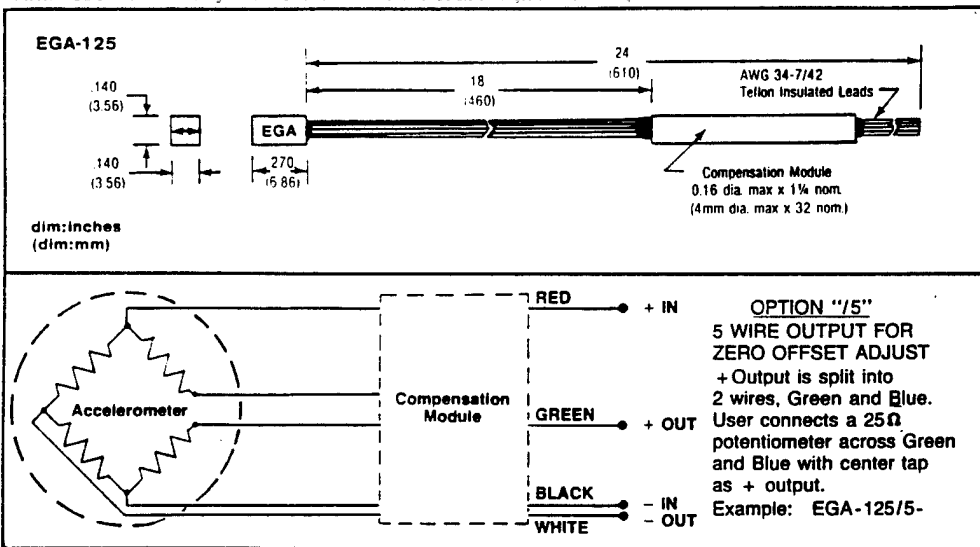
## SPECIFICATIONS

MODEL	EGA-125 -5	EGA-125 -10	EGA-125 -25	EGA-125 -50	EGA-125 -100	EGA-125 -250	EGA-125 -500	EGA-125 -1000	EGA-125 -2500	EGA-125 -5000
RANGE	$\pm 5g$	$\pm 10g$	$\pm 25g$	$\pm 50g$	$\pm 100g$	$\pm 250g$	$\pm 500g$	$\pm 1000g$	$\pm 2500g$	$\pm 5000g$
OVERRANGE	$\pm 25g$	$\pm 50g$	$\pm 125g$	$\pm 250g$	$\pm 500g$	$\pm 1250g$	$\pm 2500g$	$\pm 3000g$	$\pm 5000g$	$\pm 10000g$
SENS. mV/g nom.	15	12	5	4	2.5	1	0.5	0.25	0.1	0.05
RES. FREQ. nom.	300 Hz	500 Hz	1000 Hz	1200 Hz	1500 Hz	2000 Hz	3000 Hz	4000 Hz	6000 Hz	8000 Hz

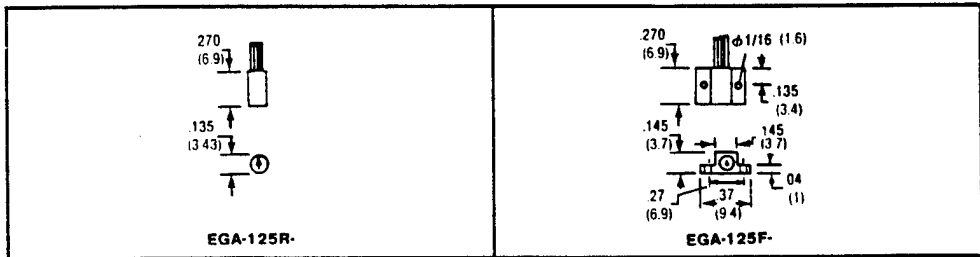
\* "OFF-THE-SHELF" STOCK IN EGA-125-10D, -100D, -250D AND -1000D AND EGA-125F-10D, -100D AND -250D DAMPED VERSIONS.

NON-LINEARITY	$\pm 1\%$
TRANSVERSE SENS.	3% max.
THERMAL ZERO	<sup>4.5</sup> $\pm 1\%$ FS/100°F
THERMAL SENS.	$\pm 2\frac{1}{2}\%$ /100°F
WEIGHT	1/2 gram nom. (w/o leads)

<sup>1</sup> Useful frequency range is 20% of Resonant Frequency. <sup>2</sup> Overrange for use within 30% of Resonant Frequency. <sup>3</sup> Available with 0.7cr damping to increase useful range as high as 50% of resonance with overrange at all frequencies (see Bulletin EGDAMP). <sup>4</sup> Zero offset of  $\pm 15mV$  typ. at 80°F after warm-up. Lower values available on request. <sup>5</sup>  $\pm 2\frac{1}{2}\%$ FS./100°F for 5g Model. <sup>6</sup> Other Excitations and Temperature Ranges available on request.



## OPTIONAL MOUNTING STYLES

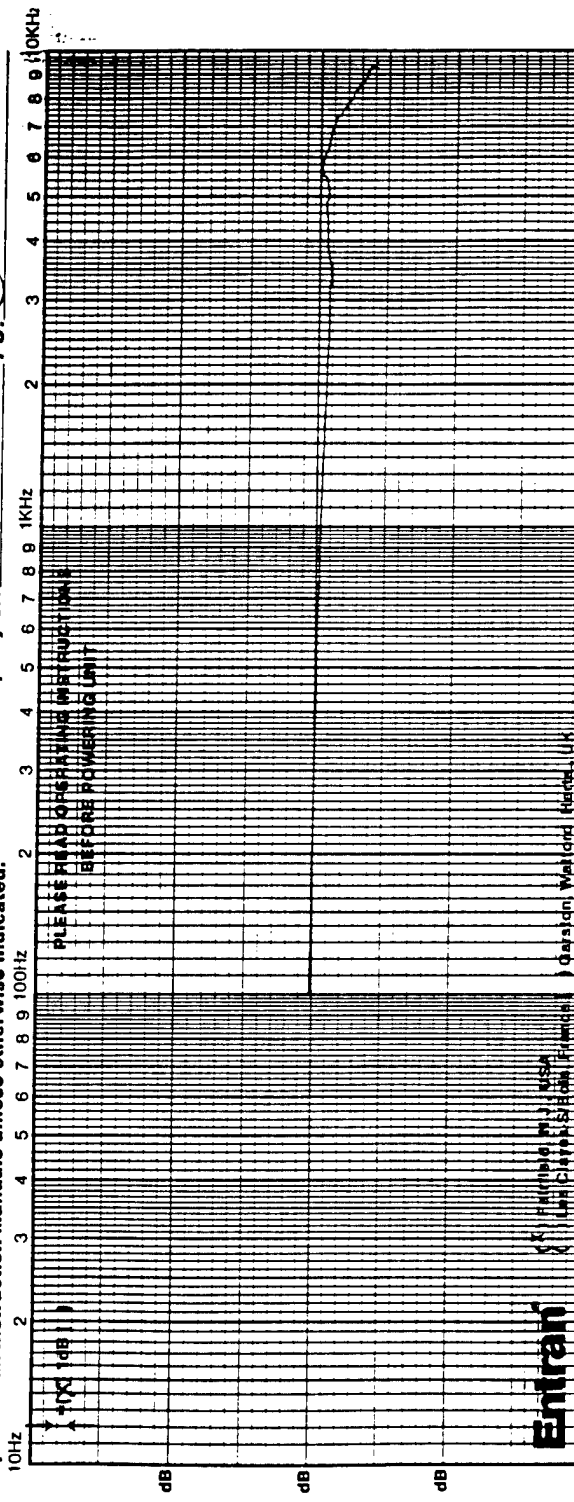


JALSIK

**CERTIFICATE OF CALIBRATION**

This instrument has been calibrated against a working standard which is directly traceable to a National Standard. All data interpreted per Entran Instruction Manuals unless otherwise indicated.

MODEL: EGA-125-10000      S/N: 92J91G12-P06  
 CAL EQUIPMENT S/N'S: ACC-129      Axis: 3126401  
 Entran by: JH-Cal. Date: 07/24/92      FQ#: 20252  
 Property of:  QC  PO:  QC

**CALIBRATION DATA**

Model : EGA-125-10000      S/N: 92J91G12-P06  
 Range :  $\pm 10000$       Lmt:  $\pm 30000$       Axis:  
 Temperature Range, Compensated: 70 to 170°F      Operating: -40 to 250°F  
 Subject to 10,000g Shock In: 1 Sensitive Axis Only ( All Axes )

**ACCELEROMETER WIRING**

To Module:  (M'Red)      To:  (M'Blk)  
 +In:  (M'Red)      +In:  (M'Blk)  
 -In:  (M'Red)      -In:  (M'Blk)  
 +Out:  (M'Blu)      +Out:  (M'Blu)  
 -Out:  (M'Blu)      -Out:  (M'Blu)  
 Connectors:  Male       Female

SHIPPING AND REPACKAGING INFORMATION

In calibrated data equals or exceeds data sheet specifications, value shown is the data sheet value unless purchase order specifies actual calibrated value. System shown is by manufacturer's claim and calibrated value is required for transducer. Note II requires return from distributor. (This means Rejection Frequency.

(For  $\pm 100$  Input, Do not use

unipolar 38V power supply)

1.2 Non-linearity:  $\pm 1\%$ FS      Subject to 10,000g Shock In: 1 Sensitive Axis Only ( All Axes )  
 1.2 Non-linearity:  $\pm 1\%$ FS      S/N: 92J91G12-P06  
 1.2 Non-linearity:  $\pm 1\%$ FS      2 X axis :  $\pm 2.5\%$  100°F  
 1.2 Non-linearity:  $\pm 1\%$ FS      273 :  $\pm 2.5\%$  100°F  
 1.2 Non-linearity:  $\pm 1\%$ FS      across :  
 1.2 Non-linearity:  $\pm 1\%$ FS      Max. In : 18.0 VDC  
 1.2 Non-linearity:  $\pm 1\%$ FS      4 Appr. In: S/N:  
 1.2 Non-linearity:  $\pm 1\%$ FS      with In : Max. In :  
 1.2 Non-linearity:  $\pm 1\%$ FS      with In : See Over :  
 1.2 Non-linearity:  $\pm 1\%$ FS      Output U : 477  
 1.2 Non-linearity:  $\pm 1\%$ FS      Input I : 15.47

**ELECTRONICS**

1.2 Non-linearity:  $\pm 1\%$ FS      S/N: 92J91G12-P06  
 1.2 Non-linearity:  $\pm 1\%$ FS      2 X axis :  $\pm 2.5\%$  100°F  
 1.2 Non-linearity:  $\pm 1\%$ FS      273 :  $\pm 2.5\%$  100°F  
 1.2 Non-linearity:  $\pm 1\%$ FS      across :  
 1.2 Non-linearity:  $\pm 1\%$ FS      Max. In : 18.0 VDC  
 1.2 Non-linearity:  $\pm 1\%$ FS      4 Appr. In: S/N:  
 1.2 Non-linearity:  $\pm 1\%$ FS      with In : Max. In :  
 1.2 Non-linearity:  $\pm 1\%$ FS      with In : See Over :  
 1.2 Non-linearity:  $\pm 1\%$ FS      Output U : 477  
 1.2 Non-linearity:  $\pm 1\%$ FS      Input I : 15.47

# HEDLAND

## IR-OPFLOW FLOW METERS INSTALLATION & MAINTENANCE INSTRUCTIONS

**IMPORTANT: READ INSTRUCTIONS THOROUGHLY BEFORE INSTALLING FLOW METER**

### 1. DESCRIPTION

#### A. GENERAL

The IR-OPFlow is an axial paddle wheel turbine type flow meter based on the belt-on wheel principal. This unique patented design makes the IR-OPFlow a very accurate, repeatable, linear device. Not only is the IR-OPFlow precise, but it is also a rugged, trouble-free flow meter which can be used in a wide variety of industries including: medical, pharmaceutical, chemical processing, pulp & paper, and many others.

#### B. PRINCIPLE OF OPERATION

Fluid flows through the meter (1), first passing through a helical nozzle (2) which causes flow to spiral, rotating in a helical pattern. The spiraling fluid then impacts on the flat blade rotor (3), causing the rotor to spin. The rotor is designed to immediately develop a rotation-induced friction-free fluid bearing, thus eliminating any potential bearing wear.

An infra-red, electro-optical transmitter and receiver (4) is molded into the body of the meter, along with a pair of miniature circuit boards, providing voltage stabilizers and automatic IR output

level control that automatically compensates for varying fluid opacity levels\*, providing a square wave electronic output signal.

This design inherently bleeds off entrained gas, improving the accuracy of the meter. It also eliminates the need for flow straighteners or special lengths of inlet piping to stabilize turbulent flow. This compact meter can be installed in any orientation, immediately adjacent to 90° elbows or other fixtures, upstream or downstream, giving you greater system design flexibility, as well as saving time and money during installation.

\*Clear, transparent and translucent fluids, must transmit infrared light.

### 2. MATERIAL CHARACTERISTICS OF PVDF (Polyvinylidene Fluoride)

#### A. MATERIAL OF CONSTRUCTION

Trade name — Kynar\*\*

All wetted parts of the IR-OPFlow are PVDF, excluding the O-ring. Wetted parts include any part of the meter that will or could come in contact with the fluid.

List of wetted parts:

1. Barbed fittings	5. End caps
2. Flow meter body	6. Strainer
3. Rotor	7. Bearings
4. Helical nozzle	(Viton O-ring seals.)

#### B. CHEMICAL COMPOSITION OF PVDF

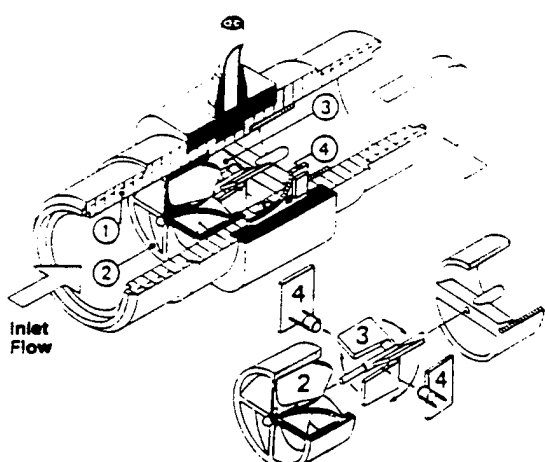
Polyvinylidene fluoride is a fluoropolymer consisting of three basic materials (carbon, hydrogen and fluorine).

#### C. CHEMICAL COMPATIBILITY OF PVDF

For a complete list of compatible fluids consult either Hedland or:

Soltex Polymer Corporation  
3333 Richmond Ave. P.O. Box 27328  
Houston, TX 77227  
(713) 522-1781

\*\*(Registered Trademark of Pennwalt Corporation)



**D. EFFECTS OF VARIOUS FLUIDS ON PVDF**

1. Weak Acids - no effect.
2. Strong Acids - attacked by fuming sulfuric & nitric acids at high temperatures.
3. Weak Alkalies - no effect.
4. Strong Alkalies - no effect.
5. Organic Solvents - Resistant to most. Slight attack by some. Imbrittled by some amines, ketone, and esters. (Reference Compass Corrosion Guide II)

**C. OPERATING PARAMETERS**

**A. TEMPERATURE RANGE** (Fluid and Ambient)  
 Dew Point to +185 degrees F.  
 Dew Point to +85 degrees C.

Since the IR-OP Flow has printed circuit boards molded into the body of the meter it is strongly recommended that 185 degrees Fahrenheit not be exceeded. Exceeding 185°F can cause irreparable damage to the circuit boards.

**B. FLOW RANGES**

The IR-OPFlow is available in six different sizes which cover a flow range from .03 - 33 GPM.

Specific Flow Ranges:

502-101	.03 - .53 GPM (0.1 - 2 LPM)
502-102	.08 - 2.38 GPM (0.3 - 9 LPM)
502-103	.13 - 3.96 GPM (0.5 - 15 LPM)
502-104	.26 - 7.93 GPM (1.0 - 30 LPM)
502-105	.79 - 19.81 GPM (3.0 - 75 LPM)
502-106	1.32 - 33.02 GPM (5.0 - 125 LPM)

Consult factory with specific applications requiring an extended flow ranges. "Warning," over spin may permanently damage the flow meters.

**C. RECOMMENDED VISCOSITY RANGE - 1-5 cSt (without correction)**

The effects of changing viscosity on the IR-OPFlow are the same as any other turbine flow meter. It is important to remember that a turbine flow meter is a viscosity dependent device where as the viscosity increases the linearity of the flow meter will decrease. (Water-line fluids are ideally suited for use with the IR-OPFlow.) The IR-OPFlow is calibrated with water.

**CORRECTION PROCEDURE FOR HIGHER VISCOSITIES**

For viscosities greater than 5 cSt consult the factory. The IR-OP Flow can be used on fluids greater than 5 cSt, however, the K-Factor (linearity) will change. This requires a recalibration of the IR-OP Flow at the known viscosity to determine the new K-Factor.

**D. RECOMMENDED FILTRATION**

Meter	Micron Filtration	Mesh Filter
502-101	35 micrometer	400 mesh
*502-102	50 micrometer	300 mesh
*502-103	100 micrometer	80 mesh
*502-104	100 micrometer	80 mesh
*502-105	100 micrometer	80 mesh
*502-106	100 micrometer	80 mesh

IR-OPFlow sizes 2-6 are fitted with strainers to help protect against dirt, fiber, and other contaminants. Due to space restriction, it is not possible to fit size 1 with a strainer. Removal of the strainer will reduce pressure drop through the flow meter, and may also change the linearity of the meter. Removal could also subject the meter to solid contaminant which could damage the meter.

\*The strainer is a 30 mesh filter/ 550 micrometer.

**E. CLEANING**

**1. STEAM CLEANING**

Steam sterilization is not possible with the IR-OPFlow due to the high temperature of the steam. Steam sterilization will permanently damage the flow meters bearings and printed circuit boards.

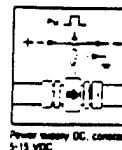
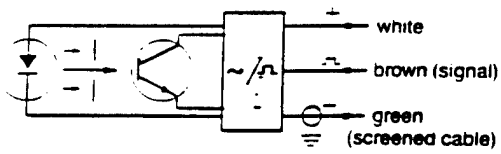
**2. CHEMICAL CLEANING**

Chemical cleaning the IR-OPFlow is permissible provided the chemicals are compatible with PVDF (polyvinylidene fluoride).

**F. BI-DIRECTIONAL FLOW**

The IR-OPFlow is designed to only provide fluid readings in the forward flow direction only. Reverse flow will not unduly restrict fluid flow.

**4. INFRA-RED SENSOR**



**A. SUPPLY VOLTAGE**

5-15 VDC (6-33 mA)

Do not exceed 15 VDC. Doing so can cause over-heating and the eventual failure of the PC boards. Printed circuit boards are non-repairable.

**B. FREQUENCY OUTPUT** Excluding Models 502-124 502-126 & 502-128. Consult factory for further details on these models.

1. Square wave pulse, unscaled
2. Output impedance 75 ohms
3. Directly proportional to flow rate
4. Output - Dc frequency
5. Offset .64 volts
6. Peak voltage = Supply voltage - 1.2V  
(example: 12Vdc - 1.2V = 10.8V)
7. Peak to peak voltage = Supply voltage - 1.2V-.64V  
(example: 12Vdc - 1.2V - .64V = 10.16V)
8. Output signal cycle 66.7%: (example: at 100 Hz there is a 6 millisecond on time, and a 4 millisecond off time.
9. TTL/CMOS circuit compatibility  
The IR-OPFlow has an operational amplifier output which has a high input impedance and a low output impedance.

**C. FREQUENCY RANGES FOR IR-OPFLOW**

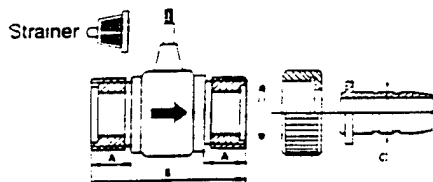
Model	Frequency (Hz)	K Factor	Pulses/Gal.
502-101	60-1200	136.260	
502-102	40-1200	30.280	
502-103	27-800	12.112	
502-104	20-600	4.542	
502-105	25-625	1.703	
502-106	21-521	352	

**D. CABLE REQUIREMENT**

1. 20 - 22 AWG (American Wire Gauge)
2. 3 conductor-shield cable

NOTE: Avoid influences of strong electromagnetic forces as they can damage components on the PC board.

**E. INSTALLING THE IR-OPFLOW IN THE FLUID LINE**



Model Number	Connections <sup>①</sup> Thread Sizes	Dimensions (inches)		
		A	B	C
502-101	Barb Fitting for .27" ID Hose	0.4	1.6	0.3
502-102	Barb Fitting for .35" ID Hose	0.5	1.8	0.4
502-103	Barb Fitting for .47" ID Hose	0.5	1.8	0.5
502-104	Barb Fitting for .63" ID Hose	0.6	2.3	0.6
502-105	1" Male NPT/BSP	.65	3.15	.77
502-106	1" Male NPT/BSP	.65	3.15	.95

<sup>①</sup>For other fittings, consult factory

**A.** Make sure the fluid is compatible with PVDF (polyvinylidene fluoride) and meets viscosity, pressure, and temperature parameters of the IR-OPFlow. The fluid must also meet filtration requirements as listed in 3.D.

**B.** Install the IR-OPFlow in the fluid line with the arrow pointing in the direction of flow. All IR-OPFlows are supplied with barbed hose fittings as standard equipment. If the IR-OPFlow is to be placed in a metallic fluid line, optional 316 Stainless Steel fittings available for sizes 1 - 4. Consult factory for price and availability.

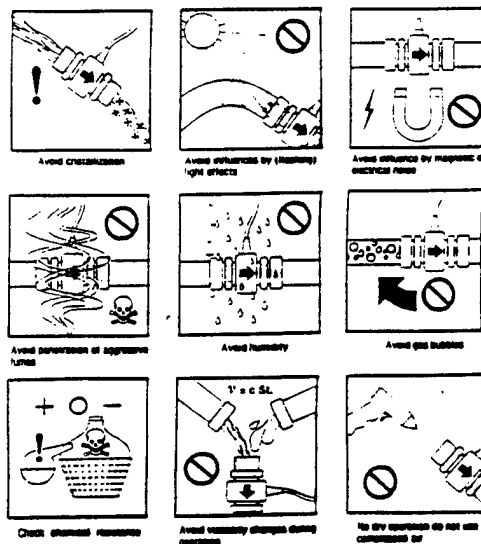
**C.** While installing the IR-OPFlow in the fluid line be careful not to over torque the end caps or other fittings on the flow meter. Due to the soft composition of PVDF the body or threads can be permanently distorted.

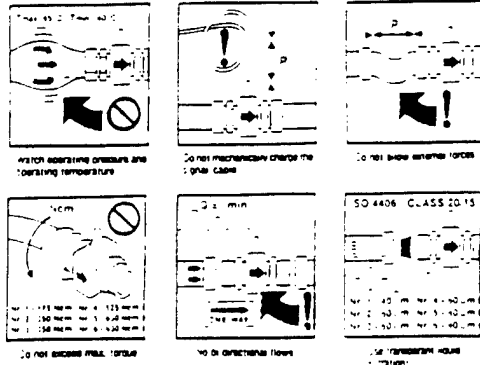
**D.** Attach wires to the readout display with the display and power off. Not only will this help to avoid a potential shock hazard, but it can also help prevent an error in hooking the flow meter to an incorrect 115VAC supply

If additional cable is required to hookup the flow meter to a digital display take caution when soldering to ensure correct connections.

**E.** Connect digital display to power supply and enter scaling factors for both the rate and total. Follow the manufacturers instructions for programming digital display.

**F.** The IR-OPFlow is now ready for use.





## 6. TROUBLESHOOTING

- If the readout does not provide correct information, review the scaling factors and the numbers programmed.
- Next check the wiring hookups to the display and all solder points.
- Finally check the flow meter for contamination.
- Consult Hedland for additional assistance.

## 7. REPAIRING THE IR-OPFLOW

- Replaceable parts for the IR-OPFlow
  - Barbed Fittings
  - Viton O-rings
  - End Caps
  - Strainers

(Consult factory for price and availability.)
- Non-repairable parts for IR-OPFlow
  - Rotor
  - Bearings
  - Printed circuit boards

## 3. LIMITED WARRANTY

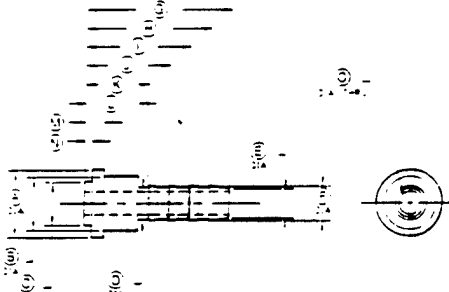
The Hedland Division of Racine Federated, Inc. warrants to the original purchaser, for the period of one year from the date of purchase, that each new flow meter is free from defects in materials and workmanship.

The warranty does not cover meters that have been damaged due to abuse, incorrect installation, or operated beyond Hedland's stated maximum parameters for the IR-OPFlow.

Hedland's sole obligations under the warranty is limited to the repair or replacement of parts, determined to be defective after inspection by Hedland. Repair or replacement of parts at Hedland's discretion.

Hedland is not liable for any consequential damages or any contingent liabilities arising out of the failure of any flow meter part, component part or accessory.

The above warranty supersedes and is in lieu of all other warranties, either expressed or implied and all other obligations or liabilities. No agent, representative or distributor has any authority to alter the terms of this warranty, in any way.



IR-OPFLOW BARB FITTING DIMENSIONS (in inches)																
Model (Size)	A Dia.	B Dia.	C Dia.	D Dia.	E Dia.	F Dia.	G Dia.	H Dia.	I Dia.	J Dia.	K Dia.	L Dia.	M Dia.	N Dia.	O Dia.	
-01	.380	.302	.230	.240	.226	.267	.1.60	.005	.807	.609	.417	.333	.150	.066	.150	
-02	.668	.528	.430	.310	.288	.342	.1.427	.1.228	.1.03	.832	.634	.503	.195	.079	.228	
-03	.556	.519	.460	.422	.392	.462	.1.450	.1.112	.920	.723	.536	.437	.156	.064	.306	
-04	.900	.680	.610	.515	.532	.587	.1.594	.1.322	.1.069	.753	.493		.185	.071	.460	
-05	1.165	1.014	.840	—	.711	.772	2.096	.1.750	.1.453	1.156	.899	.700	.234	.104	.616	
-06	1.181	1.026	.915	—	.897	.964	2.132	.1.730 + .120	.1.470	1.210	1.000	.675	.238	.121	.770	

**HEDLAND**  
DIVISION OF RACINE FEDERATED INC.

MAILING ADDRESS

P.O. BOX 1405  
RACINE, WI 53401

TELEPHONE:  
(414) 639-6770  
or 1-800-HEDLAND

SHIPPING ADDRESS:

2200 SOUTH STREET  
RACINE, WI 53404

FACSIMILE:  
(414) 639-2267  
or 1-800-CHK-FLOW

FORM #234A 8/92

## PIEZORESISTIVE SENSOR PRE-AMPLIFIER AND SIGNAL CONDITIONER PR100

### OPERATIONS GUIDE

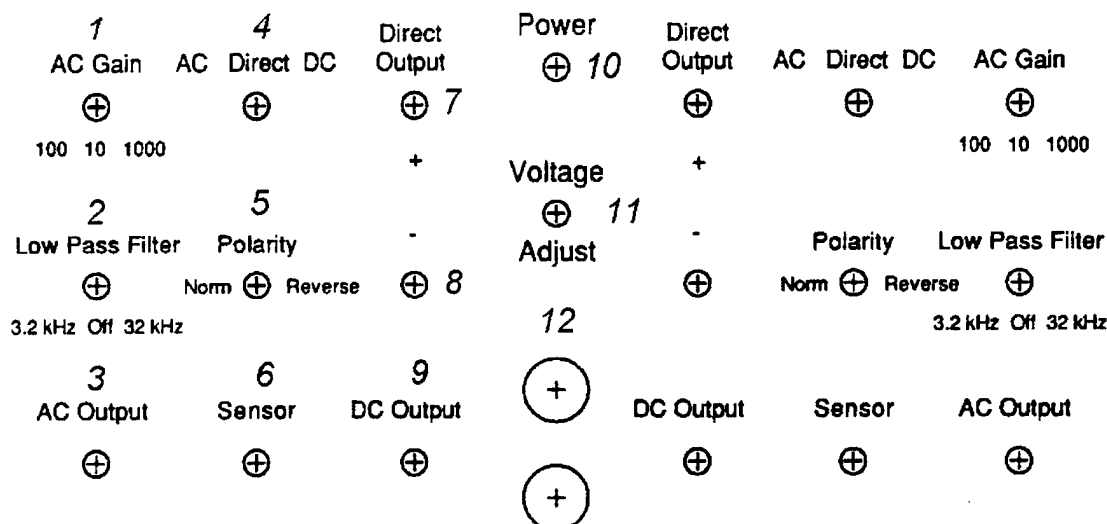


Figure 1

#### THE FRONT PANEL:

The front panel shown in Figure 1 can be divided into three sections. The left and right wings contain the outputs, inputs and controls for each channel while the center of the panel contains the power LED and the bias supply control and monitor sockets.

The circuit and function for the left and right pre-amp channels are identical, as is the front panel interface. The sensor input socket is a Switchcraft "TINI QG" 4-pin. The pin-out used in this device is shown below. So that the device can be immediately usable upon receipt, two Switchcraft plugs (the mate to the TINI QG) are included. It is very important that these plugs be wired to the sensor in accordance with the pin-out below! The figure below (Figure 2) is drawn as though the user is looking at the front panel.

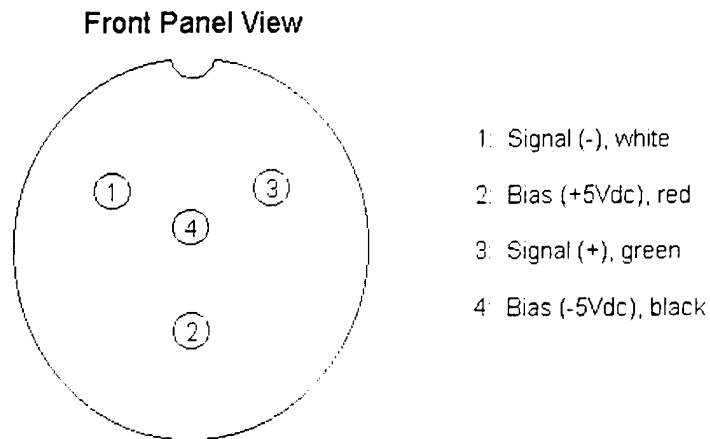


Figure 2

### BIAS SUPPLY:

The center of the front panel contains the bias supply interface and the power on indicator LED (number 10 on the drawing.) Using the 20 turn potentiometer (11) the bias supply can be tweaked between 9.6 V<sub>DC</sub> and 10.5 V<sub>DC</sub>. This bias voltage can be monitored with a multimeter via the banana plug receptacles (12). The bias supply circuitry provides a very stable supply and while it is good practice to check the supply voltage before making a series of measurements, the supply does not generally need to be adjusted.

### AC SIGNAL MODE:

The PR100 can amplify and condition two AC signals – one signal per channel. Use switch 4 to select AC signal input for the left channel. There are three amplifier gain settings, 10, 100 and 1000 -- use switch 1 to set the AC gain. Included in the AC amplification circuit is a choice of two low pass filter cut-off frequencies, 3.2kHz and 32 kHz. Use switch 2 to set the cut-off frequency, or disable the filter altogether (the OFF position.) To invert the amplified and optionally filtered AC signal, use the Polarity switch, switch 5.

Obviously, if switch 4 is set for AC signal inputs, the active output terminal is the isolated BNC receptacle 3, labeled AC output.

The AC amplifier circuit uses an AD620 instrumentation amplifier chip. The specs for this chip from Analog Devices are included at the end of this brief. The gain-bandwidth product for the AD620 chip is 800 kHz at a gain of 10, 120 kHz at a gain of 100 and 12 kHz at a gain of 1000. This means that at the highest gain setting, the response will roll off at 12 kHz, even if the filter switch is set to 32 kHz.

### **DC SIGNAL MODE:**

Since piezoresistive sensors are often used for static measurements, like strain gauges, a DC output mode is included. The gain amplification switch is inactive in DC mode as is the Low Pass Filter switch. The polarity switch is active, however. Use the isolated DC Output BNC receptacle (receptacle 9) to monitor the DC mode.

The DC mode circuitry employs an AMP03 differential amplifier chip which is a unity gain high input impedance output chip. This chip is used so that a voltmeter or other measurement device will not directly load the sensor. The chip also serves to isolate the ground reference of the signal from house ground. Documentation on this chip is also included.

### **DIRECT MODE:**

The direct signal mode allows the user to monitor the sensor signal directly and through no signal conditioning or amplification. Use the two non-isolated BNC terminals (receptacles 7 and 8) to monitor this signal. Remember that the shield of these BNC terminals is not a reference (as the shield is the reference in AC and DC mode) – the center pin of the BNC 7 is referenced to the center pin of BNC 8. The shields of BNC plugs 7 and 8 are connected to the chassis (and in turn connected to house ground.)

The direct mode option is included for users who may want to use their own differential amplifier. The user should be aware that the device attached to the direct output terminals (BNC 7 and 8) could provide a significant impedance load to the sensor which could skew measurement results.

### **TROUBLE SHOOTING:**

The circuit schematic is included in this brief – however, the actual circuit board layout is not. The circuit board layout is easy to understand by comparing the schematic and the board layout and knowing the following things:

- The board layout sort of models the front panel – that is, the bias supply circuitry is in the center of the board and the left channel is to the left, etc.
- The AC circuitry for each channel is toward the bottom of the board (so the left AC channel is to the bottom left corner nearest the blue edge connector as you look down from above the box with the front panel facing you) and the DC circuitry is directly above the AC circuits. Since the board is connected to the front panel via a removable edge connector – board removal is simply a matter of removing three screws and unplugging the board from the edge connector.

- The gain setting resistors and the low-pass filter capacitors are part of the front panel. They are soldered to the switch that controls the gain or filter functions.

For the protection of your sensors and measurement equipment, please use a 1/8 Amp Slo-Blo fuse for the PR100.

Since schematics and manuals tend to get lost, there is a copy of the schematic taped to the inside of the chassis.

For help with troubleshooting and initial testing, a pair of test leads are included that have gold sockets on one end. These leads will fit on the pins in the Switchcraft socket and can be used to inject a signal to the device with a signal analyzer and measure the frequency response of the device with no sensor. These frequency response plots are included so that you can periodically compare the amplifier performance to the "freshly built" results.

These curves shown below are made on an HP 35670A 4 channel analyzer. The instrument is in swept sine mode and the source signal is 25 mVrms. The inputs are grounded and AC coupled. Figure 3 shows the frequency response magnitude and phase – the gain switch is set to 10 and the filter switch is OFF for both channels.

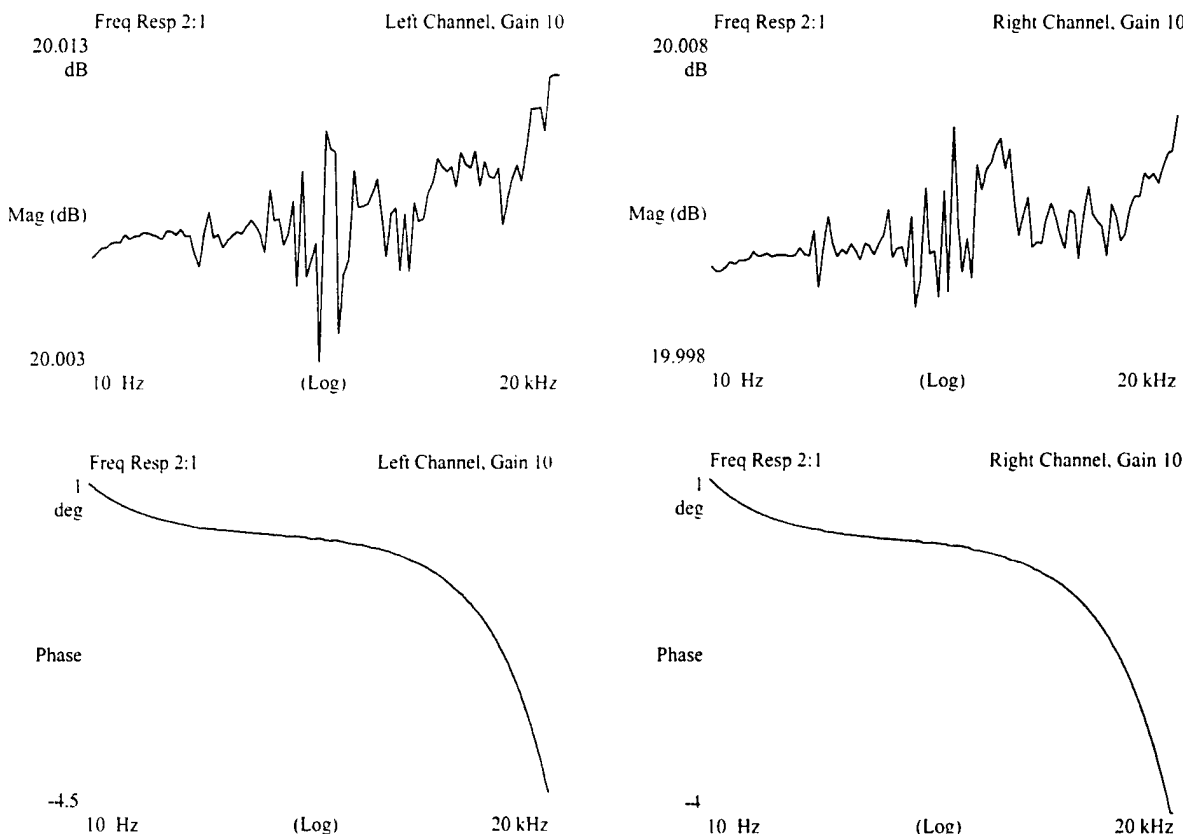


Figure 3

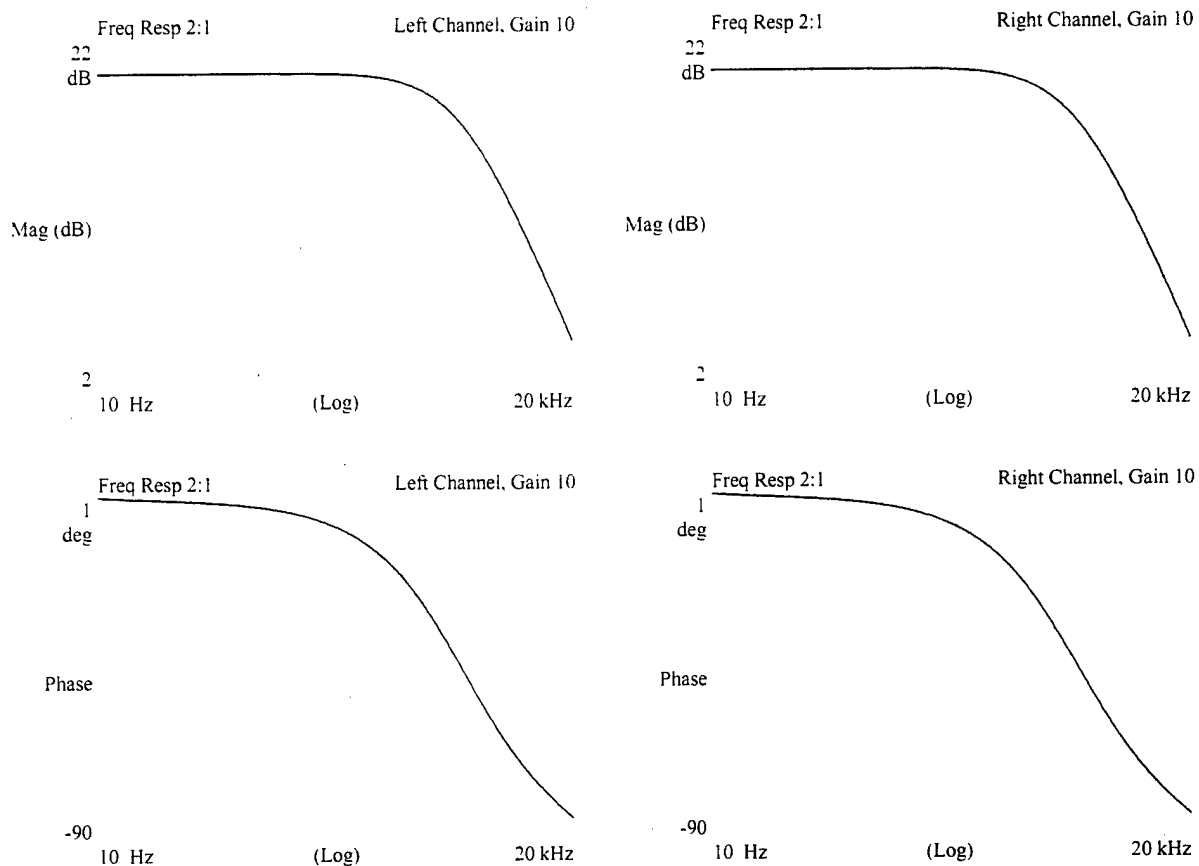
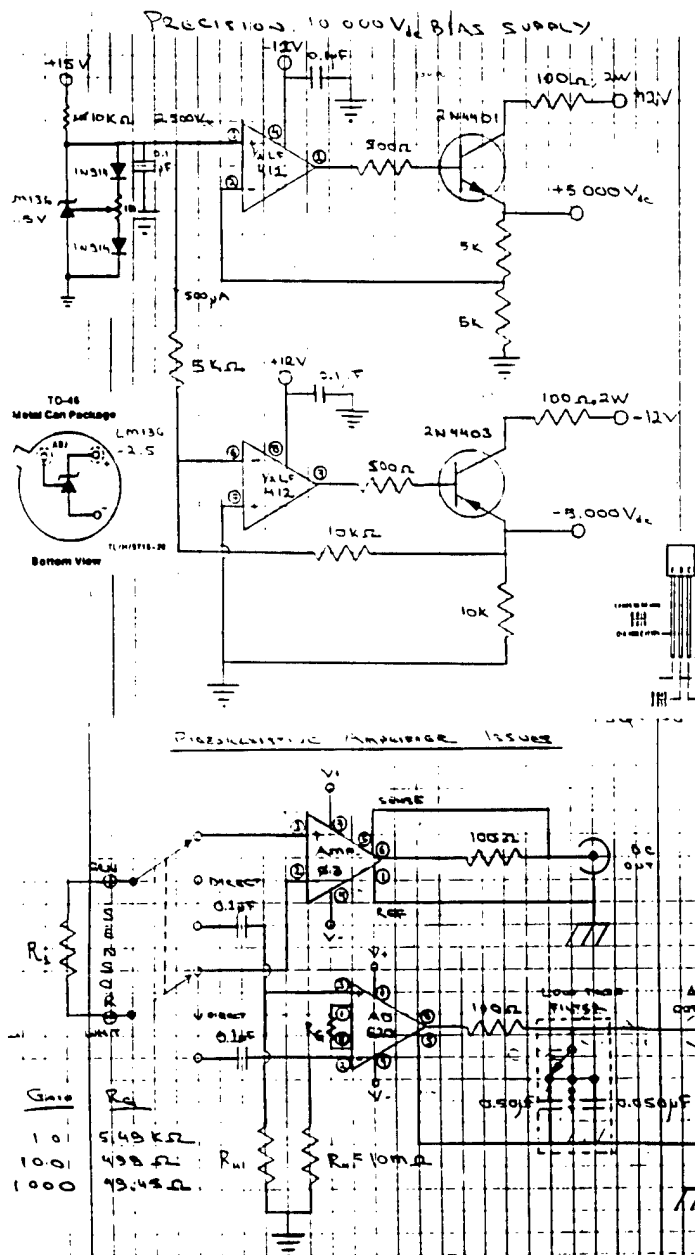


Figure 4

Figure 4 shows the frequency response functions for each channel in the gain 10 setting but with the 3.2 kHz filter switched on. Upon receipt of the device, it would be a good idea to try to reproduce these graphs and check the other gain and filter settings. If there are significant discrepancies, something is probably wrong – please don't hesitate to get in touch with me.



*EDIT CARD VHS*

### Edge Card Connections (Bridge Sensor Dual Amp)

(Bridge Sensor Dual Amp)					
Pin	Wire	Function	Pin	Wire	Function
1	Yellow (w/blue)	(+) IN for AC Amp (Left)	A	Yellow	Gain Resistor (Left)
2	Blue (w/ yellow)	(+) IN for AC Amp (Left)	B		
3	Yellow (w/purple)	(-) IN for DC Amp (Left)	C		
4			D	Blue	AC Amp OUTPUT (Left)
5	Purple (w/ yellow)	(+) IN for IX' Amp (Left)	E		
6			F	Yellow	Gain Resistor (Left)
7	Purple	DC Amp OUTPUT (Left)	H		
8	Grey	Power Supply Common	J		
9	Red	(+) 5 000 Volts	K		
10			L	White	(-) Adjust Pot (2 50 V)
11			M		
12	Black	(-) 5 000 Volts	N		
13			P		
14	Green	(+) 2 50 Volt Pot - Wiper	R		
15	Grey	Power Supply Common	S		
16	Yellow (w/ blue)	(-) IN for AC Amp (Right)	T		
17	Blue (w/ yellow)	(+) IN for AC Amp (Right)	U	Yellow	Gain Resistor (Right)
18	Purple (w/ yellow)	(+) IN for DC Amp (Right)	V	Yellow (w/purple)	(-) IN for DC Amp (Left)
19			W		
20	Grey	Power Supply Common	X	Yellow	Gain Resistor (Right)
21	Blue	DC Amp OUTPUT (Right)	Y	Purple	DC Amp OUTPUT (Right)
22	Grey	Power Supply Common	Z	Black	(-) 12 Volt Power Supply
				Red	(+) 12 Volt Power Supply